2013

INFLUENCE OF SURFACE MODIFICATION ON PROPERTIES AND APPLICATIONS OF COMPLEX ENGINEERED NANOPARTICLES

Binghui Wang
University of Kentucky, galieo198098@hotmail.com

Recommended Citation

Wang, Binghui, "INFLUENCE OF SURFACE MODIFICATION ON PROPERTIES AND APPLICATIONS OF COMPLEX ENGINEERED NANOPARTICLES" (2013). *Theses and Dissertations--Chemical and Materials Engineering*. 24.
https://uknowledge.uky.edu/cme_etds/24

STUDENT AGREEMENT:

I represent that my thesis or dissertation and abstract are my original work. Proper attribution has been given to all outside sources. I understand that I am solely responsible for obtaining any needed copyright permissions. I have obtained and attached hereto needed written permission statements(s) from the owner(s) of each third-party copyrighted matter to be included in my work, allowing electronic distribution (if such use is not permitted by the fair use doctrine).

I hereby grant to The University of Kentucky and its agents the non-exclusive license to archive and make accessible my work in whole or in part in all forms of media, now or hereafter known. I agree that the document mentioned above may be made available immediately for worldwide access unless a preapproved embargo applies.

I retain all other ownership rights to the copyright of my work. I also retain the right to use in future works (such as articles or books) all or part of my work. I understand that I am free to register the copyright to my work.

REVIEW, APPROVAL AND ACCEPTANCE

The document mentioned above has been reviewed and accepted by the student's advisor, on behalf of the advisory committee, and by the Director of Graduate Studies (DGS), on behalf of the program; we verify that this is the final, approved version of the student's dissertation including all changes required by the advisory committee. The undersigned agree to abide by the statements above.

Binghui Wang, Student

Dr. Eric A. Grulke, Major Professor

Dr. Fuqian Yang, Director of Graduate Studies

INFLUENCE OF SURFACE MODIFICATION ON PROPERTIES AND APPLICATIONS OF COMPLEX ENGINEERED NANOPARTICLES

DISSERTATION

A dissertation submitted in partial fulfillment of the requirement
for the degree of Doctoral of Philosophy in the College of Engineering
at the University of Kentucky

By
Binghui Wang

Lexington Kentucky

Director: Dr. Eric A. Grulke, Professor of Chemical and Materials Engineering

Lexington, Kentucky

2013

ABSTRACT OF DISSERTATION

INFLUENCE OF SURFACE MODIFICATION ON PROPERTIES AND APPLICATIONS OF COMPLEX ENGINEERED NANOPARTICLES

Complex engineered nanoparticles (CENPs) are being used on various applications. Their properties are different from those of neat nanoparticles. The dissertation explores these differences from four aspects: 1) Modify carbon nanomaterials' inert surfaces and investigate the effect on thermal and rheological behavior of their dispersions; 2) Generate self-assembly bi-layer structure of oxide nanoparticles via surface modification; 3) Study interaction between lysozyme and different surface-charged ceria nanoparticles; 4) Investigate the biodistribution and transformations of CENPs in biological media.

An environment-friendly surface modification was developed to modify surfaces of carbon nanomaterials for increasing their affinity to non-polar fluid. It can offset formation of agglomerates in dispersions. Less agglomerates change thermal conductivity and rheological behavior. One combined model, considering shape factor, was built to fit non-linear enhancement on thermal conductivity with volume fraction of nanoparticles.

Constructing bi-layer structure of oxide nanoparticles with different refractive index was crucial for optical thin films. Silanization was used to transform relatively hydrophilic surface of oxide nanoparticles to hydrophobic surface via attaching alkane chains. The self-assembly separation of these nanoparticles can form bi-layer structure in single deposition process since neat nanoparticles keep in hydrophilic monomer while surface-modified nanoparticles settled down.

The adsorption behaviors of lysozyme, one protein with net positive charge, on different surface-charged ceria nanoparticles were investigated. The adsorption isotherm curves were fitted with the Toth and Sips equations satisfactorily. The heterogeneity parameters suggest the surface charge predominate adsorption on negatively charged ceria while lateral effect predominate adsorption on positively charged ceria. The local site energy distributions were also estimated.

The ^{26}Al-labeled nanoalumina coated by ^{14}C-labeled citrate was synthesized and its dispersion was infused intravenously into rat. The Accelerator Mass Spectrometer (AMS) was used to measure isotopes in dosing material and tissues. The ratio of coating and core in liver was slightly less than dosing material while the ratios in brain and bone are much higher than dosing material. It may suggest that some citrate coating dissociated from nanoalumina's surface, entered metabolic cycles, and then redistributed to other organs.

KEYWORDS:
Complex engineered nanoparticles, Silanization, Self-assembly separation, Surface heterogeneity, Biodistribution

Binghui Wang
Student Signature

12/19/13
Date

INFLUENCE OF SURFACE MODIFICATION ON PROPERTIES AND APPLICATIONS OF COMPLEX ENGINEERED NANOPARTICLES

By

Binghui Wang

Dr. Eric A. Grulke
Director of Dissertation

Dr. Fuqian Yang
Director of Graduate Studies

12/19/2013
Date

Acknowledgement

First of all, I would like to express my gratitude to my advisor, Professor Eric A. Grulke for his guidance and support in my research. He opened the gate of nanoscience and nanotechnology to me. He teaches me how to think independently and balance theoretical knowledge, experimental design and practical applications. He gives me very helpful advices and encouragement when I am confused even depressed.

I would like to thank all the members in my advisory board (Dr. Stephen Rankin, Dr. John Balk, Dr. Mark Watson and Dr. Jason DeRouchey) for attending my final examination and give me helpful advices. I appreciate Ms. Monica Mehanna for her encouragement and help. I appreciate Dr. Peng Wu, Dr. Vinod Kanniah, and Dr. Ai Haibara for their theoretical and experimental support in these researches.

I would like to thank Valvoline, Ashland Inc. (along with U.S. Army TARDEC division); Optical Dynamics, division of Vision Dynamics Corporation; US Environmental Protection Agency (EPA) and National Science Foundation (NSF) for sponsoring these projects.

Table of Contents

List of Tables

Chapter 1

Chapter 2

Chapter 3

Chapter 4

Chapter 5

List of Figures

Chapter 1

Chapter 2

Chapter 3

Chapter 4

Chapter 5

Chapter 1: Introduction

Nanoparticles with high surface area and peculiar properties have been potential candidates on various medical, pharmaceutical and industrial applications for some years. With rapid developments of these applications, more specific and strict requirements for properties and performances of nanoparticles were created. Neat nanoparticles are more or less difficult to fit these requirements due to their single component and relatively fixed properties. The complex engineered nanoparticles (CENPs), which contain some nanoparticles as core material and some coatings formed in synthesis or surface modification, have been proposed to close the gap between nanoparticles and needs from applications.

On design, synthesis and use of CENPs, researchers have to think three questions:

1) How to create effective method to modify nanoparticles' surfaces for satisfying specific needs from different applications?
2) How do these surface modifications affect the properties and applications of nanoparticles and their dispersions?
3) What is the fate of these surface-modified CENPs in biological and environmental media, especially for CENPs used on medical and pharmaceutical applications?

The prior studies on these questions are summarized in following parts of this chapter. Chapter 1.1 focused on the three common methods (electrostatic coating, steric exclusion and dispersant) to create CENPs and increase the stability of their dispersions. Chapter 1.2 and 1.3 summarized the thermal conductivity and rheological behavior of dispersion with neat and surface-modified nanoparticles. Both of them are important to create better potential heat transfer fluid. The first part in chapter 1.4 focused on the recent studies on interactions between CENPs and biomacromolecules like protein and DNA. The second part in chapter 1.4 summarized the studies on toxicity, biopersistence and biodistribution of CENPs.

1.1 Surface modification methods on inorganic nanoparticles

1.1.1 Introduction

Compared with bulk material and micro-particles, nanoparticles possess large surface area per unit mass, in another word, a large fraction of total atoms are surface atoms. The surface atoms possess fewer neighbor or coordination atoms than inner atoms so they have dangling or unsatisfied bonds exposed to the surface. It is a thermodynamically unstable or metastable state, and brings extra energy to surface atoms. The extra energy per unit surface area, named surface energy, is defined as the partial derivative of Gibbs free energy on surface area (Equation 1.1)

$$\gamma = \left(\frac{\partial G}{\partial A}\right)_{n_i,T,P} \qquad (1.1)$$

Where γ is the surface energy (J/m), G is the Gibbs free energy (J), A is the surface area (m), T is the temperature, and P is the pressure.

The surface energy and large surface areas of nanoparticles result in very large surface energy per unit mass, and a strong tendency to decrease surface energy via various mechanisms. Due to their rigid structure, solid nanoparticles usually don’t decrease the surface energy through surface relaxation as might occur with liquid. They usually decrease the surface energy via formation of new bonds with other species or surface adsorption procedure. Many applications, like high-reactive catalysts and high efficiency adsorbent, take advantage of these bonding or adsorption procedures. However, the bonding or adsorption procedures result in nanoparticles connecting together to form agglomerates in base fluids. It can limit the application of nanofluids as the practical structure may be larger than nanoscale.

Nanofluids, the colloidal dispersions of nanoparticles in continuous fluid, have been used on various applications such as high heat transfer coolant (S.-C. Tzeng 2005, Ying Yang 2005) and detergent (Nikolov 2003, K. Sefiane 2008). For improving long-time stability of heat transfer fluid, a good association between dispersed nanoparticles and base fluid was necessary since it can offset the tendency of nanoparticles to form agglomerates. However, some inorganic nanoparticles such as oxide, carbide and carbon nanomaterials were not well wetted by base fluid, even settle from their dispersions. Ultrasonication has been used widely to form uniform dispersions. It gave a “brute force” approach that was less dependent on the physical and chemical properties of nanoparticles and base fluids, while the effect was not long-term after removal of ultrasonication energy (Suslick and Price 1999, Yang, Grulke et al. 2005). The pH control was another useful method to keep stability but it was extrinsic control method and affected by the polarity of the system. Therefore, intrinsic surface modifications through chemical reaction or strong adsorption, which can bring on the electrostatic or steric stabilization, were developed to create stable nanofluids (Hilding, Grulke et al. 2003). Dispersants were another useful method. The long polymer chains of dispersants can adsorb strongly on the surface of nanoparticle to maintain stability of dispersion. The principles and common methods of surface modification were summarized in following paragraphs.

1.1.2 Electrostatic coating

Through chemical reaction or strong adsorption, surface modification can create some functional groups on the surface of inorganic nanoparticles. The partial charges through absorption of ions or dissociation of surface functional groups can form surface charges on the nanoparticles. The counter ions will be attracted and loosely associated with the surface to form the second layer. When two nanoparticles with double electrical layer structure approach each other, the layers overlap and electrostatic repulsion arises, which can offset the surface energy and van der Waals force, so the system can have long-term stability to nanofluids(Cao 2004).

For neat oxide nanoparticles, the typical functional group is hydroxyl group that always exist on the their surfaces in different levels (George 1995, Cao 2004). They arise mainly from synthesis methods such sol-gel procedure for silica and hydrothermal method for titania and ceria nanoparticles. Besides the synthesis conditions, the processing history and environment where the oxide nanoparticles were kept also lead to change on surface density of hydroxyl groups. For insoluble inorganic nanoparticles, the hydroxyl groups dissociate with difficulty, neither like acid forming protons, nor like base forming hydroxide ions. The surface hydroxyl groups usually react with carboxylic groups to form charges. The binding of monodentate carboxylic acid was relatively weak so that the formed coating was readily removed in use and environment (Eva M. Wong 2001, Taratula 2006). However, the use of multi-dentate binding domains was generally recognized to dramatically enhance the stability of nanofluids (Galoppini 2004).

Citric acid (Figure 1.1), a tridentate carboxylic acid has been used to stability some nanoparticles such as iron oxides (Lindegren M 2009), zinc oxide (Z. R. Tian 2003, Lee M. Bishop 2011) and titania (Mudunkotuwa IA 2010) nanoparticles. Due to low bio-toxicity, it was also used to modify the surface of nanocarrier applied in pharmaceutical research like ceria nanoparticles (Masui 2002, Dan M 2012, Yokel 2013).

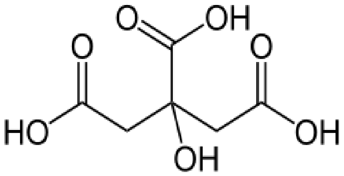

Figure 1.1 Chemical structure of citric acid

Compared with oxide nanoparticles, there are fewer hydroxyl groups on the surface of carbide like silicon carbide, a usual abrasion-resistant material. Hydrofluoric acid (HF) was commonly used to clear the surface of silicon carbide and form more hydroxyl groups after hydrolysis (Alekseev, Zaitsev et al. 2007, Schoell, Hoeb et al. 2008). The surface of neat carbon material is more chemically inert than carbide. The traditional surface modification for carbon material was to use strong oxidants such as potassium permanganate ($KMnO_4$) or concentrated nitric acid (HNO_3) in the presence of concentrated sulfuric acid (Liu, Rinzler et al. 1998, Zhang, Xie et al. 2002). After oxidation, hydroxyl, carboxylic or nitro group ($-NO_2$) was created on the sidewalls of CNTs. The dissociation of carboxylic groups can supply negative charges (Shaffer, Fan et al. 1998, G.I. Titelman, V. Gelman et al. 2005). Amine groups ($-NH_2$) reduced from nitro groups can associate with protons to make positive charge on surface (Li Wang 2010). Both positive and negative charged surface can build stable aqueous carbon nanotube suspension. Another more “green” method was to use citric acid to create hydroxyl group and carboxyl groups on the surface of carbon nanotubes and carbon black (Chee Kok Poh 2008, Poh, Lim et al. 2008). Only citric acid and heat treatment were used in this procedure. Complicated operation and post-treatment in the traditional method were avoided.

These prior electrostatic surface modification methods can help disperse inorganic nanoparticles in highly polar fluids like water and buffer. It is useful to prepare stable nanofluid used for biological and pharmaceutical applications. These studies initiated our idea for using citric acid as coating material for ceria and creating more functional groups on graphite nanodisks. However, it couldn't help us a lot on dispersing inorganic nanoparticles in nonpolar fluid, like base synthetic polyolefin used in creating high heat-transfer fluid. The steric stabilization is more useful in applications that require nonpolar continuous phase.

1.2.3 Steric exclusion coating

The steric exclusion was obtained by linking some non-charged flexible polymer chains to the surface of nanoparticles by covalent bonds. The continuous phase should be the good solvent of the polymer chains and thus the polymer chains extend. When two nanoparticles are partly modified by polymer chain approaches, interpenetration of extended polymer chains result in a reduction of the freedom of polymer's motion, which leads to a reduction of entropy, i.e. $\Delta S<0$. Assuming the enthalpy in this procedure is near zero, the change of Gibbs free energy should be positive from equation 1.2, the definition of Gibbs free energy.

$$\Delta G = \Delta H - T\Delta S \qquad (1.2)$$

When the coverage of polymer chains on nanoparticles' surface increases, the possibility of interpenetration decrease and there are higher repulsive forces between these two approaching nanoparticles.

There were mainly two methods to form steric exclusion coatings: initiating polymerization on the surface via catalyst encapsulated in nanoparticles or nanotube, and grafting polymer chain via reaction between surface functional groups. The initiation of polymerization has been used on surface modification of carbon nanotube (Daniel Bonduel 2005) and titania (Raghuraman 2008). However, they usually have strict requirements for system purity and reaction conditions. Grafting polymer chains to surface via functional groups was simpler choice. In previous paragraph, we have mentioned that there are hydroxyl groups on oxide nanoparticle. The reaction between hydroxyl groups and silane coupling agents to create steric exclusion coatings was a simple and useful surface modification method. These silane coupling agents typically have one, two or three reactive groups, such as methoxyl, ethoxyl or chloro groups, and a varied set of short chain oligomers containing hydrophobic like hydrocarbons (Huesing, Schubert et al. 1996, Garcia-Gonzalez, Fraile et al. 2009) or hydrophilic groups like amine groups (Beck, Hartl et al. 1999, Shimada, Aoki et al. 2003), even super hydrophobic groups like fluorocarbon chains. The reactive groups can form silanol after partly hydrolysis then react with hydroxyl groups on nanoparticles' surface. It has been used on improving the stability of oxide nanoparticle dispersion such as silica, titania (Fumihide Shiraishi1 2013) and zinc oxide nanoparticles (Allen CG 2008).

Silanization method was also used on improving stability of carbon material dispersion. Some researchers managed to use this effect to prevent carbon nanotubes from forming long bundles and agglomerations. Zeng et al use the modified carbon nanobeads with hydroxyl (-OH) and carbonxyl (-COOH) groups to react with N-β-aminoethyl-γ-aminopropyltrimethoxysilane to form carbon nanobeads with amino-silane chains (An and Zeng 2003). Ma et al (Ma, Kim et al. 2006) applied similar method on carbon nanotube. The MWCNTs are oxidized through UV/O3 treatment then reduced to form hydroxyl group via lithium aluminum hydride (LiAlH4). After silanization, better dispersion stability was obtained on the dispersion with silanized MWCNTs. In previous studies of groups, we found silanization reaction can attach hydrocarbon segment on graphite's surface while the amino-silane can react with some carboxylic groups on graphite's surface to attach poly(dimethylsiloxane) segments on surface. In the PAO/PDMS mixture, a potential lubricant with lower pour point, these two kinds of surface-modified graphite nanodisks can migrated exclusively to its preferred phase (V. Kanniah 2012).

The drawback of silanization was that only a part of hydroxyl groups on nanoparticles' surface can participate in coupling reactions with silanol's hydroxyl groups. The remained hydroxyl groups on nanoparticles can make the surface complex blend of polar and nonpolar groups, with a wide range of surface properties. Meanwhile, the hydroxyl groups in silanols have possibility to self-polymerize each other. An improvement on silanization and an evaluation of surface functional groups were needed, which is important to operate more controllable silanization reaction.

1.2.4 Dispersants

Dispersants normally consist of one or more kinds of surfactants such as acids and salts with long polymer chain. One end of the dispersant strongly adsorbed on nanoparticles' surface. The acid or salt give electrostatic effect while long polymer chains give steric exclusion. So dispersant can generate stable dispersions, similar to effect of chemical surface modification while complex chemical reactions are avoided. However, the lack of chemical bonds makes dispersant system usually function as a dynamic equilibrium state. Change of temperature and environment can lead to desorption or degradation of dispersant, even loss of stability.

For oxide nanoparticles, cetyltriammonium bromide (CTAB, Figure 1.2) was one common dispersant. The quaternary ammonium end can adsorb on the nanoparticles' surface and supply the positive charges while the hydrocarbon chains supply steric exclusion effect.

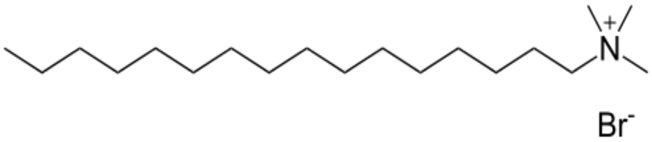

Figure 1.2 Chemical structure of CTAB

CTAB has been successfully applied to stabilize the nanofluids containing titania (Deiss, Anizan et al. 1996), and ceria nanoparticles(Rajendran 2013). Polyacrylic acid (PAA) and polyethylene glycol (PEG) are another two common dispersants to metal oxide nanoparticle. Some carboxylic groups in PAA have strong adsorption with hydroxyl groups on the surface and other carboxylic groups can dissociate and supply electrostatic effect to improve the stability of ceria nanofluid (Wang, Perez et al. 2013). The PEG has been applied on formation of stable iron oxide nanofluid while the stability mechanism was not fully understood yet (Gillich, Acikgöz et al. 2013).

The sodium dodecylsulfate (SDS) and TRITON X-100 with a hydrophilic polyethylene oxide chain, are common dispersants to disperse carbon material in polar fluid, but they fail to build stable dispersions of graphite nanoplatelets. Higher molecular weight poly (sodium 4-styrenesulfonate) (PSS, M_W=70,000) is successful to disperse graphite nanoplatelets in water, shown in Figure 1.3 (Sasha Stankovich 2006).

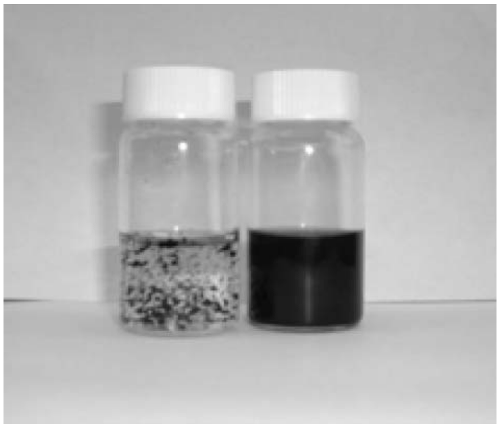

Figure 1.3 Aqueous suspensions of graphite without PSS (left) and with PSS (right)

For nonpolar base fluids like lubricant oil, the commonly used dispersant for dispersing carbon materials is polyisobutylene succinimide (PIBSI, Figure 1.4) (Liu, Lin et al. 2005, Won, Meeker et al. 2005).

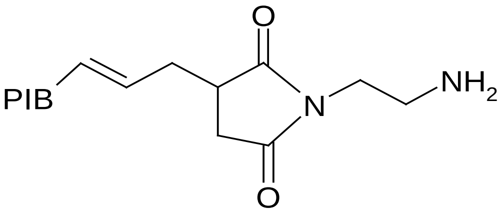

Figure 1.4 Typical chemical structure of PIBSI

The amine or polyamine segment has a high affinity to graphite’s surfaces and the long polyisobutylene (PIB) segment has good solubility in oil and offers steric hindrance to prevent agglomeration of the nanoparticles (Pugh 1984, Chevalier 2001). The previous studies of our groups focused on the influence of higher temperature on the adsorbed amount and conformation of PIBSI molecules. The dispersant doesn’t work very well at high temperature although the adsorbed amount is not sensitive to the temperature. The shrinkage of PIB segment is one reason for dispersant failure (Yang, Grulke et al. 2006).

1.2 Thermal conductivity of inorganic nanofluids

1.2.1 Introduction

One goal of our project was to explore the influence of surface modification on thermal conductivity and of carbon nanomaterial/polyolefin dispersions. Improving the heat transfer properties of heat transfer fluids via adding solid material with high thermal conductivity has been developed and studied for many years. The densities and thermal conductivities of common inorganic solid and conventional heat transfer liquids are summarized in Table 1.1. Obviously, the thermal conductivities of solids are much higher than those of conventional heat transfer fluids.

Table 1.1 Densities and thermal conductivities of solid nanoparticles and conventional liquid at 298K

Type	Materials	Density (g/cm^3)	Thermal Conductivity (W/mK)
carbon nanomaterial	Carbon nanotube	1.3-1.4	900(Kim, Shi et al. 2001)
			1980(Berber, Kwon et al. 2000)
	Graphite	2.09-2.23	5.5 (y-plane), 1000(x-plane) (Delhaes 2000)
	SiC	3.97	35.5 (Xie, Wang et al. 2001)
oxide nanoparticle	CuO	6.31	33(Liu, Lin et al. 2011)
	Alumina	3.24	35.5(A.J.Moses 1978)
Heat transfer liquid	Water	1	0.6(Liu, Lin et al. 2011)
	Ethylene glycol	1.11	0.25(Eastman, Phillpot et al. 2004)
	Engine oil	0.82	0.145(Eastman, Phillpot et al. 2004)

Some models such as Hamilton-Crosser (1962) and Davis (1986) have been developed to fit the thermal conductivities of suspensions with micro particles.

Hamilton-Crosser model: $$\frac{k_e}{k_f} = \frac{\alpha+(n-1)-(n-1)(1-\alpha)\Phi}{\alpha+(n-1)+(1-\alpha)\Phi}$$

Davis model: $$\frac{k_e}{k_f} = 1 + \frac{3(\alpha-1)}{\alpha+2-(\alpha-1)\Phi}\left[\Phi + f(\alpha)\Phi^2\right] \quad (1.3)$$

Where k_e is the effective thermal conductivity of the mixture, k_f is the thermal conductivity of base fluid, α is the ratio of thermal conductivity of particle and base fluid, and Φ is the volume fraction of particles, f(α) was a complicated function to represent strong interaction between particles. n is the particle shape factor (n=3 for spherical particles), it is calculated by following formula (1.4)

$$n = 3\psi^{-1} \quad (1.4)$$

where ψ is the sphericity, defined as the ratio of the surface area of a sphere, with a volume equal to that of the particle, to the surface area of the particle. The ψ is always larger than 1 since the spherical particle has lowest surface area in all particles with the same volume. Therefore, the n is always less than 3.

Hamilton-Crosser model considered the effect of thermal conductivity ratio between particle and liquid, shape factor and volume fraction of particles. Davis model didn't consider the effect of shape factor while f(α) was introduced to represent interaction between micro particles.

Compared with micro-fluid that has mild increase on thermal conductivity, researchers have reported the surprising increase on thermal conductivities of nanofluids containing metal oxide (Lee, Choi et al. 1999, Murshed, Leong et al. 2005) and carbon material (Eastman, Phillpot et al. 2004, Wensel, Wright et al. 2008), even though the volume fraction of nanoparticles is very small. The Hamilton-Crosser and Davis model usually underestimated the abnormal enhancement. The experiment studies on thermal conductivities of non-metallic nanofluids were reviewed in section 1.2.2. The effect of some factors such as loading level of nanoparticles, particle size and shape were also discussed in this section. The main mechanisms behind the enhancement of thermal conductivity were presented in section 1.2.3.

1.2.2 Experiment studies

Metal oxide nanofluid

Copper oxide (CuO, k=33 W/mK) and Alumina (Al_2O_3, k=25 W/mK) are the common candidates to form metal oxide nanofluid. Jwo et al (Jwo, Teng et al. 2005) reported the enhancement on the thermal conductivity of CuO (85nm)/water nanofluids. The enhancements of thermal conductivities were 5.8% and 9.6% with the nanoparticle loading levels of 1.1 vol % and 2.2 vol %. Lin et al. (Liu, Lin et al. 2006) obtained similar result from the same system. 22.4% enhancement was observed at the volume fraction of 5 vol % CuO nanoparticles. Hwang et al. (Yoo, Hong et al. 2007) measured thermal conductivities of TiO_2 (25 nm) and Al_2O_3 (48 nm) nanofluids and obtained high enhancements as well. All results verify that the addition of metal oxide nanoparticle can increase the thermal conductivities of convention heat transfer liquids. However, some opposite result are also reported, Zhang et al. (Zhang, Gu et al. 2007) observed no apparent enhancement on thermal conductivity of Al_2O_3, TiO_2 and CuO nanofluids.

The relation between the enhancement and volume fraction of nanoparticles is usually linear while Zhu et al (Zhu, Zhang et al. 2006) found non-linear effect of nanoparticles' loading level and explained the behavior via nanoparticle clustering mechanism. The effect of particle size was also studied. Mashuda and Ebata (H.Masuda and Ebata 1993) reported 30% enhancement on thermal conductivity of water by adding 4.3% of Al_2O_3 (12 nm). Lee et al. (Lee, Choi et al. 1999) observed 10% enhancement at the same volume fraction for 38 nm Al_2O_3. Xie et al. (Xie, Wang et al. 2002) found the enhancement increases firstly and then decreases with the particle size increases. 25 nm Al_2O_3 nanoparticles give highest enhancement to Al_2O_3/water system. However, Kim et al. (Kim, Choi et al. 2007) found no very strong dependence of enhancement on particle size for TiO_2 (10, 35 and 70 nm) and ZnO (10, 30 and 60 nm) system. There are papers discussing the effect of nanoparticles' shape except for Murshed et al. (Murshed, Leong et al. 2005). They measured the thermal conductivity of aqueous solution of spherical and cylindrical TiO_2 nanoparticles. The 15 nm spherical TiO_2 have slightly less enhancement than that of 10 nm×40nm size nanorods. It is consistent with theoretical predication because nanorod has different shape factor with spherical nanoparticles.

Carbon material nanofluid

The very large intrinsic thermal conductivity of carbon nanotube (CNT) from 900 W/mK (Kim, Shi et al. 2001) to 1980 W/mK (Berber, Kwon et al. 2000), lower densities (1.3-1.4g/cm^3), and larger aspect ratio compared with metals and oxide nanoparticles, makes it an attractive candidate for nanofluids. Choi et al (Choi, Zhang et al. 2001) dispersed MWNTs to base oils and found 160% enhancement of thermal conductivity with only 1 vol% of carbon nanotubes. Assael et al (Assael, Chen et al. 2004) observed the thermal conductivity of aqueous carbon nanotube dispersions increase up to 38% at 0.6 vol% of CNT. These enhancement was very surprising and nonlinear with volume fraction of CNT compared to the linear relation in metallic or ceramic nanofluids (Wen and Ding 2004).

Other carbon nanomaterials such as carbon black, graphite and silicon carbide were also used to create nanofluids with high thermal conductivities. Although their enhancement is milder than that of carbon nanotube, they are easier to disperse by surface modification and their nanofluid has better rheological behavior. Wanga et al (Wanga, Wanga et al.

2012) studies the enhancement on thermal conductivity via addition of graphite. The enhancement varies from 11% to 36%, when the amount of graphite increases from 0.68 to 1.36 vol. %. It can be attributed to formation of percolating aggregate structures. Xie et al. prepared Silicon carbide (SiC, k=35.5 W/mK) (Xie, Wang et al. 2001) nanofluid with particle size ranging between 26 and 600 nm and observed the enhancement on thermal conductivity.

1.2.3 Mechanisms of thermal conductivities of nanofluids

Some mechanisms have been developed to interpret the enhancement of dispersion with nanoparticles. The main mechanisms comprise Brownian motions, interfacial resistance, and nanoclustering and percolation mechanism.

<u>Brownian motion of the nanoparticles</u>

Heat transfer can happen directly between nanoparticles when they collide by motion, especially by Brownian motion. However, Keblinski et al. (Keblinski, Phillpot et al. 2002) pointed out the heat transfer via Brownian motion of nanoparticles is much slower than via thermal diffusion in liquid. Therefore, Brownian motion doesn't contribute significantly enhance the thermal conductivities of nanofluids. Instead of nanoparticle collision, Jang et al. (Jang and Choi 2004) postulated that Brownian motion of nanoparticles lead to some local convention effect. Based on the local convection hypothesis, a theoretical model was created to predict the effective thermal conductivity k_e of spherical nanoparticle dispersions.

$$k_e = k_f(1-\Phi) + k_p\Phi + 3C_1\frac{d_f}{d_p}k_f Re_{d_p} Pr\Phi \qquad (1.5)$$

Where subscript "f" and "p" represents base fluid and nanoparticle, d is diameter, C_1 is proportional constant and Pr is Prandtl number of nanofluids. Re_{d_p} is defined as

$$Re_{d_p} = \frac{Cd_p}{\nu} \qquad (1.6)$$

In which C and ν are the random motion velocity of nanoparticles and dynamic viscosity of the base fluid.

The model based on Brownian motion predicted the thermal conductivity enhancement increases with the nanoparticle size decrease, because the high surface area increases the local convection in nanofluids (Kumar and Patel 2004, Chon, Kihm et al. 2005). This tendency has an agreement with some experimental results. However, some work reported the enhancement on thermal conductivity increases when particle or agglomerates size increases. It may arise from the following two mechanisms: interfacial resistance and nanoparticle cluster.

Liquid layer around nanoparticles

Nanofluid was a system comprising solid nanoparticles and continuous liquid phases. Due to the differences on electronic and vibrational properties of particles and liquid, phonon attempting to traverse the interface will scatter at the interfaces. The scattering phenomenon leads to the interfacial resistance. Nan et al. (Nan, Birringer et al. 1997) addressed the effect of interfacial resistance on thermal conductivities of particulate composites. They set up a theoretical model to predict thermal conductivity of composites by including interfacial resistance term into it. When k_f<<k_p, the model can be modified as following.

$$\frac{k_e}{k_f} = \frac{(1+2\varepsilon)+2\Phi(1-\varepsilon)}{(1+2\varepsilon)-\Phi(1-\varepsilon)} \qquad (1.7)$$

in which $\varepsilon = 2R_b k_f/d_p$, subscript e, f, p represents effective properties of nanofluids, base fluid and nanoparticle. d_p is the diameter of nanoparticle, Φ is volume fraction of nanoparticles, R_b is interfacial resistance.

Yu et al. (Yu, Richter et al. 1999) applied the interfacial resistance concept on solid-liquid system and verified that liquid molecules close to solid surface can organize into layered structure. Choi et al. (Choi, Zhang et al. 2001) pointed out that this mechanism may contribute to anomalous thermal conductivity enhancement in nanotube dispersions.

The model based on interfacial resistance gave two predictions. The first prediction was that the enhancement on thermal conductivity of nanofluid should increase when the nanoparticles' size increase. It seems to contradict most experimental results. However, Keblinski (Keblinski, Phillpot et al. 2002) indicated that the thickness of the interfacial solid-like layer thickness was only on the order of a few atomic distances. This mechanism only dominated thermal conductivity at very small nanoparticles (<10 nm). So when the particle size increases from some nanometers to dozens of nanometers, thermal conductivity increases due to the interfacial resistance mechanism. If the particle size increases continually, the thermal conductivities of nanofluids should decrease due to slower Brownian motion. Prasher et al. (Prasher, Bhattacharya et al. 2005) proposed a model combined Brownian effect and interface resistance.

$$\frac{k_e}{k_f} = \left(1 + ARe^m Pr^{1/3} \Phi\right) \frac{(1+2\varepsilon) + 2\Phi(1-\varepsilon)}{(1+2\varepsilon) - \Phi(1-\varepsilon)} \qquad (1.8)$$

in which $\varepsilon = 2R_b k_f / d_p$, subscript e, f represents effective properties of nanofluids, base fluid. d_p is the diameter of nanoparticle, Φ is volume fraction of nanoparticles, Re is defined as

$$Re_{d_p} = \frac{Cd_p}{\nu} \sqrt{\frac{18k_bT}{\pi\rho_p d_p}} \qquad (1.9)$$

It gave good fit to experimental result from Xie Wang et al. (Xie, Wang et al. 2002), showing the enhancement has a maximum value with 25 nm Al_2O_3.

The second prediction from interfacial resistance mechanism was that interfacial tension will influence the enhancement on thermal conductivities of nanofluids. The simulation work by Xue et al. (Xue and Keblinski 2003) indicated that the strength of bonding between liquid and solid was very important in determining interfacial thermal resistance. The result shows the nanofluids with weak atomic bonding at interface exhibit high thermal resistance. Wetting procedure under the help of surface modification can decrease the interfacial thermal resistance. Shenogin et al. (Shenogin and Xue 2004) verified adding dispersant into dispersion systems will change the atomic bonding at interface and surface treatment can lead to varied interfacial resistance.

Nanoparticles clustering and percolation threshold

Nanoparticles with large surface energies like to connect each other to decrease surface energy, which lead to formation of many small clusters i.e. agglomerates. The small clusters in diluted nanofluid can still be stable in liquids and will function as good thermal conductors. Keblinski et al. (Keblinski and Phillpot 2001) showed that the local nanoparticle clustering is another possible mechanism of the abnormal enhancement on thermal conductivity. They suggested that the volume fraction of clusters is larger than the volume fraction of pure nanoparticles because clusters contain both nanoparticles and base liquid

The “amplifying” effect on volume fraction was obvious when the packing factor of cluster is low. The author also pointed out that clusters existing in the dispersion may cause the settlement of nanoparticles or creating particle-free regions with high thermal resistance. However, the authors didn’t consider the complex thermal conductivity of cluster. It may be lower than close-packed nanoparticles since more base liquid fills the channel between nanoparticles.

For concentrated nanofluids, the small clusters and large agglomerates formed by nanoparticles have higher opportunity to connect each other. Some properties such as thermal conductivity, heat transfer and viscosity will change substantially. The percolation threshold concept was introduced to describe the behavior. When the volume fraction exceeds the percolation threshold, the strong long-range connectivity happens between clusters, even forming three dimensional network structures in the nanofluids then changes the properties of the base fluids substantially. The percolation threshold is strongly dependent on the aspect ratio of nanoparticles. Equation 1.10 shows an empirical formula (Garboczi, Snyder et al. 1995) developed to predict the percolation threshold,

$$Pc = \frac{9.875A_f + A_f^2}{7.742 + 14.61A_f + 12.33A_f^{1.5} + 1.763A_f^2 + 1.658A_f^3} \tag{1.10}$$

Where P is the percolation threshold, A is the aspect ratio of nanoparticles. The calculated relation between percolation threshold and aspect ratio is plotted in Figure 1.5 (Garboczi, Snyder et al. 1995).

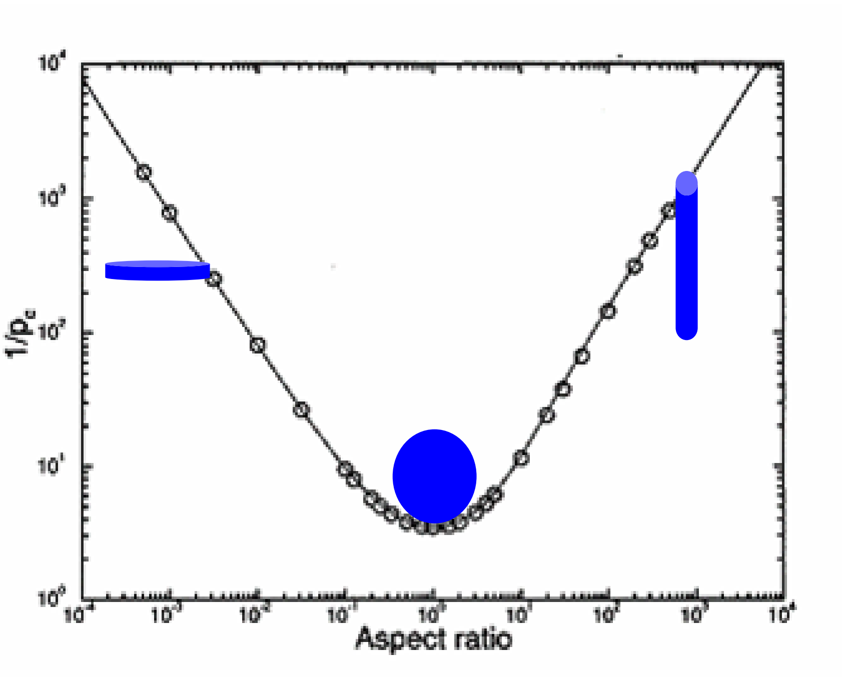

Figure 1.5 Relations between the inverse of percolation limit and the aspect ratio.

The figure shows that spherical particles (aspect ratio=1) must be closely packed in order for the particles to contact each other and form consistent thermal conduction pathways through the dispersion. non-spherical nanoparticles like nanotubes or nanowires with high aspect ratio and nanodisks with low aspect ratio will have much lower maximum packing fraction than spherical nanoparticles (Wierenga and Philipse 1998, Yamamoto and Matsuoka 1999, Chen, Ding et al. 2007). Therefore, the nanotube and nanodisk exceed the percolation threshold at much lower volume fraction. Above the percolation threshold, they form three dimensional networks, which lead to abnormal enhancement on thermal conductivities of nanofluids. Meanwhile it wound change the rheological behavior as well, discussed in next section.

There are only a few papers comparing on thermal conductivity between nanofluid with neat and surface-modified nanoparticles. Actually, surface modification will change the size of clusters and agglomerates, and interfacial tension between nanoparticle and base liquid. The size of clusters and agglomerates will influence enhancement of thermal conductivity via Brownian motion and nanoparticle clustering mechanism. The change on interfacial tension will also influence enhancement via interfacial resistance mechanism. Xie et al (Xie, Lee et al. 2003) dispersed CNTs that are functionalized by concentrated nitric acid in polar liquids like water and into decene ($C_{10}H_{20}$) with surfactants like oleyamine. They reported 10%-20% increase in thermal conductivity with 1 vol% CNTs; it is much lower than 160% enhancement of previous result. Therefore, our research expects to do measurements on graphite and silicon carbide dispersions and clarify the effect of surface modification on enhancement of thermal conductivity.

1.3 Rheological behaviors

Emphasizing on the enhancement of thermal conductivity alone is not enough for developing practical high heat transfer nanofluids. Rheological properties are also important from three aspects. Firstly, many results certified the enhancement of thermal conductivities with very small volume fraction of nanoparticles while their viscosity also increases dramatically, often leading to more non-Newtonian behavior (Yang, Grulke et al. 2006, María Jose Pastoriza-Gallego 2011). Both the increases on thermal conductivity and viscosity influence the heat transfer coefficients of dispersions. The second reason was that the drive force for heat transfer fluid in engine or pipeline was related to viscosity of nanofluid. For keeping the same volumetric flow rate, the engine of motor vehicle has to support more driving force to overcome the pressure losses on high viscosity fluid. That situation increases the power cost and decreases the life of engine. The third reason was that rheological studies have been useful to analyze micro-structure like agglomerates and aggregates in nanofluid (Yang, Grulke et al. 2005). Therefore, the important studies about rheological behaviors of nanofluids were summarized in this section.

1.3.1 Nanofluid with spherical nanoparticles

The rheological behavior of metal oxide nanofluid is closely associated with the volume fraction of nanoparticles. In dilute nanofluid, there are only weak interactions between metal oxide nanoparticles. Therefore, the Einstein formula used for predicting hard sphere suspension, and Batchelor formula including weak interactions can fit the linear relation well

$$\text{Einstein formula:} \quad \eta = \eta_0(1 + 2.5\Phi)$$

$$\text{Batchelor formula:} \, \eta = \eta_0(1 + 2.5\Phi + 6.2\Phi^2) \qquad (1.11)$$

The models predicted viscosity increases that were not remarkable and nearly linear with volume fraction of nanoparticles. The nanofluid shows nearly Newtonian behavior that the viscosity of dispersion doesn’t change with shear rate increases. The small increase of viscosity and Newtonian behavior had been verified in the dispersion with 1~4% Al_2O_3

nanoparticles (38 nm) dispersed in water (Das, Putra et al. 2003). However, the viscosity of Al_2O_3 (28 nm) nanofluid increases about 30% when volume fraction of alumina increases to 3%. The studies on the CuO nanofluid by Chang et al (Chang and Jwo 2005) found the viscosity of nanofluids increased with decrease of particle size. These results illustrate the influence of particle size on the viscosity.

For concentrated nanofluids, the interactions between nanoparticles are strong and complicated. The viscosity increase becomes obvious and the rheological behavior becomes non-Newtonian. The viscosity at high shear rate could be described by Krieger-Dougherty model (K.Gupta 2000).

$$\text{Krieger-Dougherty model:} \qquad \eta = \eta_0 \left(1 - \frac{\Phi}{\Phi_m}\right)^{-[\eta]\Phi_m} \qquad (1.12)$$

Where η is the shear viscosity of dispersion, η_0 is the shear viscosity of base fluid, Φ is the volume loading of nanoparticles, $[\eta]$ is the specific viscosity and Φm is the maximum packing fraction.

Tseng and Lin (Tseng and Lin 2003) investigated the rheological behavior of anatase/water nanofluids at shear rate of 10-1000s^{-1}. A shear-thinning behavior, which indicated the existence of agglomerates, was observed in most nanoparticle dispersion. Some researches focused on effect of dispersant and surface treatment on viscosity increases. Zamen (Zaman and Singh 2002) studied the effect of cationic surfactant on silica nanofluid. They found when the surfactant concentration was over a critical level, dispersion viscosity dropped significantly and the dispersion exhibited linear viscoelastic properties. Anoop et al (Anoop, Kabelac et al. 2009) studied the effect of surface charge on viscosity increase and reported the electrical double layer formed via surface modification has addition electro-viscous effect on increase on viscosity. Shi et al. (Shi and Wu 2003) studied the effect ammonium polyacrylate, a long-chain dispersant supplying both electrostatic and steric exclusion. The addition of dispersant decreased the viscosity of nanofluid dramatically and the rheological behavior is dependent on the amount of dispersant adsorbed on the nanoparticles' surface. The effect of same dispersant on $BaTiO_3$ nanofluid are studied by Shen et al. (Shen and Chen 2004). Similar results were reported.

1.3.2 Nanofluid with non-symmetric nanoparticles

The relation of aspect ratio, percolation threshold and thermal conductivity has been discussed. The effect of aspect ratio on viscosity of nanofluid is similar. High and low aspect ratios both lead to low percolation threshold (Heine, Petersen et al. 2010). The viscosity increase substantially when volume fraction exceeds the percolation threshold. Carbon nanotube is an example. Carbon nanotube dispersions have much higher viscosities than base fluids and show obvious non-Newtonian behavior in spite of low volume fractions (Ding, Alias et al. 2006, Yang, Grulke et al. 2006), shown in Figure 1.6. The addition of multi-walled carbon nanotubes (MWNTs) increase the viscosity of base oil (Polyolefin, PAO 6) over six orders of magnitude under low shear stress (about 0.1 Pa). The dispersion with MWNTs shows shear-thinning behavior as the shear stress increases. The two "plateau" regions indicate shear-dependent (and therefore unstable) structures existed in the dispersion.

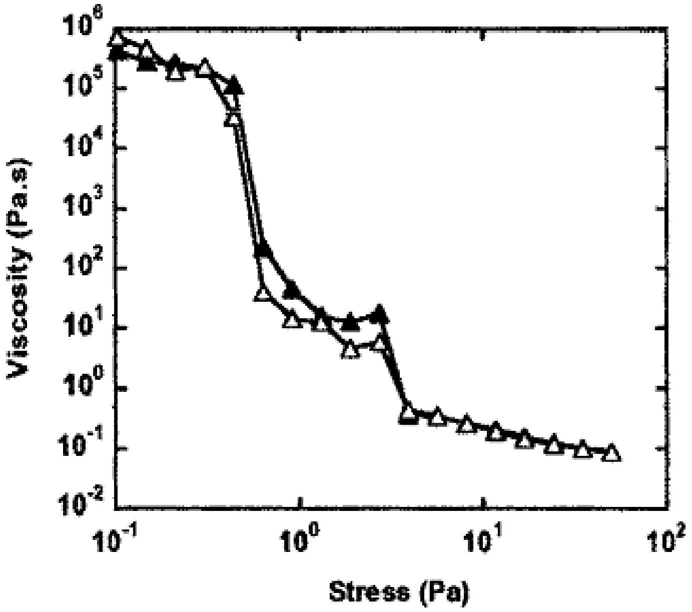

Figure 1.6 Viscosity of 0.12 vol% carbon nanotube dispersion in PAO 6 without dispersant.

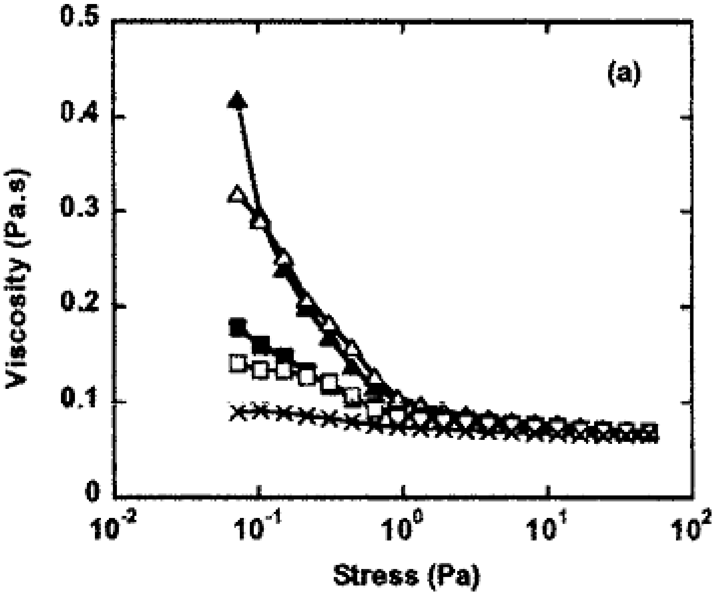

Figure 1.7 Effect of dispersant concentration on viscosity of 0.12 vol% carbon nanotube dispersions

(Labels: (▲) 0.3 wt%, (■) 1wt%, (×) 3wt%, (□) 5wt%, and (Δ) 8wt%.)

Ying et al also studied the dispersion of MWNT with different loading of dispersant shown in Figure 1.7(Yang, Grulke et al. 2006). They found the dispersions with highest (8 wt %) and lowest dispersant concentrations (0.3 wt.%) are both strongly shear thinning, while the dispersion with 3 wt% dispersants behaves like a nearly Newtonian behavior and minimum viscosity. At lower dispersant concentration, few PIBSI molecules are adsorbed to the surface of carbon nanotubes, the formed larger agglomerates lead to shear thinning behavior. As the concentration of dispersant increases, fewer agglomerates lead to decrease on viscosity and more Newtonian behaviors. At higher dispersant concentration, the bridging flocculation between PIBSI chains occurred. It also leads to shear thinning behavior.

Compared with studies on rheological properties of nanotube and nanorod dispersion, there are few papers about the rheological properties of nanodisks. Exfoliated graphite has nanodisk structure, low aspect ratio (l/d=0.02), high thermal conductivity and low density. It should be a good candidate to develop nanofluid. Therefore surface modification and its influence on thermal conductivity and rheological behavior of graphite nanofluid becomes topic of our first project.

1.4 Interaction with bio-macromolecules and nanotoxicity

1.4.1 Introduction

Complex engineered nanoparticles (CENPs), with nanoparticle as their core and some coatings formed via surface modification, are promising scaffolds for applications such as biomacromolecule receptors (Verma and Rotello 2005), biosensors (De, Rana et al. 2009), imaging indicators (Smith, Duan et al. 2008) and drug carriers (Davis, Chen et al. 2008). The common core material in CENPs include metal oxides such as alumina (Pailleux, Boudard et al. 2013), ceria (Yokel, Tseng et al. 2013), titania (Hund-Rinke and Klawonn 2013), zirconia (Smits, Liepins et al. 2012) and some carbon-based nanomaterials

(Shvedova 2010, Chen, Hu et al. 2012). Some of these nanoparticles inevitably entered biological and environmental media. As mentioned in previous chapters, nanoparticles have large surface areas and strong tendencies to adsorb and interact with biomacromolecules to decrease surface energy. Therefore, to study interactions between biomacromolecules and nanoparticles is crucial to evaluate the safety of nanoreceptors and nanocarriers. On the other hand, these metal oxide and carbon nanoparticles have low aqueous solubility, so they are likely to persist in biological and environmental systems for long time with potential to cause delayed toxicity (European Parliament 2006, Ai, Biazar et al. 2011, Zhan, Yanxia et al. 2011, Bimbo, Peltonen et al. 2012).

Studying the interaction and bio-persistence of core nanoparticle alone is not enough. The coating material formed in synthesis or surface modification can alter surface physical and chemical properties, manipulate interactions between core nanoparticles and biomacromolecules, and increase the stability of dosing dispersion. Some prior studies have verified the coatings can interact with organisms in tissue and environment (Cedervall, Lynch et al. 2007, Lynch and Dawson 2008, Wang 2012) and may induce some unanticipated toxicological outcomes *in vitro* (Ould-Moussa, Safi et al. 2013), *in vivo* (Seok, Cho et al. 2013), and in the environment (Hoecke 2009). Sandhu et al. (Sandhu, McIntosh et al. 2002) reported that a quaternary ammonium coating with positive charge can inhibit DNA transcriptions and Fischer et al. (Fischer, McIntosh et al. 2002) reported that a negative carboxylic coating can inhibit the enzyme activity of α-chymotrypsin. The effect of surface charge was emphasized by researchers but quantitative analysis about the effect was missing so far.

To create a nanosystem with both peculiar capabilities and low toxicity for reducing the potential biological environmental impact, it is essential to study the interaction between differently charged CENPs and proteins quantitatively. A new characterization method to study bio-distribution of CENPs in different organs should be also necessary to develop.

1.4.2 Interaction between nanoparticles and protein

Verma et al. (Verma and Rotello 2005) reported the surface coating of CENPs can works as receptor due to their strong interaction with DNA and protein molecules. Li et al (Li, Chen et al. 2012) have investigated the toxicity of seven different types of neat engineered metal oxide NPs against Paramecium multi-micronucleatum. The results showed metal oxide NPs strongly associated with the cell membrane, inducing more severe cytotoxicity. The toxicity increased as follows: $Al_2O_3 < TiO_2 < CeO_2 < ZnO < SiO_2 < CuO < Fe_2O_3$. Sund et al (Sund, Alenius et al. 2011) investigated the adsorption of proteins onto eleven thoroughly characterized engineered nanoparticles. All kinds of tested nanoparticles were taken up by primary macrophages and epithelial cells in rats' lungs. Fibrinogen chains were attached to all nanoparticles after exposure to plasma proteins. Pulmonary surfactant components adsorbed on the nanoparticles' surface and significantly reduced the overall protein adsorption. The results verified the strong interaction between protein molecules and nanoparticles, and the effect of surfactant.

Some researchers investigated the effect of ceria ($CeO_{2-}\mathbf{x}$) in biological media. Ceria, a rare earth metal oxide with two oxidative states of cerium, Ce (III) and Ce (IV), possesses unique chemical properties in a redox reaction (Land 1973, Suzuki, Kosacki et al. 2001). Recently, nanoceria has been found to scavenge reactive oxygen species and has been proposed as an antioxidant to promote organism longevity. Rzigalinski et al. reported that ceria nanoparticles (NPs) of the size range of 6-20 nm prolong the lifespan of mixed brain cell cultures (Rzigalinski 2005). Tarnuzzer et al. reported that nanoceria provide radioprotection to normal cells from radiation (Tarnuzzer, Colon et al. 2005). These findings show that ceria is a potential candidate for antioxidant and radio-protective applications.

However the scavenge of free radicals and interact with protein may co-exist in cells. Schaefer et al. (Schaefer, Schulze et al. 2012) compared the binding capacity of BSA on silica and ceria nanoparticle via Atomic Force Microscope (AFM) measurement and found ceria has much higher interaction with BSA than silica. Wang et al. used dextran and PAA coatings to stabilize ceria nanoparticles and found they can inhibit the growth of bacterial cells. The reason was likely that the interactions between nanoparticles and some specific proteins on the bacterial cell membranes alter the permeability of the cell membranes. In the interactions between ceria nanoparticles and protein, adsorption of protein molecules on the nanoparticles' surface was essential and needed more investigation.

The adsorption behavior of protein on coated ceria nanoparticles' surface was complicated. Previous research focused on the adsorption of proteins to neutral, or their oppositely charged surfaces to form protein coronas (Lynch and Dawson 2008). The electrostatic attractive force or Van der Waals force were main factors and the adsorption behavior can be fitted by Langmuir isothermal well, which usually describe adsorption on homogenous surfaces (Asthagiri and Lenhoff 1997, Xu and Lenhoff 2008). However, an electrostatic attraction is not always adequate to capture all adsorption behavior and most adsorption behavior is heterogeneous. Three other factors need to be addressed: local energy distribution, charge distribution in protein via conformation/orientation, and possible lateral effect between adsorbed, neighboring and following protein molecules.

Local energy distribution: the energy distribution on nanoparticles' charged surface is not uniform due to the surface heterogeneity and curvature. Some sites on the surface have higher binding energy change after adsorption. These sites are more active, and then solute is usually adsorbed on them first. Some researchers have created an estimation method for energy distribution in gas-solid system (Cerofolini 1974, Kumar, Monteiro et al. 2011) and adsorption of humic acid on activated carbon (Carter 1995).

Charge distribution in protein via orientation: the protein molecules always have both positive and negative charged segments. It can adsorb on both negative and positive surfaces via change of conformation and orientation, but can have preferred orientations for a specific surface. The orientation change has been modeled by Brownian dynamics (Ravichandran, Madura et al. 2001, Ermakova 2005) and Monte Carlo simulations (Zhou, Chen et al. 2003, Zhou, Tsao et al. 2004, Xie, Zhou et al. 2010). Experimentally, the surface charge distribution of lysozyme has been shown to affect its orientation in adsorption procedure (Tiemeyer, Paulus et al. 2010). The different orientation will influence the monolayer adsorption amount.

The lateral interactions between adsorbed and following protein molecules are also important (Al-Muhtaseb and RItter 1999, Podkoscielny 2008). When a solute adsorbs on a heterogeneous surface, it may not readily de-adsorb or be displaced by competing solutes, thus modifying the surface for the uptake of following species. The adsorbed molecules can have attractive forces (positive cooperative effect) or repulsions (negative cooperative effect) to following molecules. It will influence the shape and slope of adsorption curve.

In our project, ceria nanoparticles with different surface charges and lysozyme were chosen to study. Toth and Sip models were applied to fit adsorption behavior. The energy distribution, orientation of lysozyme and lateral effect were discussed. The detailed description of this study was in Chapter 4.

1.4.3 Bio-distribution and bio-persistence of nanoparticles

Seok et al. (Seok, Cho et al. 2013) investigated the bio persistence of Zinc oxide (ZnO) nanoparticles in mice after 13 weeks. Zinc oxide usually exists in paints, cosmetics and food. They found the zinc ion formed after ingestion of zinc oxide nanoparticles play key role on their toxicity while no obvious adverse effect level of ZnO NPs was observed.

Yokel et al (Yokel, Au et al. 2012, Yokel, Tseng et al. 2013) found that the rat's body burden of a 30 nm ceria ENM dose did not significantly decrease up to 90 days after a single intravenous administration. Hirst et al. studied the bio-persistence of ceria in organs of mice and got similar results (Marie, Ajay et al. 2011).

As mentioned before, the biodistribution and biopersistance of CENPs in biological media depends not only on the physico-chemical attributes of the core nanoparticle (size, size distribution, shape), but also their surface-bound molecular coatings. A pharmacokinetics study of the distribution of ceria nanomaterials in blood showed that, on clotting, both 15- and 30-nm ceria samples partitioned to the clot fraction, rather than the serum, over time (Hardas, Butterfield et al. 2010). The clot contains most cells, platelets and protein. This partitioning performance may result from changes in their surface chemistry, such as loss of the surface coating. Therefore, finding a method to trace the transformation of both core and coating material was necessary.

The common characterization methods for biodistribution of nanoparticle are High Resolution Transmission Electron Microscopy (HR-TEM) and ICP-MS. The previous can give good morphology information but it is difficult to do quantitative analysis. The latter is difficult on tracing the organic component. Some methods based on radioactive isotope are proposed. Perez et al. (Perez-Campana, Gomez-Vallejo et al. 2013) applied direct proton beam activation method on aluminum oxide NPs. ^{13}N-labeled alumina nanoparticle formed by proton beam activation can show the distribution of them in different organs. It verified the alumina nanoparticles like to accumulate in liver. The method can't supply distribution information after long time the since the half-life of 13N (9.97 min) is very short. Rojas et al. (Rojas, Gispert et al. 2012) used ^{18}F isotope to label the amino coating on ceria nanoparticles and showed that of ceria accumulated mainly in lungs, spleen, and liver. However, labeling only the coating or core material was not enough because the coating on surface is likely to dissociate, degrade or transport in biological media.

Using one isotope tracer on core material and the other on coating material was proposed by us. After the CENPs have been distributed in different organs, Accelerator Mass Spectrometry (AMS) was used to measure the amount of stable isotope. AMS can separate rare isotopes with high selectivity and high sensitivity via extraordinarily high kinetic energies. It detected such species at levels 10^3 to 10^9 times lower than other methods (Barker and Garner 1999) and has been applied to tracing biomacromoles (Ognibene and Vogel 2004). Therefore, the amount in dosing material and different tissue measured by AMS can give information about transporting properties of CENPs. Moreover, it should be possible to identify changes in the molar ratios (coating/core) after the dosing entering into biological media and metabolism. This technology will directly give understanding on the potential toxic of CENPs from where they go, how long they stay there, and are they transformed during these processed. The detailed description of this methodology and analysis is in Chapter 5.

1.5 Dissertation Overview

After summarizing the prior studies, the dissertation would explore further the effect of surface modification on properties and applications of CENPs. It comprises four aspects: 1) Modify carbon nanomaterials' surface and investigate the effect on thermal and rheological behavior of their dispersions; 2) Generate self-assembly bi-layer structure of oxide nanoparticles via surface modification; 3) Study interaction between lysozyme and different surface-charged ceria nanoparticles; 4) Trace biodistribution and transformations of CENPs in biological media via radioactive isotopes tracers.

Chapter 2 focused on the new and environmentally-friendly method we developed to convert the surface of graphite and silicon carbide (SiC) to hydrophobic surface. The thermogravimetric analysis (TGA) method was used to estimate the surface density of hydroxyl groups. SiC was found to have enough hydroxyl groups therefore direct silanization was used to create alkane chain. The graphite was verified to be short of reactive groups on surface so citric acid was used to generate hydroxyl surface groups firstly. The surface modification was verified to offset the formation of agglomerates in their dispersion. It lead the changes on thermal conductivity and rheological behavior. One combined model was built to fit and interpret the interesting results. The competitive effect between Brownian motion and nanocluster mechanisms was also discussed.

Chapter 3 focused one novel method to construct bi-layer structure of oxide nanoparticles with different refractive index such as silica and titania, which was crucial for optical thin films. There are always some hydroxyl groups on the surface of silica and titania nanoparticles. Silanization was used to transform their relatively hydrophilic surface to hydrophobic surface via attaching alkane chains. TGA method was also used to estimate the amount of needed silane and evaluate the hydrophilic/hydrophobic properties of modified surfaces. In spin-coating process, the neat nanoparticles keep in hydrophilic monomer while surface-modified nanoparticles settled down. The bi-layer structure was created via self-assembly separation in the single deposition process.

In chapter 4, the adsorption behaviors of lysozyme, one protein with net positive charge, on different surface-charged ceria nanoparticles were investigated. The adsorption isotherm curves were fitted with the Toth and Sips equations satisfactorily. The estimations on the monolayer coverage suggest there is orientation change on different charged surfaces. The heterogeneity parameters obtained from Toth and Sips models suggest the surface charge predominate adsorption on negatively charged ceria while lateral effect predominate adsorption on positively charged ceria. Estimation of local site energy distributions was also achieved via heterogeneity parameters and monolayer coverage amount.

Chapter 5 discussed the evaluation and characterization on the bio-distribution, translocation, and persistence of CENPs. The ^{26}Al-labeled nanoalumina, coated by ^{14}C-labeled citrate, was synthesized through hydrothermal and pH control. It dispersion was infused intravenously into rat. The Accelerator Mass Spectrometer (AMS) was used to measure amount of isotope in dosing material and tissues. The ratio of coating and core in liver was slightly less than dosing material while the ratios in brain and bone are much higher than dosing material. It may suggest some citrate coating dissociate from nanoaluminas' surface, entered metabolic cycles then redistributed to other tissues.

Chapter 2: Surface modification of graphite and silicon carbide nanoparticles and properties of their dispersions

2.1 Highlights

- Surfaces of graphite nanodisks and silicon carbide nanoparticles were modified via citric acid-silane method
- TGA was used to evaluate original surfaces and surface modification effect.
- A combined model was built to fit non-linear relation between thermal conductivity and volume fraction of nanoparticles
- The effect of shape and size of agglomerates on thermal conductivities was discussed
- Effect of surface modification on rheological behavior was investigated.

2.2 Introduction

Improving the heat transfer properties of heat transfer fluids via adding solid material with high thermal conductivity has been developed and studied for many years. Some researchers have reported surprising increase on the thermal conductivities of carbon nanotube dispersions (Assael, Chen et al. 2004, Wensel, Wright et al. 2008), even though the volume fraction was very small (<1 vol%). However, the previous studies by our group reported that the dispersions of carbon nanotubes also have abnormal increase on viscosity and strong non-Newtonian behaviors (Yang, Grulke et al. 2005, Yang, Grulke et al. 2006). The results can be linked to the very low percolation threshold for carbon nanotube due to very high aspect ratio.

Graphite and silicon carbide nanoparticles were chosen as the discontinuous phase for this project because these nanoparticles provide balance of thermal conductivity, rheological behavior and cost of product. They have relatively low densities and high thermal conductivities. The low densities lead to the nanoparticles with low settling rates and large volume fraction when the same mass was added. The thermal conductivity parallel to the basal planes in graphite is typically >1000W/mK although the property taken perpendicular to the basal planes is just 6 W/mK (Delhaes 2000). The observed thermal conductivity can sometimes be represented as the geometric average (~75 W/mK). The thermal conductivity of silicon carbide is 35.5 W/mK. Both values are much higher than the thermal conductivity of conventional heat transfer oils (around 0.145 W/mK). However, the surfaces of graphite (nearly no functional groups) and SiC (some hydroxyl groups) are not wetted well by nonpolar base fluids, increasing their tendency to agglomerate and settle from solution.

The most commonly reported surface modification method for inert carbon nanoparticles is to use strong oxidants such as potassium permanganate (KMnO4) or concentrated nitric acid (HNO3) in the presence of concentrated sulfuric acid strong oxidation (G.I. Titelman, V. Gelman et al. 2005). The method can create carboxylic groups, supplying negative charges via dissociation (Shaffer, Fan et al. 1998, G.I. Titelman, V. Gelman et al. 2005). A hydrofluoric acid (HF) etching method was used to create more hydroxyl and carboxyl groups on SiC surfaces (Alekseev, Zaitsev et al. 2007, Che, Wang et al. 2007, Schoell, Hoeb et al. 2008). These surface modifications require complicated protocols and the chemicals used are strongly corrosive. Some researchers developed a novel method that citric acid (CA) was used to create hydroxyl group and carboxylic groups on carbon nanotubes and carbon black (Chee Kok Poh 2008, Poh, Lim et al. 2008). The carboxylic groups on the surface provide electrostatic stabilization and can help disperse carbon nanoparticles in highly polar fluids like water. However, the method has limited value for nonpolar liquids. Steric stabilization was more useful in applications that require nonpolar continuous phase. The reaction between surface hydroxyl groups and active groups such as chloro, methoxy, ethoxy, in silane coupling agents can create oligomer or polymer chains on nanoparticles' surface. The chains increase the association between nanoparticle and nonpolar continuous phase and create steric exclusion coatings, which can reduce or prevent agglomerates between nanoparticles.

The combined citric acid method plus silanization were used in our project. Graphite nanodisks were treated with citric acid to generate surface hydroxyl groups. The generated hydroxyl groups reacted with chloro-silane with alkane chains without pre-hydrolysis to get alkane grafted graphite. SiC nanoparticles can react with silane directly to created alkane chains on surface because there were some levels of surface hydroxyl groups on its surface. The original surface density of hydroxyl groups, alkane chains, conversion degree and surface coverage of functional groups were estimated using the thermo-gravimetric analysis (TGA) technique. The surface modifications influence the size and aspect ratio of agglomerates in dispersion. Their effects on thermal conductivities and rheological behavior of dispersion were discussed.

2.3 Experiments

2.3.1 Surface modification of graphite and SiC nanoparticles

Scheme 2.1 shows the surface modification procedure for graphite nanodisk and SiC nanoparticles.

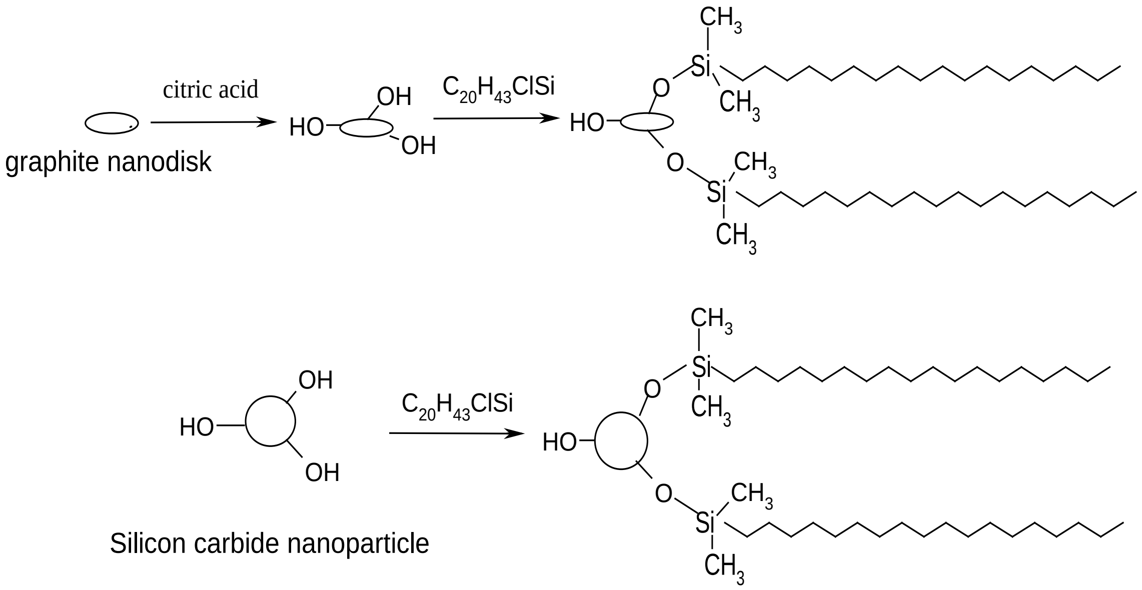

Scheme 2.1 surface modification for graphite nanodisks and SiC nanoparticles

The surface modification procedure for graphite nanodisks had two steps. In the first step, the citric acid was expected to etch the nanoparticle, creating some hydroxyl groups (simple hydroxyl groups and some in carboxylic groups) on the surface. In the second step, chloro-silanes containing alkane chains coupled directly to surface hydroxyl groups via the nucleophilic substitution. This step was in organic solvent and the silane didn't need partial-hydrolysis before reaction. The possibility of self-polymerization between partly hydrolyzed silanes was prevented via this improvement. There are two requirements for the nucleophilic substitution reaction (Kirk 2001). The first was that the chemical agent containing hydroxyl group in reaction mixture, nanoparticles in our case, must have a higher boiling point than the silane and solvent. The second was that the products (HCl, here) must be easily removed from the reaction system. Both of them were satisfied in our design.

4 g of citric acid monohydrate (Mallinckrodt Chemicals, MW=210.14) was added into 20 mL of distilled water to form an aqueous solution. 200 mg of graphite nanodisks (Graftech, supplied by Valvoline, Inc.) were dispersed into this solution under ultrasonication **(**Hielscher, UP 400s, 60% amplitude**,** 15 minutes**)**. This dispersion was the precursor to

citric acid-treated graphite. Another 200 mg of graphite nanodisks was dispersed into 20 mL distilled water under same ultrasonic agitation. The two dispersions were air-dried into pastes. The pastes were heated in an oven at 300 °C (above 175°C, the decomposing temperature of citric acid) for 30 minutes. The samples were washed by distilled water two times and by alcohol one time, and then dried in air. They are named “CA-graphite” (citric acid-treated graphite) and “neat graphite”. TGA technique was applied to measure the surface density of hydroxyl on these two samples. 200 mg CA-graphite was added into 20 ml toluene and dispersed under the same ultrasonication conditions. 193 mg of n-octadecyldimethyl-chlorosilane (Gelest Company, $C_{20}H_{43}ClSi$, MW=347.10) was dissolved in toluene to form a 10 wt% solution. The solution was added into graphite dispersion with stiring (400 rpm). The molar ratio of chloro group in silane to hydroxyl group on CA graphite) was 5:1 based on TGA result. The mixture was stirred and refluxed for 12 hours. The product was rinsed with toluene one time and hexane two times to remove the remaining silane and dried at 90°C for 12 hours. The dried sample was named AG-graphite (alkane-grafted graphite)

SiC nanoparticles (Nanoamor Company) were washed by water two times, ethanol one time and dried at 80°C for 12 hours. The dried sample was ground to fine powder and named “neat SiC”. 200 mg of neat SiC was was added into 20 ml toluene and dispersed under the same ultrasonication conditions. 0.58 gram of n-octadecyldimethyl-chlorosilane (Gelest Company, $C_{20}H_{43}ClSi$, MW=347.10) was dissolved in toluene to form a 20 wt% solution. The solution was added into SiC dispersion with stirring (400 rpm). The molar ratio of chloro group in silane to hydroxyl group on neat SiC was 5:1 based on TGA result. The mixture was stirred and refluxed for 12 hours. The product was rinsed with toluene two time and hexane one time to remove the remaining silane and dried at 90°C for 12 hours. The dried sample was named “AG-SiC” (alkane-grafted silicon carbide).

2.3.2 Nanoparticle characterization

The shape and morphology of graphite nanodisks and SiC nanoparticles were observed by Scanning Electron Microscope (SEM, Hitachi 4300, University of Kentucky) and Tranmission Electron Microscope (TEM, Hitachi 2010F, University of Kentucky). Fourier Transfer Infrared Spectroscopy (Nicolet™ iS™50 FT-IR Spectrometer, University of Kentucky) was used to detect the functional groups on nanoparticles' surface. Diamond Attenuated total reflectance (ATR) measure unit was used. All the samples were heated in vacuum oven at 120 °C for one hour to remove the water from them. Tiny amount of nanoparticles were put on the plate and screw was tight to press sample to thin pellet. The pellets were scanned by infrared from 400 cm^{-1} to 4000 cm^{-1}. Quantitation of surface groups was done by thermo-gravimetric analyzer (TGA 7, Perkin Elmer Corporation). The analyzer can record the weight loss from degradation and decomposition with temperature. In a nitrogen environment, all samples were heated from room temperature to 100 °C at rate of 10°C /min, kept at 100 °C for 30 mins to remove physically-adsorbed water and then heated from 100 °C to over 700 °C at rate of 10 °C/min. The degradation of all surface groups at such high temperature appeared to be complete.

2.3.3 Preparation and characterization of dispersions

Graphite dispersions with different volume fraction of graphite nanodisks were prepared by dispersing the neat graphite and AG-graphite samples into one kind of synthetic poly olefin oil (PAO 6, Chevron-Philips Company). The mixture was ultrasonicated for 15 mins to form dispersions. The volume fractions of graphite nanodisks range from 0 to 3.5 wt% (0 to 1.4 vt%) because the graphite settled down too rapid to measure the thermal conductivitiy when the volume fraction exceeded 1.5%. The SiC dispersions were prepared by the same dispersing method and weight concentration.

The size and aspect ratio of agglomerates in dispersion were photographed by optical microscope (Axiotech 100, Carl Zeiss Inc). The thermal conductivities of these dispersions were measured by hot wire method via thermal properties analyzer (KD-2 pro, Decagon Devices Inc). The samples were equilibrated above 15 mins to room temperature then are tested three times. The thermal conductivities used were the average value of all three trials. A coaxial cylinder rheometer (Viscoanalyzer, ATS Company) was used to measure the viscosity and rheological behaviors of these dispersions. The samples were loaded in the gap between rotary cylinder and the inner wall of container. They were equilibrated to 20 °C and tested under the shear rate varied from 0.5 to 1000 S^{-1}. At each point, the samples were equilibrated for 30-300s to ensure steady state and uniform conditions. The shear rate sweeps were repeated three times for each sample. The viscosity values used were the averages value of all three trials.

2.4 Results and discussions

2.4.1 Shape and morphology of graphite and silicon carbide nanoparticles

The SEM picture and size distribution curve of neat graphite nanodisks were shown in Figure 2.1 (a) and (b).

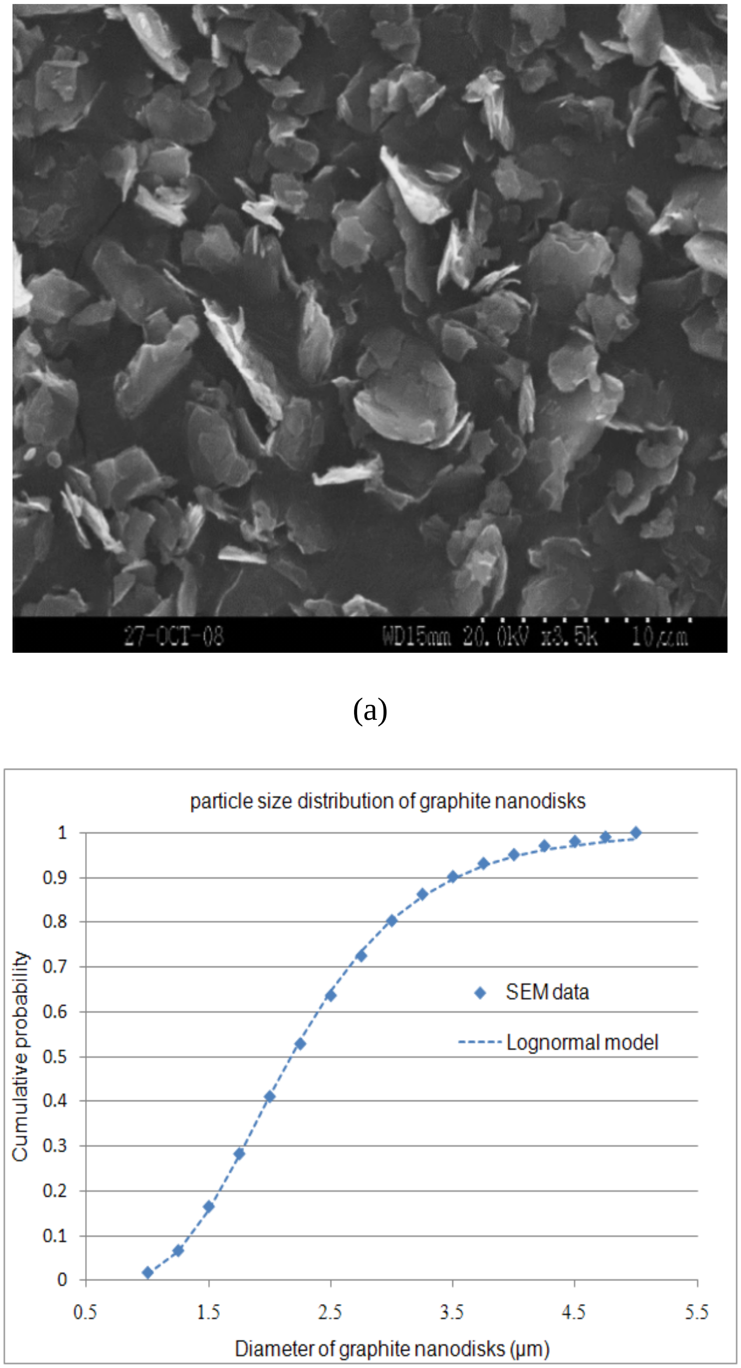

(a)

(b)

Figure 2.1 Morphology of neat graphite nanodisks, (a) SEM picture, (b) size distribution curve fitted by lognormal model.

Both single graphite nanodisks and multi-layer stacks can be observed in the Figure 2.1(a). 200 nanodisks and stacks of neat graphite were counted to calculate the size distribution. The result was fitted by lognormal model, shown in Figure 2.1(b). The average diameter given by the lognormal model was 2.33 μm and the thickness of single graphite nanodisk that was measured from some tilted graphite nanodisks was about 50 nm. The typical aspect ratio is 0.021 (thickness/diameter).

The TEM picture of neat SiC nanoparticles was shown in Figure 2.2. Most of them werespherical nanoparticle and their size was uniform. However, most discrete particles were agglomerated and aggregated into clusters. 100 spherical SiC nanoparticles in the SEM picture were counted. The average primary particle size is 18 nm.

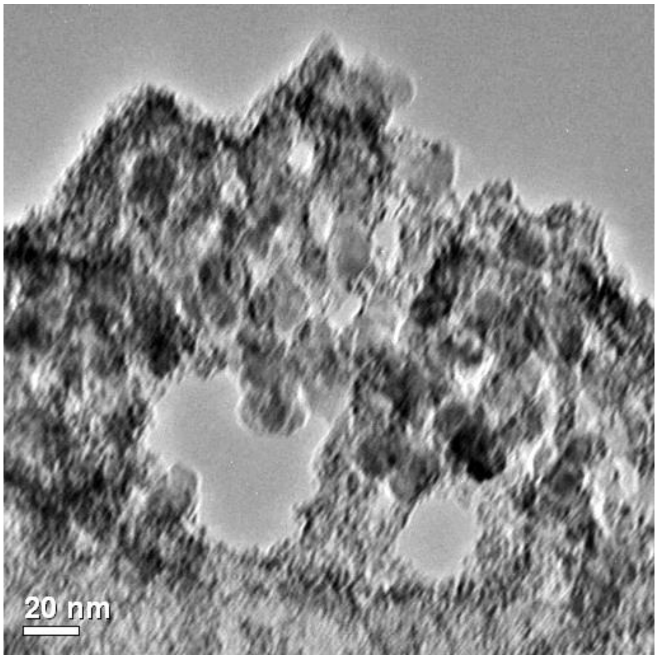

Figure 2.2 TEM picture neat SiC nanoparticles

2.4.2 FTIR analysis of surface modification effect

Figure 2.3 (a) shows the FTIR spectra of neat graphite, CA-graphite and AG-graphite samples. No wide peak ranging from 3400 to 3600 cm^{-1}, corresponding to the hydroxyl group, was shown on the FTIR curve of neat graphite. It suggested the heat treatment removed most physically-absorbed water on the surface of graphite nanodisks. The small peak at 1573 cm^{-1} was attributed to stretching vibration of carbonyl groups (C=O). It suggested that some surface carbon atom may be oxidized in the heat treatment procedure. Compared to neat graphite, a new wide peak appeared on FTIR curve of CA-graphite centering 3427 cm^{-1}, showing some hydroxyl groups were generated. The small double peaks at 2850 and 2921 cm^{-1}, corresponding to the stretching vibration of methyl groups ($-CH_3$) or methylene groups ($-CH_2-$), were given by short alkane chain in citric acid coating. The weak peak around 1720 attributed to carboxylic groups form citric acid or esters formed from self-polymerization between citric acid. Therefore, the results confirmed that hydroxyl groups were created on the graphite surface through citric acid-heat treatment.

For AG-graphite, the double peaks at 2850 and 2920 cm^{-1}, attributed to the stretching vibration of methylene groups, become much larger and the peak around 1464 cm^{-1}, attributed to the bending vibration of –CH2- appears (Chercoles, San et al. 2009). The new peak appearing at 1119 cm^{-1} corresponds the asymmetric stretching of C-O-Si bond (Oh, Lee et al. 2005), which is generated by the covalent bonds between silane and the graphite surface. These results verified the long alkane chain was attached to the surface of graphite nanodisks via silanization.

Figure 2.3 (b) shows the FTIR spectra of neat and AG-SiC nanoparticles. The neat SiC has wide peak ranging from 3200 to 3600 cm^{-1}, verifying some hydroxyl groups on the surface of neat SiC. It was also reported by other researchers (Harris 1995, Schoell, Hoeb et al. 2008). The strong peak at 1082 cm^{-1} was attributed to Si-C bond. The AG-SiC has a new double-peak at 2850 and 2920 cm^{-1}, which attributed to the stretching vibration of methyl and methylene groups in silane. The sharp peak at 1072 cm^{-1} corresponds to the combination of Si-C bond and the symmetrical Si-O-Si stretching. These results verified the long alkane chain was attached to the surface of nanoparticles via silanization.

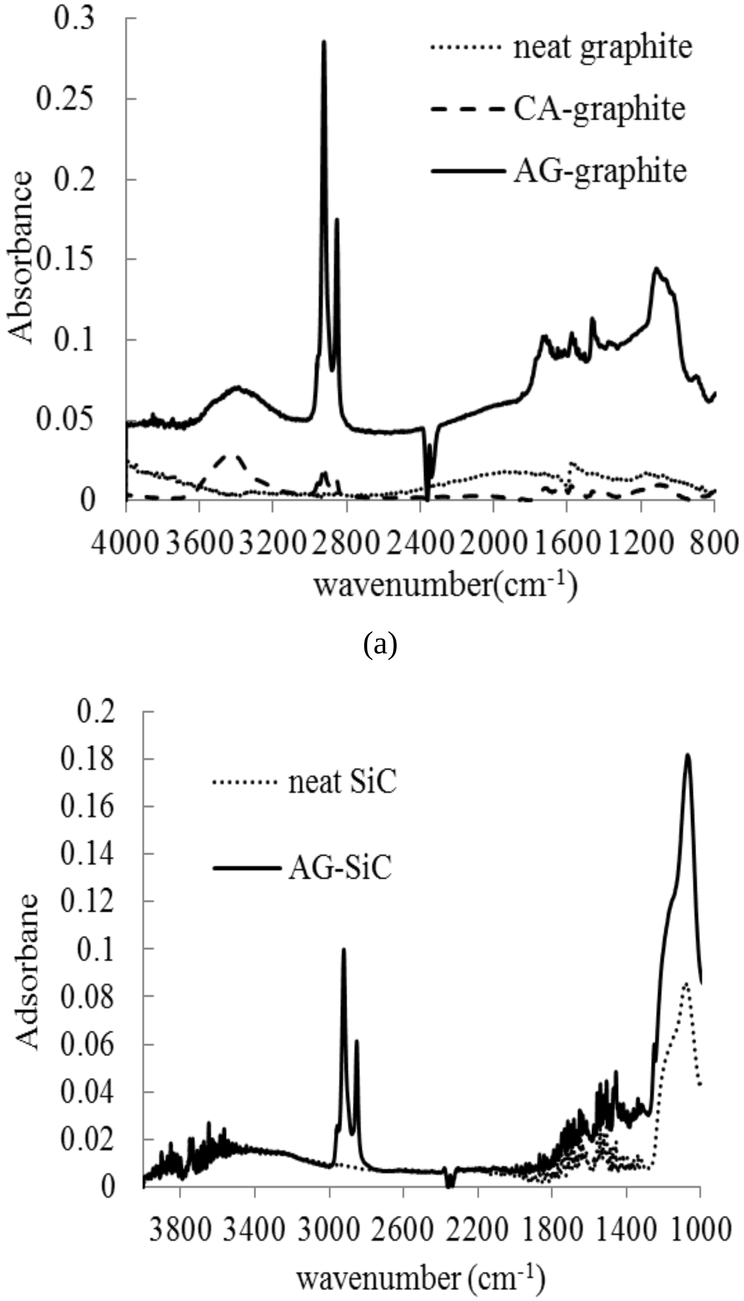

(a)

(b)

Figure 2.3 FTIR spectra of (a) neat graphite, CA-graphite and AG-graphite (b) neat SiC and AG-SiC nanoparticles

2.4.3 Surface groups and composition analysis by TGA

Thermogravimetric analysis (TGA) in the absence of oxygen can show a number of weight loss events, attributing different decoupling reactions. The physically-adsorbed water on the nanoparticles surface will typically desorb from room temperature to 110 °C. Therefore all samples were kept at 110°C for 30 minutes to complete the process. At higher temperature, the surface hydroxyl groups can undergo dehydration. Two hydroxyl groups release a water molecule and give a C-O-C or Si-O-Si structure. Our previous TG-MS result shows the dehydration of hydroxyls on graphite occurs over the temperature range, 110 °C < T < 320 °C(V. Kanniah 2012). Above this temperature, the decarboxylation reaction and decomposition of alkane chain happened since TG-MS result shows the formation of carbon dioxide and ethylene molecules. The dehydration of hydroxyls on SiC occurs at the temperature ranging from 110 °C to 350 °C, then complex reactions of surface carbon atoms occurs with the peak centered at 650°C (Lu, Xie et al. 2003, Gu, Zhang et al. 2009). So the weight loss occurring over these separate temperature regions can be used to estimate the amount of functional group on the nanoparticle surface. The estimates for both the hydroxyl surface density, (# OH/nm^2), and alkane chains surface density (# alkane chains/nm^2), was useful to evaluate the effect of surface modification.

The surface area per gram (S, nm^2/g) of nanoparticles has been estimated via Equation 2.1 and 2.2, based on the shape and dimension obtained from the SEM and TEM pictures.

$$S_{\text{graphite}} = \frac{surface}{mass} = \frac{2\pi \text{rh} + 2\pi r^2}{\pi r^2 h\rho} = \frac{2(h+r)}{rh\rho} \qquad (2.1)$$

where r is the graphite nanodisks' radius (1165 nm), h is the thickness of single graphite nanodisk (50 nm) , and ρ is the density of crystalline graphite (2.2g/cm^3).

$$S_{\text{SiC}} = \frac{surface}{mass} = \frac{4\pi r^2}{\frac{4}{3}\pi r^3 \rho} = \frac{3}{r\rho} \qquad (2.2)$$

where r is the SiC nanoparticles' radius (9 nm), and ρ is the density of crystalline SiC (3.22g/cm^3).

The number of hydroxyls per gram of nanoparticles, F (# groups/g), can be estimated from the weight loss over specific temperature ranges by Equation 2.3.

$$F_{\text{hydroxyls}} = \frac{2\left(\frac{W_{water}}{Mw_{water}}\right)N_A}{W_{final}} \qquad (2.3)$$

where, the factor "2" means two hydroxyls are lost for each molecule of water, W_{water} is the weight of water lost, and Mw_{water} is its molecular weight, NA is the Avogadro's number, and W_{final} is the weight of the sample at the end of the TGA decomposition experiment. It was used as weight of pure nanoparticles in the sample. Equation 2.4 was used to estimate the number of alkane chains per unit mass of neat nanoparticles.

$$F_{\text{alkane}} = \frac{\left(\frac{W_{alkane}}{Mw_{alkane}}\right)N_A}{W_{final}} \qquad (2.4)$$

Where, W_{alkane} is the weight loss of silane coating, and Mw_{alkane} is the molecular weight of alkane part in silane.

The surface densities of hydroxyl and alkane groups were estimated by computing the ratio of F_i and S_i.

Surface functional groups on graphite nanodisks

Figure 2.4 shows TGA curves of percent weight loss with temperature for neat graphite, CA-graphite and AG-graphite samples in nitrogen. Table 2.1 summarized weigh loss events with the various surface groups on the graphite samples.

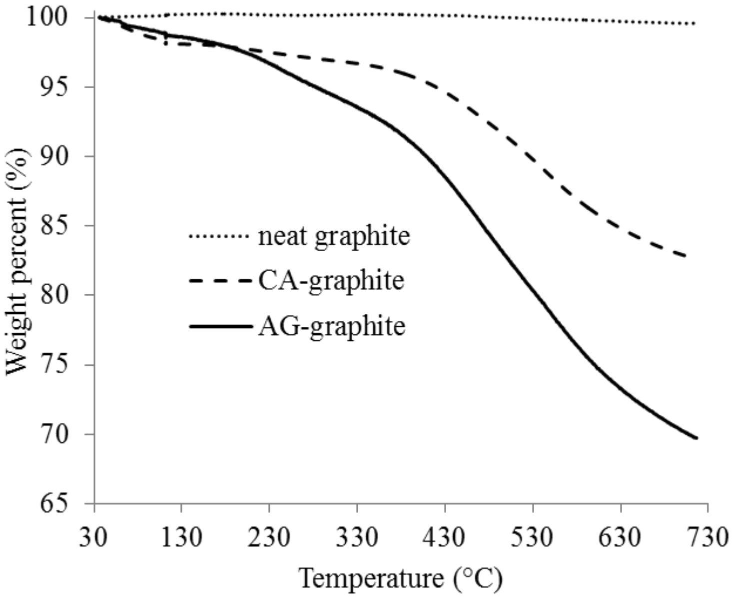

Figure 2.4 TGA curves of neat graphite, CA-graphite and AG-graphite samples

Table 2.1 Composition of weight loss events for graphite samples

Temp (°C)	Reaction	% Weight loss
a) neat graphite		
25 – 110	Desorption of water	~ 0
110 – 720	Decomposition of ketone groups	0.6
b) CA-graphite		
<110	Desorption of water	1.89
110 – 320	Dehydration	1.33
320 – 720	Decomposition of citrate coating	14.2
c) AG-graphite		
<110	Desorption of water	1.3
110 – 320	Dehydration and initial decomposition of alkane	4.8
340 – 720	Decomposition of citrate and alkane coatings	21.4

Neat graphite doesn’t have measurable weight loss below 110 °C. It suggested almost no physically-absorbed water on the surface. 0.6% weight loss was recorded from 110 to 720 °C. This weight loss was likely to be the dehydration and decomposition of aldehyde/ketone (Barton and Harrison 1975, Pellenbarg, Dementev et al. 2010), which has been verified by FTIR result.

In our previous TG study, the pure citric acid melts at ~153 ºC, decomposes from 175 ºC and finishes at 300 ºC. The initial decomposition products are aconitic acid and itaconic acid. The final products are carbon dioxide and ethylene (Barton and Harrison 1975, Barbooti and Al-Sammerrai 1986). As the CA-graphite was heated at 300 ºC for 30 mins and washed, the free citric acid should decomposes or be removed thoroughly. However, the CA-graphite shows several weight loss events, which are different from weight loss events of neat graphite. It seems very likely some functional groups on the graphite have condensed with hydroxyl and carboxylic groups in citric acid. In addition, some self-condensation reactions between hydroxyl groups and carboxylic groups between different citric acid molecules have occurred. Similar phenomena were observed in functionalization of other nanoparticles. The citric acid was reported to be irreversible sorbed onto anatase titania or ceria nanoparticles and water washing didn’t remove the material (Mudunkotuwa IA 2010).

The CA-graphite has 1.33% weight loss at the temperature ranging from 110°C to 320°C. It results from the dehydration of hydroxyl groups in citric acid coating. The surface density of hydroxyl groups on CA-graphite was estimated to be was 57/nm^2. The increase on hydroxyl groups was consistent with the FTIR scans discussed previously. Based on an estimated size (8.4 Å^2) of hydroxyl groups, closest packed hydroxyls on a flat crystalline surface would have a surface density of 11-12 OH/nm^2 (Carmo 2001). The 57/nm^2 suggested that the hydroxyls were arranged in a multilayer structure, which may formed in the self-condensation between different citric acid. The major weight loss

(14.2%) for CA-graphite occurred between 320°C to 720°C. The main reaction in this temperature range was decomposition of citric coating. Subtracting the weight loss of neat graphite, the weight of citric acid coating per gram of nanoparticles was 0.181 g. We assume the density of the citric acid coating is similar with that of the pure material (1.665g/cm^3); the estimated citric acid coating thickness is 5.7 nm. The hydrodynamic diameter of citric acid molecule has been estimated as 0.72 nm (van Drunen, Finsy et al. 1993). Based on these dimensions for the molecule, the number density of close packed citric acid molecules was 2.5/nm^2 and the estimated thickness represents about 8 layers of citric acid molecules on the nanoparticles. So the theoretical hydroxyl density without condensation should be $2.5\times8\times4=80/\text{nm}^2$, the 57/nm^2 we measured was 71% of theoretical hydroxyl density.

AG-graphite has both citric acid coating and silane coating. At the temperature range $110°\text{C} < T < 320°\text{C}$, the total weight loss is 4.8%. It combined the dehydration of unreacted hydroxyl groups and initial decomposition of alkane chain. The main weight loss, 24.1% was observed above 320 °C, combine the decomposition of both citric acid coating and alkane chains. We subtracted the overall weight loss of CA-graphite (15.5%) ranging from 110°C to 720°C from the overall weight loss (28.9%), obtained the weight for alkane chain per gram of graphite is 0.225g. According to Equation 2b, the surface density of alkane-chain on the surface was estimated to be 28/nm^2. Therefore, the reacted percentage of hydroxyl groups was 28/57 =49%. Assuming that the citric acid layer and the silane layer do not intermingle (or that each component contributes to the layer density based on its liquid or solid density), the silane coating thickness was estimated to be additional 9.8 nm to the citric acid coating and total thickness is 15.5 nm), but our SEM does not have enough resolution to show the thickness.

Surface groups on SiC

Figure 2.5 shows TGA curves of neat SiC and AG-SiC nanoparticles in nitrogen. The weight loss events with the various surface groups on the neat and AG-SiC samples were summarized in Table 2.2.

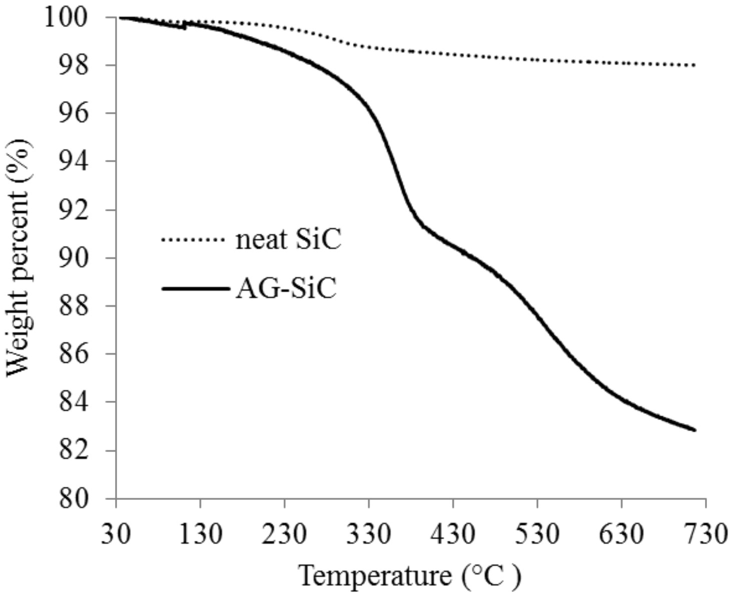

Figure 2.5 TGA curves of neat SiC and AG-SiC samples

Table 2.2 Composition of weight loss events for SiC samples

Temp (°C)	**Reaction**	**% Weight loss**
a) neat SiC		
<110	Desorption of water	0.21
110 – 350	Dehydration	1.15
350 – 720		0.65
b) AG-SiC		
<110	Desorption of water	0.34
110 – 350	Dehydration and initial decomposition of alkane	8.8
350 – 720	Decomposition of alkane	8.1

The water associated with the neat silicon carbide surface was 0.17%. This water was likely associated with surface hydroxyl groups on the silicon carbide. The surface hydroxyl groups (1.15%) dehydrated over the temperature range, 110°C < T < 350°C, the estimated hydroxyl density on the surface of neat SiC is 7.6/nm^2 (Table 2.2). Additional material (0.65%) was lost from the surface ranging from 350°C to 720°C.

The overall weight loss of AG-SiC at the temperature ranging from 110 °C to 720°C is 16.9%. Subtracting the weight loss of neat SiC at this temperature range, the weight of alkane coating per gram of SiC nanoparticles was 0.185 g. The Si part in the n-octadecyldimethyl-chlorosilane was assumed to be left on the surface and other moiety (MW=253.6) removes from the surface. The surface density of alkane-chain on the surface was estimated to be 4.2/nm^2. So 4.2/7.6=55% of the hydroxyl groups reacted with chloro groups in the coupling process. The silane coating thickness was estimated to be 1.3 nm based on the liquid density of silane. The hydrodynamic diameter of silane molecule has been estimated as 1.12 nm, the estimated thickness represents about monolayer of alkane on the SiC nanoparticles.

2.4.4 Thermal conductivities of graphite and SiC dispersion

<u>Combined Hamilton-Crosser and Davis Model</u>

Hamilton-Crosser (1962) and Davis (1986) models have been applied on fitting the thermal conductivities of suspensions.

$$\text{Hamilton-Crosser model: } \frac{k_e-k_f}{k_f}=\frac{n(\alpha-1)\Phi}{\alpha+(n-1)+(1-\alpha)\Phi}$$

$$\text{Davis model: } \frac{k_e-k_f}{k_f}=\frac{3(\alpha-1)[\Phi+f(\alpha)\Phi^2]}{\alpha+2-(\alpha-1)\Phi} \qquad (2.4)$$

Where k_e is the effective thermal conductivity of the mixture, k_f is the thermal conductivity of base fluid, $\frac{k_e-k_f}{k_f}$ was defined as the enhancement percentage, α is the ratio of thermal conductivity of particles and base fluid, Φ is the volume fraction of particles, *f(α)* was a complicated function to represent strong interaction between particles, n is the particle shape factor, it is calculated by following formula:

$$n = 3\psi^{-1} \tag{2.5}$$

where ψ is the sphericity, defined as the ratio of the surface area of a sphere, with a volume equal to that of the particle, to the surface area of the particle. The ψ is always larger than 1 since the spherical particle has lowest surface area in all particles with the same volume. Therefore, the n is always less than 3.

Both of these two models has limit on fitting the enhancement on thermal conductivity of dispersion with nanoparticles. Hamilton-Crosser model doesn't consider the strong interactions between nanoparticles so sometimes underestimate the enhancement but Davis model use the "f (α) Φ^2" item to represent these interactions; Davis model didn't consider the shape factor contained in Hamilton-Crosser model. Therefore, a combined model (Equation 2.6) was used by us for containing the influence of interactions between nanoparticle and shape factor.

Combined model: $$\frac{k_e - k_f}{k_f} = \frac{n(\alpha-1)}{\alpha+(n-1)-(\alpha-1)\Phi}\left[\Phi + f(\alpha)\Phi^2\right] \tag{2.6}$$

For spherical particle, n=3, it transforms to be Davis model. If the interaction between nanoparticles is weak, the "f (α) Φ^2" item can be neglected therefore it transforms to be Hamilton-Crosser model.

Graphite dispersions

The thermal conductivity enhancement percentage of dispersion with different volume fraction of neat and AG-graphite were shown in Figure 2.6.

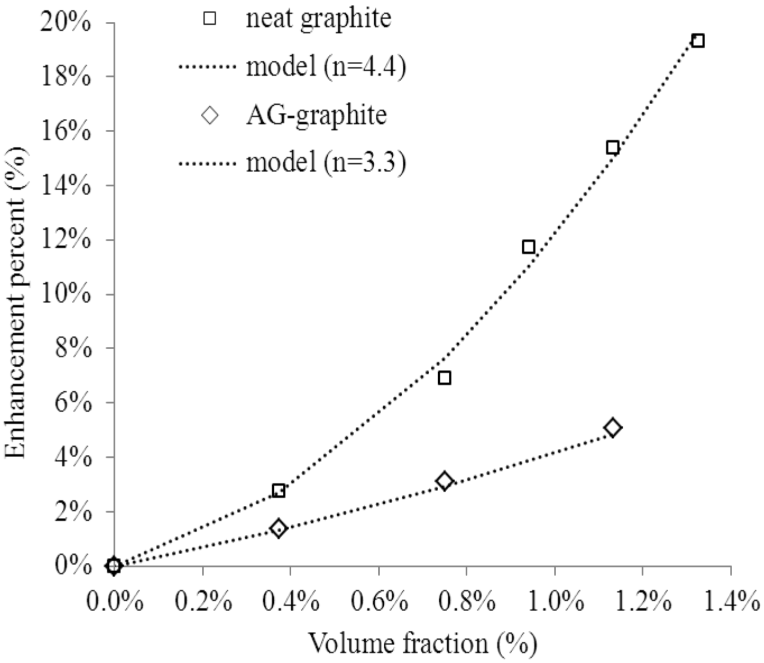

Figure 2.6 Thermal conductivity enhancements of dispersions with different volume fractions of neat and AG-graphite nanodisks

The enhancement on *k* of neat graphite dispersion is 19% when the volume fraction is 1.4%. The relation between enhancement and volume fraction is non-linear. After surface modification, the enhancement become milder, 5% was recorded when the volume fraction of AG-graphite is 1.2 %. The relation between enhancement and volume fraction is linear till 1.2 vol%. The results show the surface modification decrease the enhancement on thermal conductivities of graphite dispersions. The enhancement percentage of dispersion with different volume fraction of neat and AG-graphite were fitted by this model very well. The shape factors obtained by the model are 4.4 and 3.3 for neat and AG-graphite respectively. However, the primary particle of neat and AG-graphite are nanodisks with aspect ratio about 0.02. The calculated shape factor should be 15.5. It is much higher than the value obtained from model.

The lower enhancements on thermal conductivity for AG-graphite dispersion and the difference on shape factors may result from the different morphology of agglomerates in graphite dispersions. The morphology of agglomerates in 0.75 vol% neat and AG-graphite were shown in Figure 2.7.

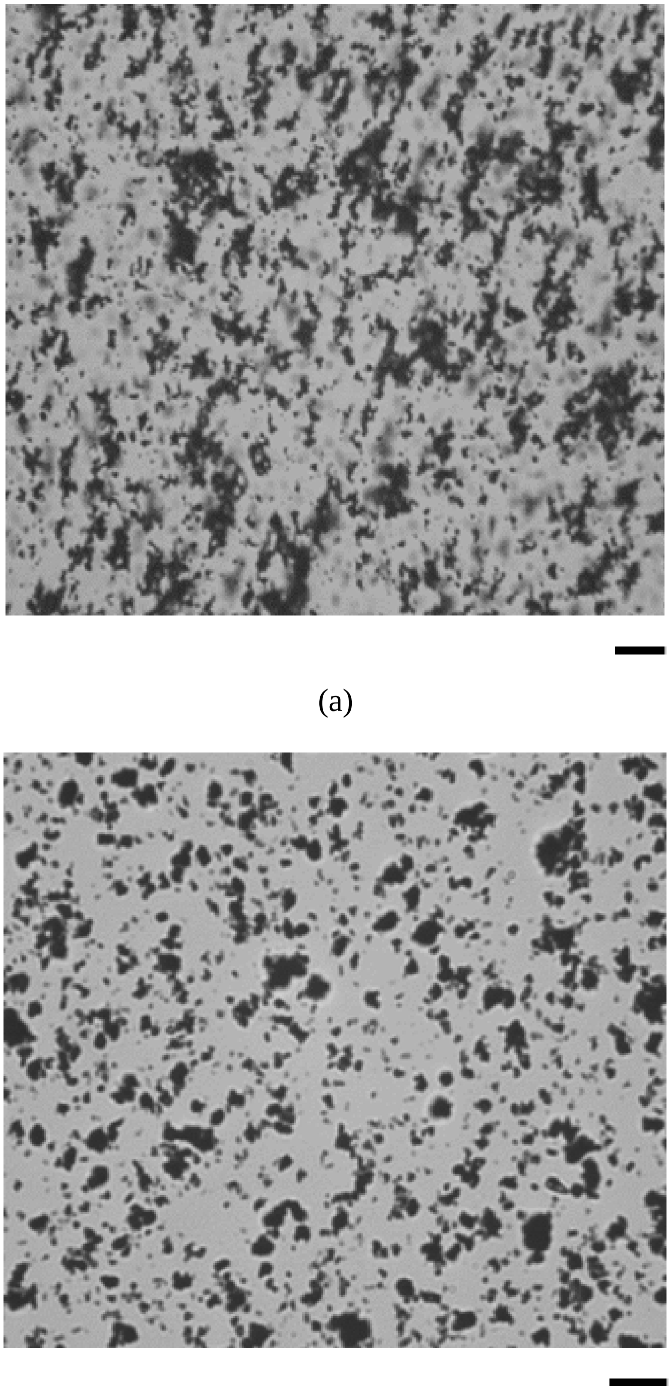

(a)

(b)

Figure 2.7 Morphology of graphite dispersions: (a) 0.75 vol% of neat graphite, (b) 0.75 vol% of AG-graphite. (Scale bar=5 µm)

The agglomerates in neat graphite dispersion like long prolate spheroid and most of them contact each other. 30 agglomerates were counted to get the longest and shortest length is 10.5 and 2.3 µm. The aspect ratio of agglomerates is 4.6. The agglomerates in AG-graphite dispersion like short prolate spheroid and separate each other. 30 agglomerates were counted to get the average longest and shortest length is 4.5 and 2.3 µm. The average aspect ratio of agglomerates is 1.96. Therefore, the surface modification offset the tendency to form agglomerates.

The shape factor of agglomerates can be calculated from the definition and formula about prolate spheroid shape.

Surface of prolate spheroid: $S = 2\pi a^2 \left(1 + \frac{b}{ae} sin^{-1} e\right)$, $e = \sqrt{1 - \left(\frac{a}{b}\right)^2}$

Volume of prolate spheroid: $V = \frac{4}{3}\pi a^2 b$ (2.7)

where a, b are half major and minor axis of prolate spheroid respectively.

The shape factors calculated from size of agglomerates are 4 for neat graphite and 3.2 for AG-graphite). Both of them are close to the shape factors (4.4 for neat and 3.3 for AG-graphite) obtained by the combined model. It may suggest the shape factor in thermal conductivity enhancement relates to the aspect ratio of agglomerates more than the aspect ratio of primary nanoparticles.

SiC dispersions

The enhancement percentage of dispersion with different volume fraction of neat and AG-SiC were shown in Figure 2.8.

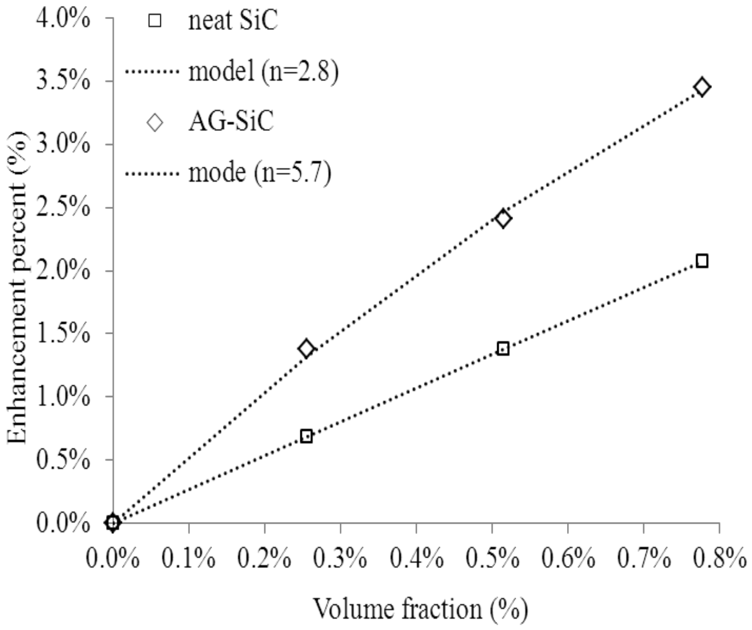

Figure 2.8 Thermal conductivity enhancement of dispersions with different volume fractions of neat and AG-SiC nanoparticles

The enhancement on *k* of neat SiC dispersion is 2% when the volume fraction is up to 0.8%. The relation between enhancement and volume fraction is linear. After surface modification, the enhancement become larger, 3.5% was recorded when the volume fraction is 0.8%. The relation between enhancement and volume fraction is non-linear. The results show the surface modification increase the enhancement of thermal conductivities of SiC dispersions. The enhancement percentage of dispersion with different volume fraction of neat and AG-SiC were fitted by this model very well. The shape factors are 2.8 and 5.7 for neat and AG-SiC respectively. The morphology of agglomerates in 0.5 vol% neat and AG-SiC dispersion were shown in Figure 2.9.

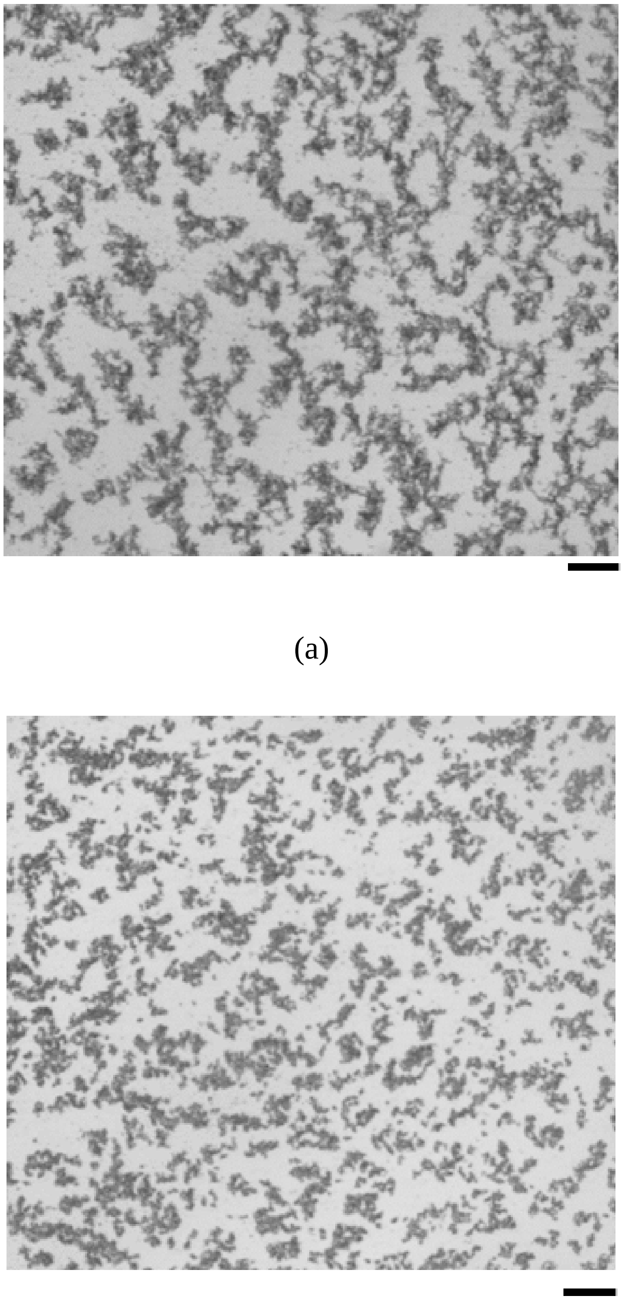

(a)

(b)

Figure 2.9 Morphology of SiC dispersions: (a) 0.5 vol% of neat SiC, (b) 0.5 vol% of AG-SiC. (Scale bar=100 μm)

The agglomerates in neat SiC dispersion have a star-shape and connect each other. The average diameter of the star-shaped agglomerates is over 250 µm. The aspect ratio is difficult to define. The agglomerates in AG-graphite dispersion are combination of long and short prolate spheroid. Some connect while others separate each other. 30 agglomerates were counted to get the average longest and shortest length is 172 and 18 µm. The average aspect ratio of agglomerates is 9.6. Therefore, the surface modification offset the tendency to form agglomerates. The calculated shape factor was 5.1. It is close to the shape factors (5.7 for AG-SiC) obtained by the combined model. It also suggests the shape factor in thermal conductivity enhancement relates to the aspect ratio of agglomerates more than the aspect ratio of primary nanoparticles.

In both graphite and SiC dispersions, the surface modification decreases the size of agglomerates. However, it decreases the enhancement of thermal conductivity in graphite dispersion and increases that in SiC dispersions. The phenomena may result from competitive effect of Brownian motion and nanocluster mechanisms. For Brownian motion mechanism, the thermal conductivity increases with decrease of agglomerate size because it can lead stronger local convection. For nanocluster mechanism, the thermal conductivity increases with increase of agglomerate size since some local three dimensional networks can form. As the surface modification offset the size of agglomerates, It was helpful to Brownian motions of agglomerates while prevent the formation of local three-dimensional networks. It seems that the Brownian motion predominates in graphite dispersion with agglomerate size less than 10 um, so the enhancement on k decreases in the agglomerates size range in graphite dispersion. When the agglomerates size is in the range of SiC dispersion (20-200 nm), the nanocluster effect predominates so the enhancement on k increases with decrease of agglomerate size.

2.4.5 Rheological properties of graphite and SiC nanodispersions

The viscosity and rheological behavior of dispersion connect closely with agglomerates. For exploring the influence of agglomerates, the viscosity at zero shear rates η_0 need to be measured. It was difficult to measure since there was always some fluctuation on data at very low shear rate. However, the Cross model has been used widely to estimate the η_0 from the viscosity at some shear rate (η) and very high shear rate η_∞.

$$\text{Cross Model} \qquad \frac{\eta-\eta_\infty}{\eta_0-\eta_\infty} = \frac{1}{1+b\gamma^n} \qquad (2.11)$$

Where η is the viscosity at some shear rate, η_∞ is the viscosity at very high shear rate, *b* and *n* are two fitting parameters.

Cross model can fit the rheological behavior of graphite and SiC dispersions satisfactory. The obtained η_0 from dispersions with different volume fraction was fitted by Krieger-Dougherty model.

$$\frac{\eta_0}{\eta_f} = \left(1 - \frac{\Phi}{\Phi_m}\right)^{-[\eta]\Phi_m} \qquad (2.12)$$

Where η_0 is the viscosity of dispersion at zero shear rates, η_f is the viscosity of base fluid, Φ is the volume loading of nanoparticles, $[\eta]$ is the intrinsic viscosity and Φm is the maximum packing fraction.

<u>Graphite dispersion</u>

Figure 2.10 shows typical rheological behavior of neat and AG-graphite dispersion at 25 °C. 1 wt% neat graphite nanodispersion exhibited nearly Newtonian behavior at the shear rate range. However, the 3 wt% neat graphite nanodispersion exhibited obvious shear-thinning behavior. The viscosity of 3 wt% neat graphite nanodispersion at 0.1 s^{-1} is 0.38 Pa·s, eight times of viscosity of dispersion with 1 wt% neat graphite. The viscosities of these two dispersions at high shear rate are very close. It is likely that the shear thinning

behavior results from the deformation and/or disruption of graphite agglomerates. More agglomerates formed when the volume fraction increases so the dispersion undergoes the transition from nearly Newtonian to shear-thinning.

The 1 wt% AG-graphite nanodispersion exhibited nearly Newtonian behavior. The 3 wt% AG-graphite nanodispersion exhibited mild shear-thinning behavior. The viscosity of 3 wt% neat graphite nanodispersion at 0.1 s^{-1} is 0.1 Pa·s, two times of viscosity of dispersion with 1 wt% AG-graphite. The viscosities of these two dispersions at high shear rate are very close. Both of them have lower viscosities and more Newtonian behavior than the dispersion with the same volume fraction of neat graphite. It results from the surface medication offset the agglomeration tendency.

Figure 2.11 shows the viscosity ratio with different volume fractions of graphite nanodisks. The Krieger-Dougherty model can fit viscosity-volume fraction very well. The maximum pack fractions obtained for neat and AG-graphite dispersion were 1.48 vol% and 1.65 vol% respectively. The percolation limit predicted from the geometrical relation was 2.2 vol% based on the aspect ratio of graphite nanodisks and from 18% to 20% based on the aspect ratio of agglomerates (Garboczi, Snyder et al. 1995). It suggests the maximum packing fraction in rheological behavior relates to the aspect ratio of primary nanodisks more than the aspect ratio of agglomerates. The intrinsic viscosities represented the contribution of nanoparticles to solution’s viscosity. The intrinsic viscosities of neat and AG-graphite dispersions were 94 and 18 respectively. It means the surface modification decrease the contribution of nanoparticle to solution’s viscosity due to offset the formation of agglomerates

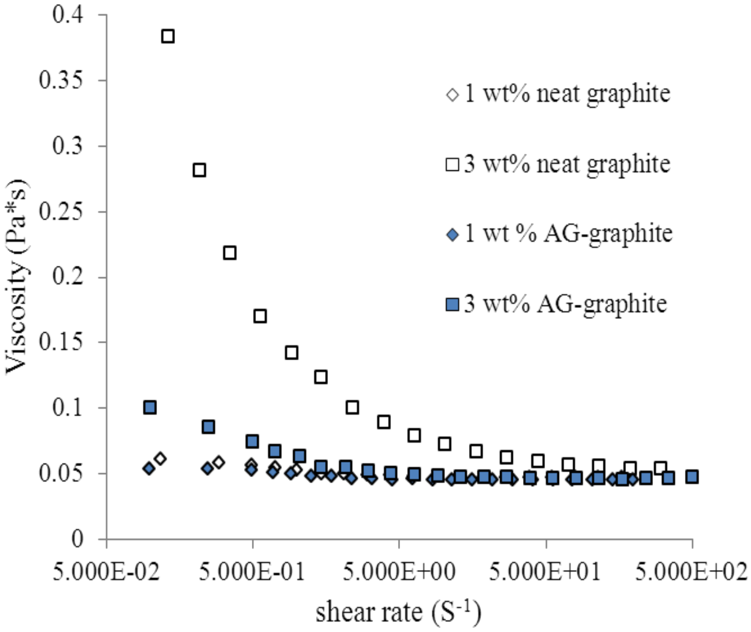

Figure 2.10 Typical rheological behavior of neat and AG-graphite dispersions

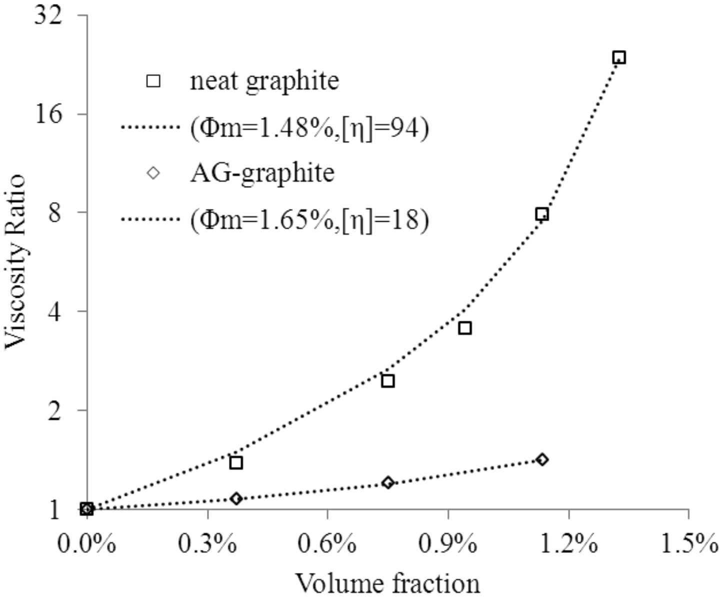

Figure 2.11 Viscosity ratio of dispersions with different volume fractions of neat and AG-graphite nanodisks

SiC dispersion

Figure 2.12 shows typical rheological behavior of neat and AG-SiC dispersion at 25 °C and the viscosity ratio with different volume fractions of SiC nanoparticles. The 1 wt % neat SiC dispersion exhibited a little bit shear-thinning behavior at the shear rate range. The 3 wt% neat SiC dispersion exhibited obvious shear-thinning behavior. The viscosity of 3 wt% neat SiC dispersion at 0.7 s^{-1} is 1.27 Pa·s, nearly ten times of 1 wt% neat SiC dispersion. The viscosities of these two dispersions at high shear rate are very close. It is likely that the shear thinning behavior results from the deformation and/or disruption of graphite agglomerates. More agglomerates formed when the volume fraction increases so the dispersion became more shear-thinning.

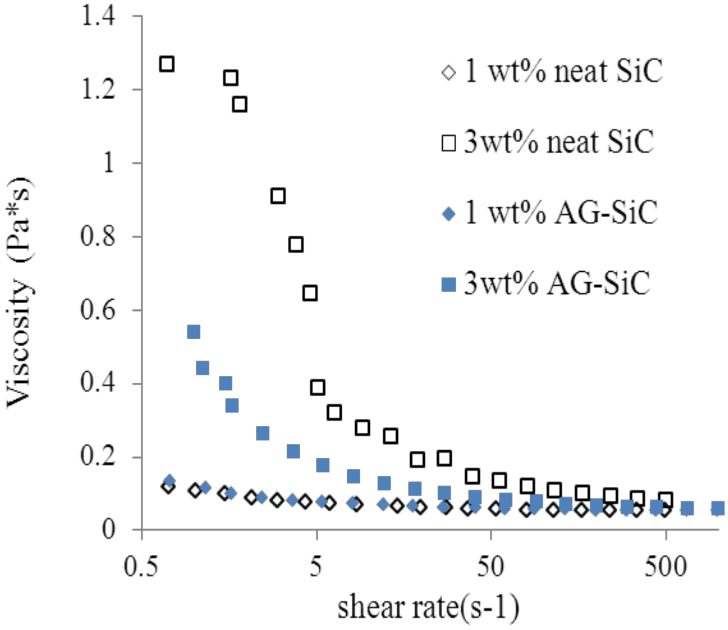

Figure 2.12 Typical rheological behavior of neat and AG-SiC dispersion

The 1 wt% AG-SiC dispersion exhibited a little bit shear-thinning behavior at the shear rate range. The 3 wt% AG-graphite dispersion also exhibited shear-thinning behavior. The viscosity of 3 wt% neat SiC dispersion at 1 s^{-1} is 0.5 Pa·s, five times of viscosity of dispersion with 1 wt% AG-SiC. The viscosities of these two dispersions at high shear rate are very close. The 3 wt % AG-SiC dispersion has lower viscosities and relatively less non-Newtonian behavior than the dispersion with the same volume fraction of neat SiC. It results from the surface modification offset the agglomeration tendency. The effort to use Krieger-Dougherty model to fit viscosity-volume fraction data doesn't give convergent sequences. More points were needed to modify the fitting procedure.

2.5 Conclusion

A simpler and environment-friendly method to modify surfaces of graphite nanodisks and silicon carbide nanoparticles was developed. The citric acid can generate hydroxyl groups and silanization can attach alkane chain on inert surfaces of graphite and SiC. The original and modified surface was evaluated via thermo-gravimetric analysis. The surface modification decrease formation of agglomerates in their dispersion. The dispersion of complex graphite has lower thermal conductivity than those of neat graphite. However, the dispersion of complex SiC has higher thermal conductivity than those of neat SiC dispersion. One combined model was built to fit non-linear enhancement on thermal conductivity with volume fraction of nanoparticles. It suggests the enhancement on thermal conductivity relates to shape factor of agglomerates strongly. The relation between agglomerates size and enhancement on thermal conductivity suggest the competitive effect of Brownian motion and nanocluster mechanisms. The rheological behavior of these dispersions with surface-modified nanoparticles became more Newtonian, more practical for practical application. The research supplied more understanding to influence of surface modification on the thermal and rheological properties of dispersions with nanoparticles.

Chapter 3: Nanoparticle segregation in ultrathin films: surface chemistry effects

3.1 Highlights

- Silanization method was applied to change surface hydrophilic/hydrophobic properties of silica and titania nanoparticle.
- TGA was used to evaluate original surface and surface modification effect.
- Formation of bi-layer structure via self-assembly segregation of surface-modified nanoparticles in monomer matrix.

3.2 Introduction

Transparent ultrathin nanocomposite films can be used for a wide variety of applications, including reinforced anti-reflection optical filters (Druffel, Geng et al. 2006, Mosher, Wu et al. 2006) and multi-layer stacks designed as high-reflection coatings (Glocker 1995, Kats, Blanchard et al. 2013). The high-reflectance coatings (mirrors) comprise multi-layer structure with different effective refractive indices. Precise control of the optical properties of each layer will require control of: the composition and crystallinity of the nanoparticle additives, the polymer continuous phase composition, the layer thickness, the interlayer adhesion, and the manufacturing process. The first two elements, nanoparticle and polymer composition, establish the effective refractive index (RI) of each layer. Some low cost choices of nanoparticles range from silica (low, 1.54) to zinc oxide (medium, 2.0) and titania (high, 2.6). The RI difference between layer and layer refractive indexes, and the thickness of each layer influence the phase shift of light (H.A.Macleod 2001). With precise control of refractive indexes and coating thickness, the constructive interference will happen and increase the reflectance to at the design specific wavelength such as infrared (Druffel, Geng et al. 2006), visible (Zhang, Li et al. 2009), ultraviolet (Torchio, Gatto et al. 2002), even X-ray (Tripp, Fabreguette et al.

2005).

Practically, the multi-layers structure was usually achieved by "layer-by-layer" deposition processes such as vapor deposition (Martinu and Poitras 2000) or sol-gel dip coating (Brinley, Seal et al. 2006). However, alternating polymer matrix compositions can lead to problems with interfacial adhesion. Using one polymer matrix but adding nanoparticles with higher or lower refractive index will control the layer refractive index and retain good interlayer adhesion. Therefore layers with refractive index gradients represent a new type of designs. This study explored the possibility of producing refractive index gradients by inducing gradients in the nanoparticle additives. The gradients might be induced by altering the nanoparticle surface chemistries in ways that would make the nanoparticles preferentially migrate to the liquid/solid or the air/liquid interface of the ultrathin film.

Figure 3.1 is a conceptual sketch of self-assembly segregation of nanoparticles, showing separation of two metal oxide nanoparticles with different surface modification during the spin coating of an ultrathin nanoparticle/monomer mixture.

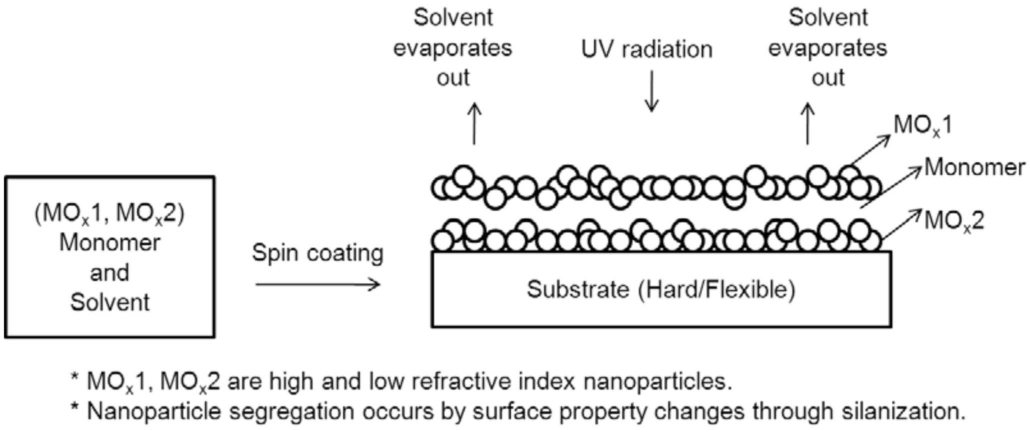

* MO$_x$1, MO$_x$2 are high and low refractive index nanoparticles.
* Nanoparticle segregation occurs by surface property changes through silanization.

Figure 3.1 Conceptual sketch of self-assembly segregation of nanoparticles

There are always some hydroxyl groups on metal oxide surfaces, which results in relative hydrophilic surface of metal oxide nanoparticles. The hydroxyl group can react with active silanes, which has leaving groups like methoxy, ethoxy or chloro. The result of silanization reaction is attaching more hydrophilic (amino or sulfuric chains), hydrophobic (alkane, aromatic), or superhydrophobic (fluoro-carbon chains) on surface of nanoparticles (Beck, Hartl et al. 1999, Shimada, Aoki et al. 2003, Raghuraman and Dhamodharan 2004, Garcia-Gonzalez, Fraile et al. 2009). The nanoparticle has opposite hydrophilic/hydrophobic properties to monomer is easy to form agglomerates, settle down and form bottom layer, while the nanoparticle with similar properties has tendency to keep in monomer matrix. So nanoparticles can achieve segregation due to their different compatibility with the monomer.

For verify the segregation in single deposition process and clarify the influence of the surface coverage of initial functional groups and attached groups from surface modification, our study involves 1) Constructing hydrophobic chains on initially hydrophilic silica and titania nanoparticles' surfaces. 2) Analysis and quantification of the surface modification by the TGA quantification method, which has been used to characterized both graphite nanodisks and SiC nanoparticles. 3) Analyze the segregation structure formed by Energy-dispersive X-ray spectroscopy (EDX).

3.3 Experiments

3.3.1 Preparation of neat silica and titania nanoparticles.

Commercial dispersion of colloidal silica in isopropyl alcohol (Nissan chemicals, IPA-ST) was used. The pH value of the dispersion was 2 so that some acid may act as stabilizer. The acid needed to be removed in order to control surface functionalization reactions. 0.5 ml of 25 mM sodium hydroxide solution was added into 10 ml of silica dispersion. Silica nanoparticles settled from the dispersion and the acid stabilizer forms sodium salts, followed by water washing, and recovery of the silica via ultracentrifugation. The silica nanoparticles were then washed by water three times and ethanol one time. The pH of the final supernatant was around 6.5, suggesting that both acid and base were removed. The recovered silica powder was dried at 90 ^{o}C overnight and the final dry sample was named "neat SiO_2". Commercial Titania powder (Alfa Aesar, Titanium(IV) oxide, anatase, 99.9%) was used. They were washed by water three times and ethanol one time. The recovered powder from ultracentrifuge was dried at 90 ^{o}C overnight. The dried sample was named "neat TiO_2".

3.3.2. Surface modification

For achieving controlled silanization and avoiding excess silane leading to self-condensation, we calculate the surface density (#/nm^2) of hydroxyl groups on silica and titania nanoparticles from via TGA. The detailed calculation method is described in the following section. Scheme 3.1 shows the surface modification procedure for silica and titania nanoparticles.

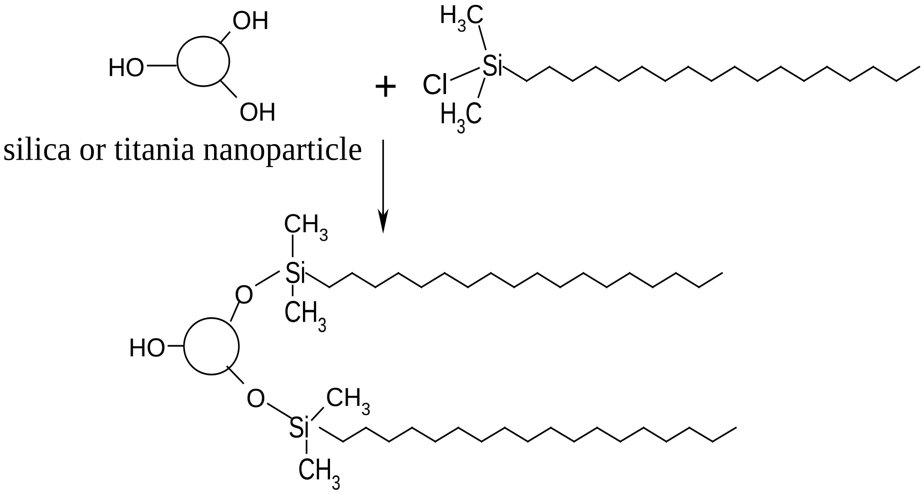

Scheme 3.1 Surface modification for silica and titania nanoparticles

200 mg of neat silica nanoparticles was dispersed in 15 ml toluene under the help of ultrasonication. 0.66 gram of n-octadecyldimethyl-chlorosilane (Gelest Company,

$C_{20}H_{43}ClSi$, MW=347.10) was dissolved in toluene to form a 5 wt% solution. The surface density of hydroxyl group was used to calculate the amount of silane needed to perform the coupling reaction; the molar ratio of hydroxyls on silica to chloro group was set at 1:5. The silane solution was added into the silica dispersion and the mixture was refluxed at 110 ^{o}C for 12 hours. The product was washed with toluene twice and ethanol twice to remove any excess silane and then air-dried at 90 ^{o}C. The dry sample was then named "AG-SiO_2" (alkane-grafted silica).

200 mg neat titania was dispersed in 50 ml toluene under the help of ultrasonication. 0.84 gram of n-octadecyldimethyl-chlorosilane (Gelest Company, $C_{20}H_{43}ClSi$, MW=347.10) was dissolved in toluene to form a 5 wt% solution. The surface density of hydroxyl group was used to calculate the amount of silane needed to perform the coupling reaction; the molar ratio of hydroxyls on titania to chloro group was set at 1:5. The silane solution was mixed with the titania dispersion. This ratio between titania and silane can make the molar ratio of hydroxyls to methoxy be 1:1. The mixture was kept refluxing at 110 C for 12 hours. Then it was washed and dried the same as on silica. The dry sample was then named "AG-TiO_2" (alkane-grafted titania).

3.3.3. Characterization of surface modification

The morphology and particle size distributions of the neat silica and titania were observed by TEM (Hitachi 2010F, University of Kentucky). Fourier Transfer Infrared Spectroscopy (Nicolet™ iS™50 FT-IR Spectrometer, University of Kentucky) was used to detect the functional groups on nanoparticles' surface. Diamond Attenuated total reflectance (ATR) measure unit was used. All the samples were heated in vacuum oven at 120 °C for one hour to remove the water from them. Tiny amount of nanoparticles were put on the plate and screw was tight to press samples to pellets. The pellets were scanned over the wavelength range, 400 cm^{-1} to 4000 cm^{-1}, in a dry air environment.

Quantitation of surface groups was done by thermo-gravimetric analyzer (TGA 7, Perkin Elmer Corporation). The analyzer can record the weight loss from degradation and decomposition with temperature. In a nitrogen environment, all samples were heated from room temperature to 100 °C at rate of 10°C /min, kept at 100 °C for 30 mins to remove physically-adsorbed water and then heated from 100 °C to over 700 °C at rate of 10°C /min. The degradation of all surface groups at such high temperature appeared to be complete.

3.3.4 Ultrathin film spin coating

An acrylate monomer (SR 415, Sartomer USA, LLC) were used to prepare ultrathin nanocomposite films. Their chemical structures are shown in Figure 3.2.

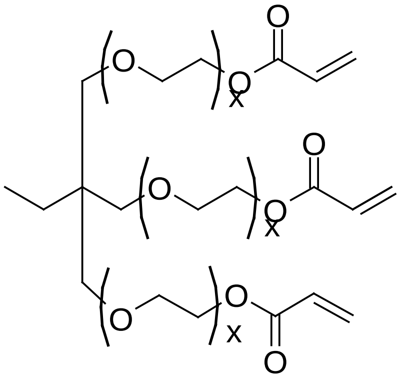

Figure 3.2 Chemical structure of SR 415, hydrophilic monomer

The SR 415 monomer has propane triacrylate structure. Meanwhile it has ethoxylated groups in each ‘leg’ of the chains (x is around 20). These ethoxylated groups enhance the water solubility of the monomer, making it relatively hydrophilic (the surface tension = 41.8 dynes/cm). It also has three carbon-carbon double bonds so they are easily and rapidly UV-curable. Physical properties of the nanoparticles and monomers are listed in Table 3.1.

Table 3.1 Material properties data sheet

Materials used	**Refractive Index**	**Density (g/cm^3)**	**Molar mass (g/mol)**	**Surface tension (Dynes/cm)**
neat SiO_2	1.49	2.63	60.1	-
neat TiO_2	2.49	3.9	79.9	-
SR 415	1.47	1.12	1176	41.8

The neat and alkane-grafted nanoparticles were mixed with SR 415 to form two dispersions. 1-Hydroxy cyclohexyl phenyl ketone (Ciba Irgacure 184) was used as the photoinitiator. The used sample weight and expected final composition were described in Table 3.2.

Table 3.2 Composition of dispersion for bi-layer structure

ID	Description	Final Composition (vol %)
bilayer-1	30 mg AG-SiO_2, 30 mg neat TiO_2, 300 mg SR 415, 2.64 g 1-methoxy 2-propanol	0.36% AG-SiO_2, 0.24 % neat TiO_2 8.5% monomer, 91% solvent
bilayer-2	30 mg neat SiO_2, 30 mg AG-TiO_2 300 mg SR 415, 2.64 g 1-methoxy 2-propanol	0.36% neat SiO_2, 0.24% AG-TiO_2 8.5% Monomer, 91% solvent

The particle size of silica and titania in their dispersions were measured by dynamic light scattering method (90 Plus, particle size analyzer, Brookhaven Instrument Corporation). 3 drops of the mixtures were spin-coated at 1000 rpm kept 3 mins, and then a layer of film was formed on the polycarbonate substrate, 6 cm×6 cm cut from polycarbonate sheet (thickness is .020 inch, 2 ft x 4 ft, TAP Plastics). The remained solvent was removed by vacuum heating. After addition of photo initiator and cured by UV, the final sample was named “bilayer 1-2”

3.3.5. Characterization of nanoparticle segregation in ultrathin films

The coated polycarbonate thin plate was put in to epoxy resin. After the resin was cured, microtome cutting was used to slice very thin sections from the films on polycarbonate substrate. EDX (Energy-dispersive X-ray spectroscopy) was used to identify the elemental composition across the cross-sectional surface of the ultrathin film.

3.4 Results and Discussions

3.4.1 Morphology of neat SiO_2 and TiO_2 nanoparticles

Figure 3.3 shows the TEM picture and particle size distribution of neat SiO_2. Most of SiO_2 nanoparticles observed in the TEM picture were nearly spheroidal. Over 130 nanoparticles were counted to obtain the primary particle size distribution. The distribution was fit with lognormal distribution model. The mean diameter given by the lognormal model was 12.9 nm.

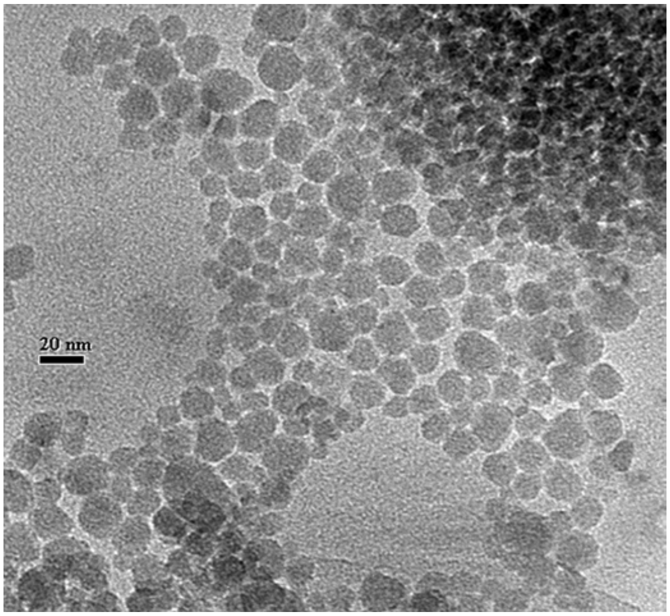

(a)

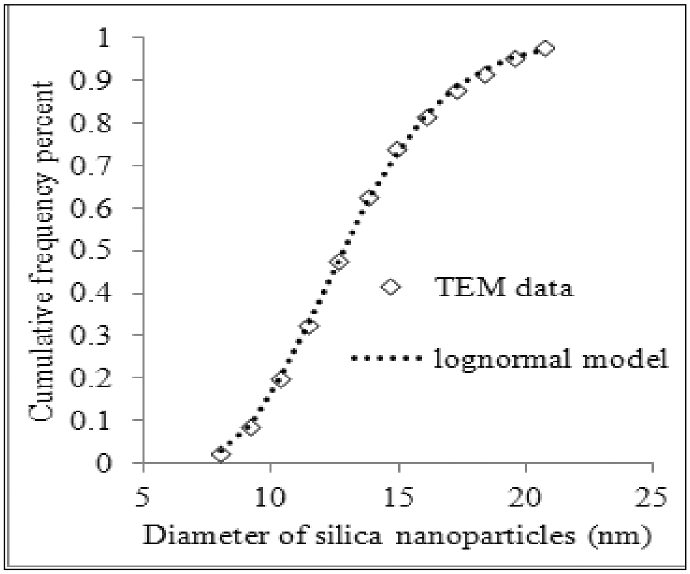

(b)

Figure 3.3 Morphology of neat silica nanoparticles: (a) TEM picture and (b) primary particle size data fitted by lognormal model.

Figure 3.4 shows the TEM picture of neat TiO_2 nanoparticles. The neat titania nanoparticles were spheroidal with an area-equivalent diameter of 27 nm.

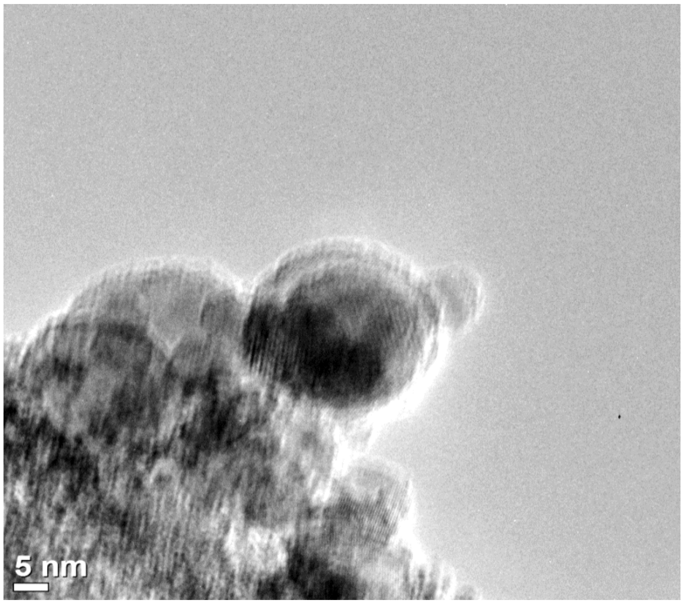

Figure 3.4 TEM picture of neat TiO_2 nanoparticles

3.4.2 FTIR characterization

Figure 3.5 (a) shows the FTIR results of neat and alkane-grafted SiO_2 nanoparticles. For neat silica nanoparticles, the broad peak from 3700 cm^{-1} to 3300 cm^{-1}, centering 3450 cm^{-1} shows there were some hydroxyl groups on surface. The peak at 1060 cm^{-1} represent the Si-O asymmetric stretching vibration (Calleja, Falcony et al. 1995). For AG-SiO_2 nanoparticles, there are new peaks at 2852 and 2930 cm^{-1}, representing the stretching vibration of methylene and methyl groups. The result shows some alkane chains have been attached on the surfaces. The new peak at 790 cm^{-1} attributed to the bending of Si-O bond. It attributed to the formation of Si-O-Si bond in surface modification.

Figure 3.5 (b) shows the FTIR results of neat and alkane-grafted TiO_2 nanoparticles. The neat TiO_2 nanoparticles have a large, broad peak (from 3700 cm^{-1} to 2600 cm^{-1}, centering at 3370 cm^{-1}), representing the hydroxyl groups (Maira, Coronado et al. 2001). For AG-TiO_2 nanoparticles, two new peaks (2850 and 2923 cm^{-1}) appear, representing the stretching vibration of methylene and methyl groups in alkane groups from silane. The result shows some alkane chains have been attached on the surfaces.

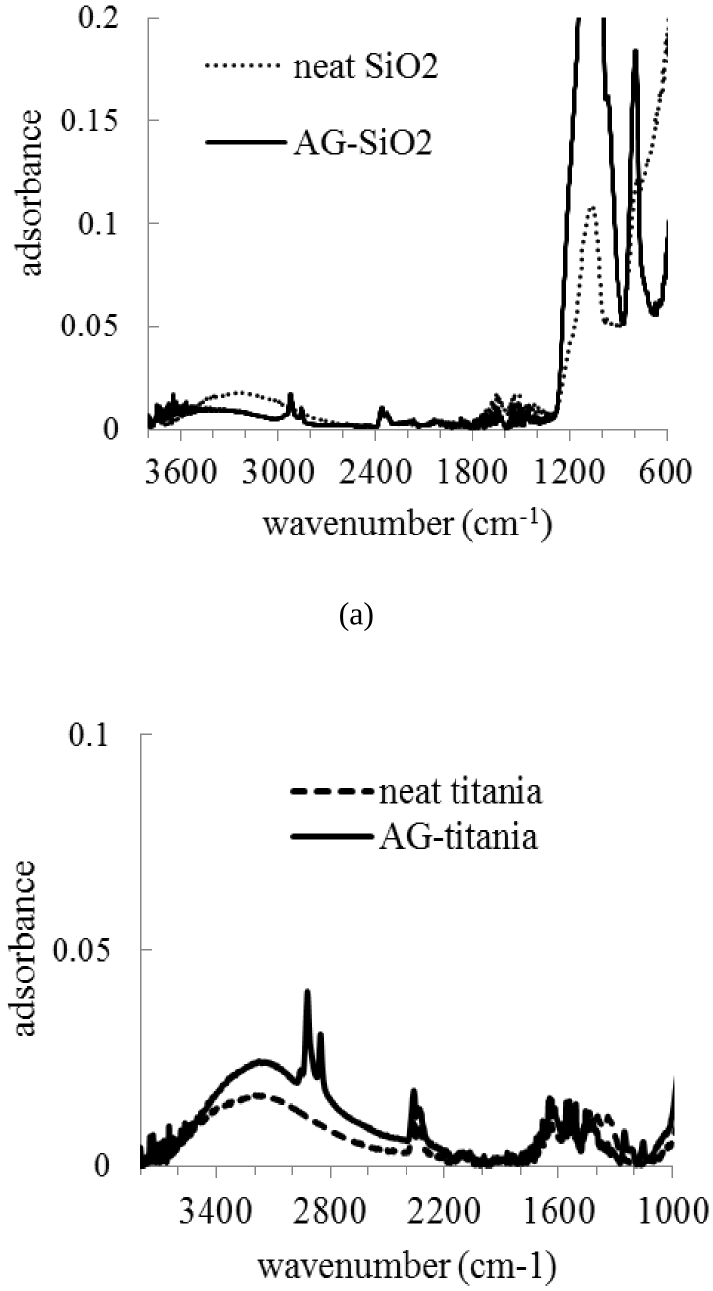

(a)

(b)

Figure 3.5 FTIR spectra of (a) neat and AG-SiO_2 and (b) neat and AG-TiO_2 nanoparticles

3.4.3 TGA characterization of neat and alkane-grafted nanoparticles

TGA analysis

For verifying the initial surface density of hydroxyl groups and coverage of alkane chain after surface modification, thermogravimetric analysis (TGA) was used. Thermogravimetric analysis analysis in the absence of oxygen can show a number of weight loss events with temperature increases, which attributes different decoupling reactions. Physically-adsorbed water on the nanoparticles' surfaces typically desorb from room temperature to 110°C. At higher temperature, the surface hydroxyl groups, which exist on metal oxide nanoparticles with different level, can undergo dehydration. Two hydroxyl groups release a water molecule to form M-O-M bond.

For estimating the surface density of hydroxyl groups, the surface area per gram (S, nm^2/g) of nanoparticles was firstly estimated via Equation 4.1, based on the dimension obtained from the TEM pictures.

$$S_{NPs} = \frac{\text{surface}}{\text{mass}} = \frac{4\pi r^2}{\frac{4}{3}\pi r^3 \rho} = \frac{3}{r\rho} \qquad (3.1)$$

Where r is the nanoparticles' radius, and ρ is the density of bulk material, silica ($2.63 g/cm^3$) and titania (anatase, $3.9\ g/cm^3$).

The number of hydroxyls per gram of nanoparticles, F (# groups/g), can be estimated from the weight loss over specific temperature ranges.

$$F_{\text{hydroxyls}} = \frac{2\left(\frac{W_{water}}{Mw_{water}}\right) N_A}{W_{final}} \qquad (3.2)$$

Where, the factor "2" means two hydroxyls are lost for each molecule of water, W_{water} is the weight of water lost, and Mw_{water} is its molecular weight, N_A is the Avogadro's number, and W_{final} is the weight of the sample at the end of the TGA decomposition experiment. It is used as weight of pure nanoparticles in the sample.

$$F_{\text{alkane}} = \frac{\left(\frac{W_{alkane}}{Mw_{alkane}}\right) N_A}{W_{final}} \qquad (3.3)$$

Where, W_{alkane} is the weight loss of silane coating, and Mw_{alkane} is the molecular weight of alkane part in silane. The surface densities of hydroxyl and alkane groups were estimated by computing the ratio of F_i and S_i. Where r is the radius and ρ is the density of nanoparticles. Hence the surface density of hydroxyl groups is the ratio of hydroxyls per nanoparticle mass and specific surface area.

<u>TGA analysis of neat and AG-SiO_2</u>

Figure 3.6 shows TGA curves of weight percentages with temperature for neat and AG-SiO_2.

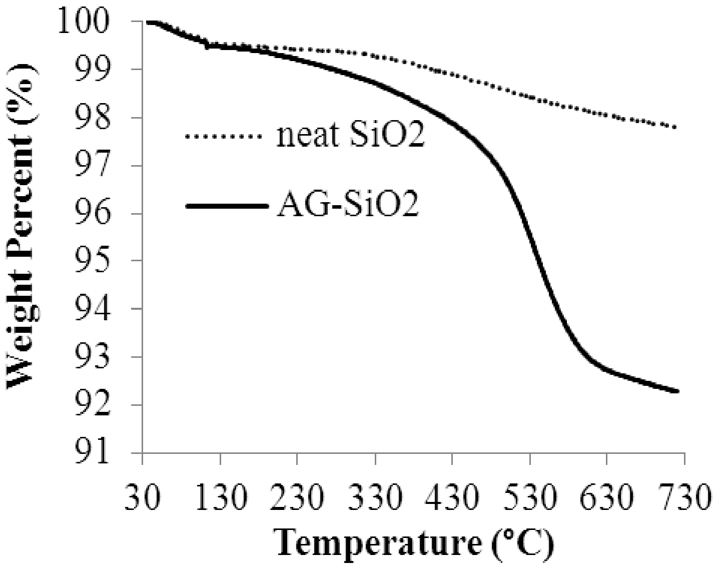

Figure 3.6 Weight loss curves with temperature of neat and AG-SiO_2 samples

The neat silica nanoparticles had a 0.47% weight loss between room temperature and 110 °C, representing physically-adsorbed water. Additional water (1.54%) is lost between the ranges 150°C to 720 °C. The water loss accelerates up to 550°C and then decreases. These are expected to be dehydration reactions at the nanoparticle surface. This mechanism is consistent with the previous literature that reported the vicinal hydroxyl groups dehydrated in the temperature range of 150 °C to 450-600 °C, and followed by slow dehydration of isolated hydroxyl groups (R.K.Ilner 1979, Sneh and George 1995). The total density of removed hydroxyl groups was calculated to be 6.6/nm^2 based on the average particle size of 12.9 nm, which is in the range of literature value (4-8 OH/nm^2) (Horacio E. Bergna 2006).

For the AG-silica nanoparticles, a large weight loss (15.2%) was shown in the TG curve above 150°C. The weight loss combined dehydration of remained hydroxyl groups and decomposition of alkane chain. Subtracting the 1.7% weight loss of neat silica at this temperature range, the normalized weight loss for fluoro chain is 0.06g per gram of pure silica nanoparticles. If we assume that the Si atom is left on the surface and other moiety (remained M_W=283.6) removes from the surface, the surface density of alkane chain on the surface was estimated to be 0.73/nm^2. The silane we used only has one active group, so it suggest the conversion percentage of hydroxyl groups is 0.73/6.6=11%. The diameter of silane molecule to be 1.1 nm based on its density (0.856 g/cm^3), therefore 0.73/nm^2 means the coverage of alkane chain is around 70%. The relative high coverage may lead to steric exclusion to following silane chain, so the conversion percentage was low.

TGA analysis of Neat and AG-TiO_2

Figure 3.7 shows TGA curves of weight percentages with temperature for neat and AG-TiO_2.

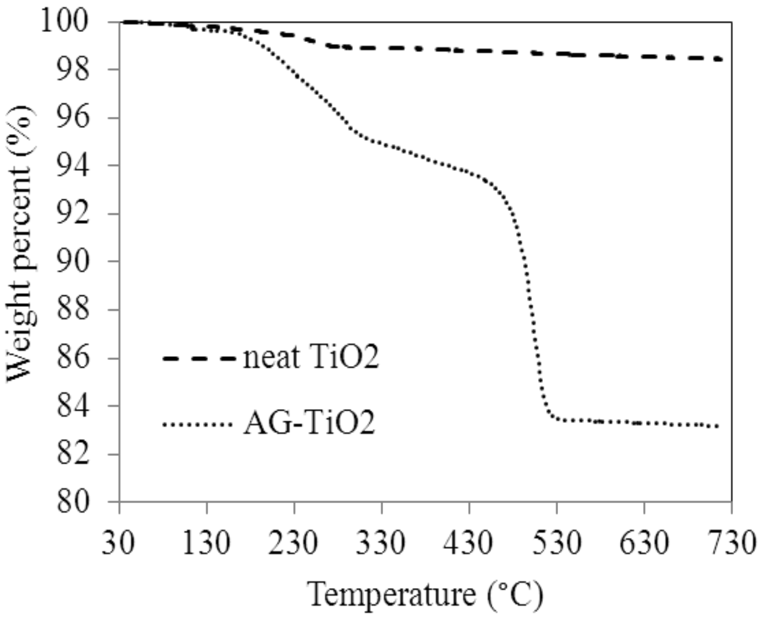

Figure 3.7 Weight loss curves with temperature of neat and AG-TiO_2 samples

Neat TiO_2 nanoparticles have a 0.2% weight loss between room temperature and 110 °C, representing the loss of physically-absorbed water. After that, the main weight loss (0.9%) happened between 110°C to 350 °C. It was consistent with the previous result that most hydroxyl groups on the surface of TiO_2 dehydrate below 350°C (Iwasawa 1986). The estimated value is 9.2/nm^2 based on the average particle size of 27 nm, in the range of literature value (6-11/nm^2) (Tamura 2002).

For AG-TiO_2 nanoparticles, there is large weight loss above 150°C. Subtracting the weight loss of neat TiO_2 at this temperature range, the weight loss for alkane chain is 0.19g per gram of pure TiO_2 nanoparticles. We can assume the Si part in the silane used was left on the surface and alkane moiety (MW=283.6) is removed from the surface. The surface density of alkane chain on the surface was estimated to be 5.6/nm^2. The diameter of silane molecule was estimated to be 1.1 nm based on its density (0.856 g/cm^3) so 5.6/nm^2 means the coverage of alkane chain is over 100%.

3.4.4 Particle size of neat and alkane-grafted nanoparticles in their dispersions

Figure 3.8 (top) shows the particle size distribution of AG-SiO_2 and neat TiO_2 in their dispersion (components of bilayer-1). Figure 3.8 (bottom) shows the particle size distribution of neat SiO_2 and AG-TiO_2 in monomer matrix (components of bilayer-2).

The neat TiO_2 has an average primary particle size of 9.6 nm. The average particle size is around 142 nm. It means small agglomerates forming in SR 415. There are larger agglomerates (peak at 330 nm) formed when AG-SiO_2 was dispersed in SR 415. It results from the alkane grafted surface doesn’t like hydrophilic monomer.

The neat SiO_2 has a uniform distribution in SR 415, the hydrophilic monomer. The average particle size is around 130 nm. It means only small agglomerates of SiO_2 forming in SR 415. There are larger agglomerates (peak at 238 nm) formed when AG-TiO_2 was dispersed in SR 415. It results from the alkane grafted surface doesn’t like hydrophilic monomer.

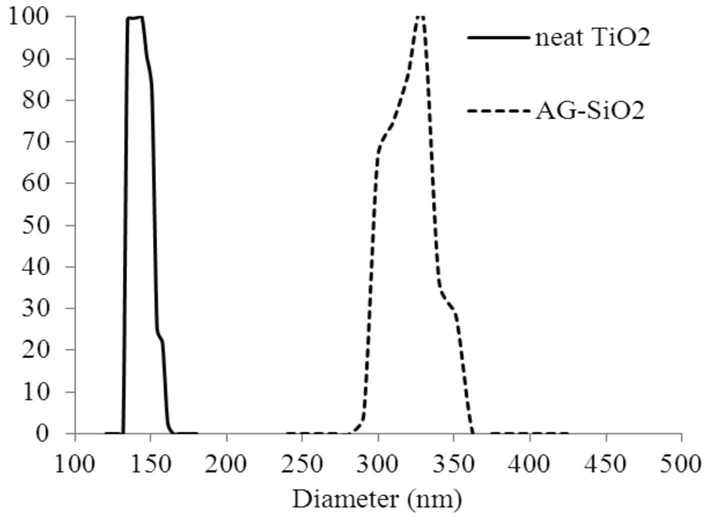

(a)

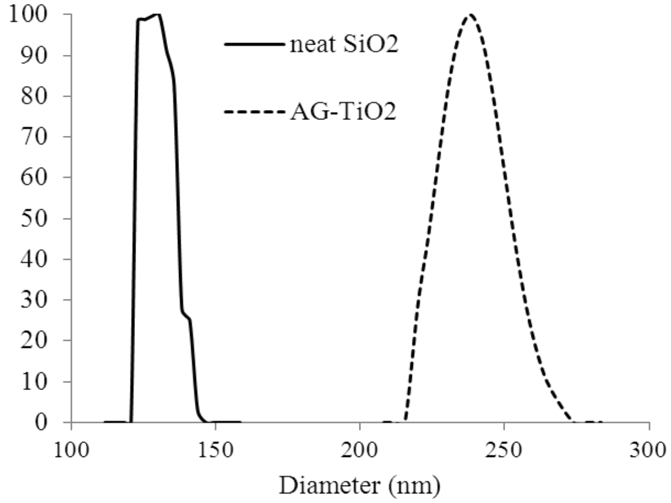

(b)

Figure 3.8 Particle size distribution in dispersions: (a) AG-SiO_2 and neat TiO_2, (b) neat SiO_2 and AG-TiO_2.

3.4.5 Composition analysis of ultrathin nanocomposite films

EDS analysis of bilayer-1 (AG-SiO_2, neat TiO_2 and hydrophilic monomer) and bilayer-2 (neat SiO_2, AG-TiO_2 and hydrophilic monomer) were shown in Figures 3.9.

The initial weight of SiO_2 nanoparticles was equal to TiO_2 nanoparticles so the atomic ratio between Si and Ti should be 4:3. For bilayer-1 sample, the SiO_2/TiO_2 was about 1:15, much lower than the initial atomic ratio. It means the neat TiO_2 nanoparticles were more concentrated in the hydrophilic monomer while the AG-SiO_2 far away from the outermost layer. It is consistent with the particle size result. The AG-SiO_2 with 330 nm agglomerates is easier to settle down from the monomer than neat TiO_2 with 142 nm agglomerates in spin coating process. The final bilayer structure has outer layer with high RI and inner layer with low RI.

For bilayer-2 sample, the atomic ratio between silica and titania is about 4:1. It means the neat SiO_2 nanoparticles were more concentrated in the hydrophilic monomer while the AG-TiO_2 far away from the outermost layer. It is consistent with the particle size result. The AG-TiO_2 with 238 nm agglomerates is easier to settle down from the monomer than neat-SiO_2 with 130 nm agglomerates in spin coating process. The final bilayer structure has outer layer with low refractive index and inner layer with high refractive index. Both structures are useful to create anti-reflectance and high reflectance thin films.

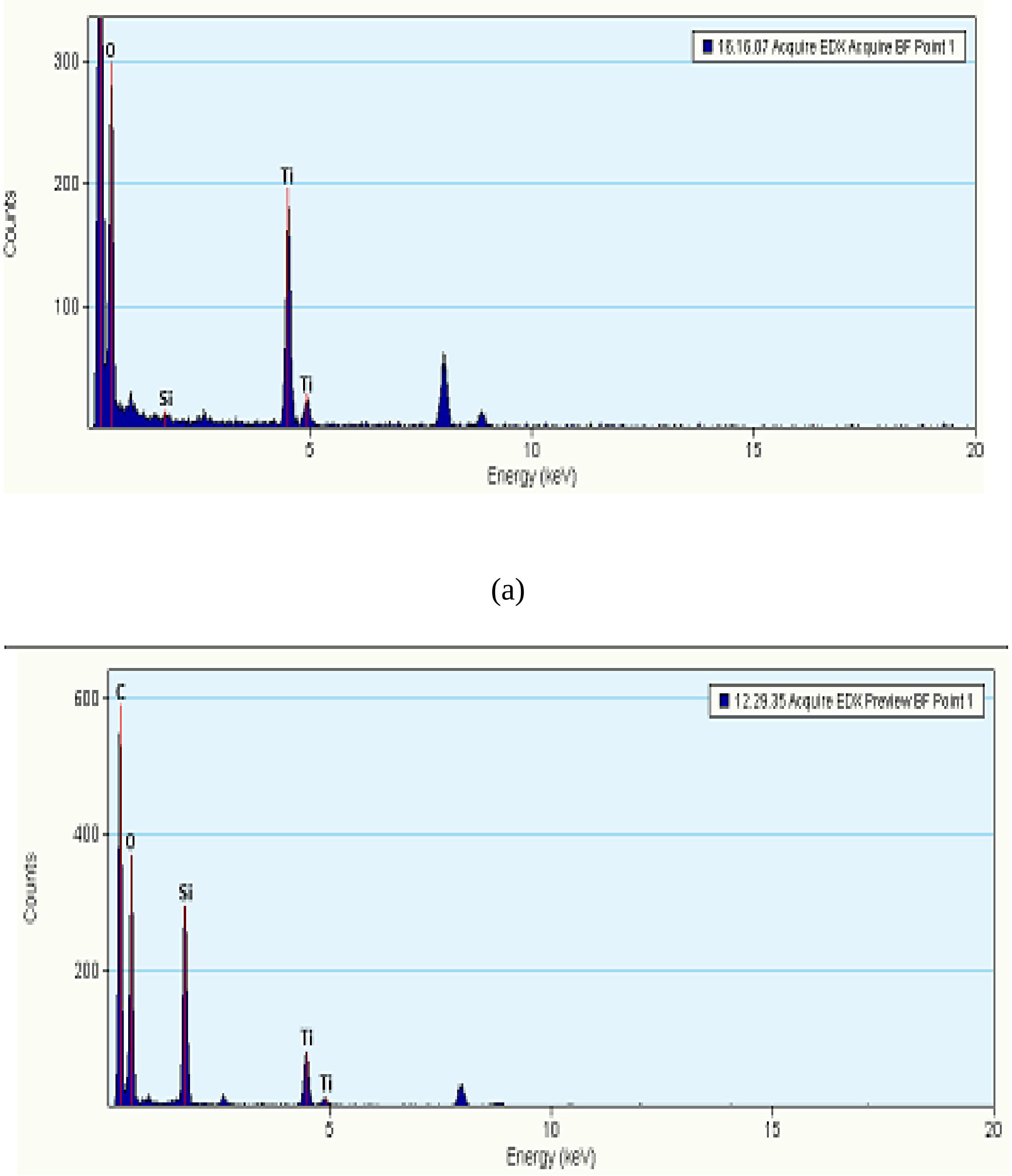

(a)

(b)

Figure 3.9 EDS analysis of bilayer-1 (a) and bilayer-2 (b) samples at the outermost layer

3.5 Conclusions

Silanization reaction was used to transform relatively hydrophilic surfaces of silica and titania nanoparticles to hydrophobic surface via attaching alkane chains. Thermo gravimetric analysis (TGA) was developed to analyze the initial surface density of hydroxyl groups and their conversion percentage to alkane chains. The neat nanoparticles has tendency to remain in monomer while alkane-grafted nanoparticles settle down easily. They are capable to segregate assembly to form bi-layer structure self-assembly in single deposition process. The Energy-dispersive X-ray spectroscopy (EDS) verifies that the bi-layer structure has been successfully obtained.

Chapter 4: Influence of surface charge on lysozyme adsorption to ceria nanoparticles

Much of the material in this chapter has been published at Applied Surface Science (Wang 2012).

4.1 Highlights

- Ceria nanoparticles with different surface charges were synthesized.
- Monolayer coverage amounts (jamming and maximum limit, side-on and end-on orientation, at surface with different curvature) were discussed
- Toth and Sip models were applied to fit adsorption behavior.
- Effect of surface charge and lateral effect are evaluated via parameters from Toth and Sips models.
- The local site energy distributions were estimated.

4.2 Introduction:

With rapid development and more applications of complex engineered nanoparticles (CENPs), they are inevitable to enter biological and environment, interact with the biological macromolecules. Nanomaterials medical agents are frequently given via parenteral administration. When CENPs contact a biological environment, proteins can bind to their surface immediately, creating protein coronas (Cedervall, Lynch et al. 2007, Sahoo, Goswami et al. 2007, Lynch and Dawson 2008). Biodistribution of the CENPs is affected by this protein coating. Understanding the principles governing the formation of the corona and the effects of the surface properties of CENPs themselves, play a central role in selecting nanocarriers for drug delivery. The project focused on adsorption equilibria of lysozyme, one protein with positive charge in acetic acid/acetate buffer, with ceria with an average diameter of 12 nm, having different surface charges in the buffer:

negative, near neutral and positive.

Ceria, a rare earth metal oxide with two oxidative states of cerium, Ce (III) and Ce (IV), possesses unique chemical properties in a redox reaction (Land 1973, Suzuki, Kosacki et al. 2001). Nanoceria are being used as an additive to diesel fuel to reduce soot, and for wafer planarization in the electronics industry since 1999. Recently, nanoceria has been found to scavenge reactive oxygen species and has been proposed as an antioxidant to promote organism longevity. Rzigalinski et al. reported that ceria nanoparticles (NPs) of the size range of 6-20 nm prolong the lifespan of mixed brain cell cultures (Rzigalinski 2005). Based on their ability to protect cells from free radical mediated injury and known chemical activities, they suggested that ceria NPs are acting in a redox capacity within the cells. Seal et al. reported that nanoceria provide radioprotection to normal cells from radiation (Tarnuzzer, Colon et al. 2005). Moreover, they found that nanoceria possess superoxide-dismutase-like activity (Korsvik, Patil et al. 2007). These findings show that ceria is a potential candidate for antioxidant and radioprotective applications.

Our previous pharmacokinetics study of the distribution of ceria nanomaterials in blood showed that, on clotting, both 15- and 30-nm ceria samples partitioned to the clot fraction, rather than the serum, over time (Hardas, Butterfield et al. 2010). The clot contains most cells, platelets and protein. This partitioning performance is likely to be caused by changes in their surface chemistry, such as loss of the functionalizing agent, association with proteins or blood cells, and/or cell entry.

Lysozyme was the model protein in this study. It is present in blood and has an isoelectric point (net charge of lysozyme is zero at this point) around 11 in water (Burton, Nugent et al. 1988). Lysozyme’s conformation in aqueous solutions is affected by solvents (Bonincontro, De Francesco et al. 1997) and pH. Between pH 4 and 6, lysozyme’s conformation is relatively stable. The isotherms were measured in dilute acetate buffer (pH ~ 4.3) with ceria functionalized to have different charges. The interactions between lysozyme and ceria surface with different charges are complicated. In general, solute adsorption occurs on surface sites with a range of energies, i.e., the site energy distribution was important. The heterogeneity can arise from two main factors: surface heterogeneity and lateral effect between adsorbed moleculues. Surface heterogeneity includes surface morphologies with irregular shape or small pores and multiple types of surface functional groups. Commercial nanoparticle samples often have been functionalized to improve their performance in specific applications. While the net charge on lysozyme at pH 4.3 is positive, it has a symmetrical distribution of positive charges and an asymmetric distribution of negative charges. This protein can adsorb to both negative and positive surfaces, but can have preferred orientations for a specific surface. Adsorption of proteins to oppositely charged surfaces (such as electrostatically-driven protein adsorption to ion exchange resins) has been modeled using colloidal models (Asthagiri and Lenhoff 1997, Xu and Lenhoff 2008). However, continuum electrostatic is not always adequate to capture all adsorption behavior and additional molecular interactions need to be addressed (Yao and Lenhoff 2005). Protein adsorption characteristics have been modeled by Brownian dynamics (Ravichandran, Madura et al. 2001, Ermakova 2005) and Monte Carlo simulations (Zhou, Chen et al. 2003, Zhou, Tsao et al. 2004, Zhou, Zheng et al. 2004, Xie, Zhou et al. 2010). The simulations showed that both van der Waals and electrostatic forces influence the orientation of proteins on charged surfaces. Experimentally, the surface charge distribution on lysozyme has been shown to affect its adsorption orientation to lipid monolayers (Tiemeyer, Paulus et al. 2010). The second factor, lateral interactions between adsorbed molecules on the adsorbent surface, was also important(Al-Muhtaseb and RItter 1999, Podkoscielny 2008). When a solute adsorbs on a heterogeneous surface, it may not readily de-adsorb or be displaced by competing solutes, thus modifying the surface for the uptake of other species. Adsorbed molecules can have attractive forces (positive cooperative effect) or repulsions (negative cooperative effect) to neighboring molecules. Examples of this phenomenon are humic acid adsorbing on activated carbon (Carter 1995) and proteins adsorbing on nanoparticles, respectively (Caracciolo 2011).

Since heterogeneous site energy distributions were expected, we used two models, the Toth model and the Sips model, that contain heterogeneity coefficients. The approximate site energy distribution function can be obtained through their heterogeneity coefficient and the condensation approximation proposed by Cerofolini . The method is relatively simple, and has been applied to the adsorption of various gas molecules and some organic adsorbents in aqueous solution on activated carbon (Cerofolini 1974, Carter 1995, Kumar, Monteiro et al. 2011). Our aim was to clarify the effect of surface charge and lateral effect by heterogeneity coefficient in models and apply the site energy distribution analysis to our ceria-lysozyme system. They are useful to interpret the formation of the protein 'corona' on the surface of nanoparticles.

The study reports the adsorption behavior of a positively charged protein, lysozyme, on cerium dioxide (ceria) nanoparticles with three different surface charges. Adsorption isotherms were modeled with the Toth and Sips equations. Comparison of the loading levels to monolayer coverage estimate for 'side-on' and 'end-on' lysozyme molecules suggested that adsorbed lysozyme had different orientations on the three different nanoparticle surfaces. Evaluation of adsorption site energy distributions (generated using the model coefficients) suggested that the negatively charged ceria surface had a very broad site energy distribution and that its surface heterogeneity controls the adsorption process. By contrast, the adsorption of lysozyme on the positively charged nanoparticles appears to be influenced by lateral effects from adsorbed protein species. The results illustrate the importance of nanoparticle surface chemistry to protein adsorption. The modeling and site energy distribution evaluations can be used to interpret formation phenomena associated with protein coronas on nanoparticles.

4.2 Experiments

4.2.1 Synthesis of ceria NPs with three different coatings

12 nm ceria NPs were synthesized using a hydrothermal approach (Pan, Zhang et al. 2008). In a typical procedure, 1.5 mmol cerium nitrate hexahydrate (Sigma-Aldrich # 22350, >99.0%) and 0.5 mmol hexadecyltrimethylammonium bromide (CTAB, Sigma-Aldrich #H9151, ~99.0%) were dissolved in 20 ml water. 2 ml ammonium hydroxide (Fisher # 3256, ACS, 28-30%) was drop wise added into the mixture and kept stirring for 0.5 h to form a brown emulsion. The CTAB surfactant stabilizes the growing nanoparticles, controlling their ultimate particle size. The emulsion was transferred into a Teflon-lined stainless steel bomb and heated at 120 °C for 24 h to complete the reaction. The fresh product was washed with water three times, ethanol twice to remove free ceria salt, most of CTAB, and other impurities, and then dried in an oven at 65°C for 12 h. The "as-synthesized" ceria have certain hydroxyl groups on the surface that can be modified (Tok, Boey et al. 2007) to change their surface chemistry.

Citrate-coated ceria nanoparticles were generated by coating the as-synthesized 12 nm ceria NPs with citric acid (EMD Chemicals Inc # CX1725-1, GR ACS), which is relatively nontoxic and widely used in biological and medical applications. The nanoparticles were dialyzed with fresh citric acid aqueous solutions for three times followed by water wash to get rid of free citric acid and dried at 65°C for 24 h.

Aminosilane-coated ceria nanoparticles were generated by silanization of 12 nm as-synthesized ceria with ureidopropyltrimethoxysilane ureidopropyltrimethoxysilane (Gelest # SIU9058.0) in an alcohol/water mixture. Generally, a 95% ethanol and 5% water solution was adjusted to pH 4.5 using acetic acid. The silane was stirred in, followed by as-synthesized 12 nm ceria powder. The methoxy groups on the silane are converted to hydroxyls at the reaction conditions. These can condense with surface hydroxyls on the ceria or hydroxyls on other silane molecules. The silane proportions were set so that there were sufficient silane molecules to attach one silane molecule to each hydroxyl on the ceria surface (~12 [OH]/nm^2). The mixture was stirred for 12 h at 70°C to complete silanization. The product was washed with ethanol three times and water once to remove extra silane, then dried at 65°C for 12 h.

4.2.2 Characterization of ceria nanoparticles

Elemental analysis and particle morphology

The three ceria nanoparticles were dispersed into methanol to form much diluted dispersion. Copper grits were dipped into the dispersion so some ceria nanoparticles will transfer to the surface of copper grit. The morphology and crystallinity of ceria samples was evaluated using a 200-keV field emission analytical transmission electron microscope (JEOL 2010F, Tokyo, Japan), 200-keV field emission TEM equipped with an Oxford energy dispersive X-ray spectrometer and Gatan 794 CCD (charge coupled) camera. Electron energy loss spectroscopy (EELS) was used to determine the Ce(III)/Ce(IV) ratio from the M5/M4 ionization edges and was performed using a JEOL 2010F STEM outfitted with a URP pole piece, GATAN 2000 GIF (Pleasanton, CA, USA), GATAN DigiScan II, Fischione HAADF STEM detector (Export, PA, USA), and EmiSpec EsVision software (Tempe, AZ, USA). STEM images were acquired using the high resolution probe at 2 Angstrom and EELS was performed using the 0.2 Angstrom probe, alpha of 30 mrad, and a beta of 6 mrad. Primary particle size distributions were determined by TEM analysis (Mandzy, Grulke et al. 2005). The crystallinity of all ceria ENMs were determined by XRD (Siemens 5000 diffractometer).

Surface coating determination

The Fourier transform infrared spectroscopy (FTIR) method was used to detect the functional groups on the surface of ceira samples. Before the experiments, ceria samples and KBr as pellet mater were heated in an oven at 80°C for 24 h to evaporate the physically absorbed water. The ceria powder was mixed with KBr at 1:200. 50 mg of the mixture was pressed to the pellet. The FTIR spectra were recorded with a Thermo Nicolet NeXus 470 FT-IR Spectrometer operated in the range of 400 – 4,000 cm^{-1}. Thermogravimetric analysis (Perkin-Elmer TGA7 Analyzer) was performed to investigate the weight loss of as-synthesized, citrate-coated and aminosilane-coated ceria NPs under nitrogen atmospheres at a gas flow rate of 20 ml/min. The samples were held at T ~100°C for 30 min to drive off water absorbed on the ceria surface or in the coating. The temperature was steadily increased up to 750°C at a rate of 10°C/min. The weight loss from decomposition of citric acid and aminosilane were used to calculate the surface coating percentage of each ceria NPs. The extent of citrate/silane surface coating was estimated based on the assumption that all the ceria NPs were spherical and had uniform size(V. Kanniah 2012).

Zeta potential determination

To investigate the surface charge of ceria NPs and its change with pH condition, zeta potential curves were determined for each NP using a Zetasizer 2000 (Malvern Instruments, Worchestershire, UK). The concentration of each ceria NP aqueous suspension was about 15 μg/ml. Sodium hydroxide and hydrochloride acid were applied to adjust the pH of suspension. At each pH, four readings were recorded. The experimental data were fitted using a Carreau equation since it models two “plateau” areas at high and low pH values and a logarithmic region between these two extremes (Shenoy 1998).

$$\frac{\zeta-\zeta_0}{\zeta-\zeta_\infty} = [1 + (a * 10^{pH})^2]^{\frac{b-1}{2}} \qquad (4.1)$$

Where ζ is the zeta potential at a specific pH, ζ_0 is the limiting zeta potential at low pH, ζ_∞ is the limiting potential at high pH, pH is the negative log of the hydrogen ion concentration, and a and b are coefficients. The isoelectric point (IEP) was computed using model coefficients to solve for the pH at which $\zeta=0$.

Protein determination using UV-vis spectroscopy

Ten ml 0.05 v% of ceria NPs aqueous suspension was prepared. 1.1, 2.5, 3.8, 5, 6, 7.4, 10.5 and 13.7 mg lysozyme from chicken egg white (Sigma-Aldrich # L6876), were dissolved in 5 ml acetate buffer (pH ~4.3) and added to the ceria aqueous suspensions. The protein/ceria suspensions were equilibrated in glass bottles with fastened lids under stirring conditions at 25°C for 18 h. To determine the amount of surface adsorbed protein, 9 ml suspensions were withdrawn from the mixture of ceria with lysozyme after 18 h and placed in 15 ml plastic centrifuge tubes. Subsequently, the tubes were centrifuged at 4200 rpm for 30 min at 25°C. The top ~2 ml of supernatant was transferred to plastic bottles and protein concentration was determined by using the Bradford method (Bradford 1976). Following the method, the visible absorption values of the protein samples were measured at a wavelength of 595 nm, using an UV/vis spectrometer (UV-2501PC, SHIMAZDU Scientific Instruments). The results were compared to reference curves for lysozyme, which had a minimal detection limit of 2.5 μg/ml. The adsorbed amount of lysozyme was calculated from the protein concentration left in the supernatant and the total amount of protein added in the beginning.

4.3 Adsorption isotherm models for organic molecules on nanoparticles

The adsorption of organic molecules on nanoparticles is complex. It is influenced by many factors; including the nanoparticle surface (charge, functional group, shape, local curvature and energy distribution) as well as the protein properties (net charge, hydrogen bonding and charge distribution). The Langmuir isotherm (4.2) has been a common starting point (Toth 2002).

$$q_e = \frac{q_m K_L C_{eq}}{1+K_L C_{eq}} \qquad (4.2)$$

where q_e, is adsorption amount normalized by mass of nanoparticles, q_m is the maximum adsorption capacity for monolayer, C_{eq} is the concentration in supernatant at the adsorption equilibrium, and K_L is a temperature-dependent parameter related to the energy of adsorption.

The Langmuir model applies strictly to homogenous surfaces since it assumes the energy distribution is uniform for all surface sites. The energy distribution on adsorption of protein on nanoparticles, however, usually shows heterogeneous behavior. It results from the surface heterogeneity and the lateral effect between adsorbed molecules described above. Two empirical models for heterogeneous adsorption were used in our study: the Toth equation (4.3 a) and the Sips equation (4.3 b), which considered the influence of both factors (Toth 2002).

$$q_e = q_{\mathrm{m}} \left(\frac{K_T C_{\mathrm{eq}}^t}{1+K_T C_{\mathrm{eq}}^t}\right)^{1/\mathrm{t}} \qquad (4.3\ \mathrm{a})$$

$$q_e = q_{\mathrm{m}} \frac{K_S C_{\mathrm{eq}}^t}{1+\mathrm{K}_S C_{\mathrm{eq}}^t} \qquad (4.3\ \mathrm{b})$$

where q_m and C_{eq} are defined as for the Langmuir equation, K_S and K_T relate to the adsorption energy, and t is a heterogeneity coefficient. The Toth model was often used to model the heterogeneous adsorption of organic molecules on nanoparticles. The Sips equation, which is equivalent to the Hill equation in biochemistry, is also used to model cooperative adsorption between macromolecules and ligands(Gokel 2006). The magnitude of t has been linked to the factors affecting heterogeneous adsorption. When $0 < t < 1$, the heterogeneity is considered to be linked to variations in the solid surface. When the adsorbed molecule has strong affinity to other adsorbent molecules (a positive cooperative effect), t will be greater than 1 (Toth 2002, Kowalczyk 2003).

The relationship between adsorption amount and site energy distribution can be represented by the Fredholm integral equation (4.4).

$$q_e(C) = \int_{E_{min}}^{E_{max}} q_h(E, C) f(E) dE \qquad (4.4)$$

where q_e is the total adsorption amount. It was represented by the integral of energetically homogeneous surface with adsorption amount (q_h) multiplied by a site energy frequency distribution, f (E).

It is difficult to solve the above integral to get the exact site energy distribution. The simple condensation approximation proposed by Cerofolini (Cerofolini 1974)can be used to obtain an approximate site energy distribution on a heterogeneous surface. Applying the assumptions of the Cerofolini approximation, this approach relates the equilibrium liquid phase concentration to the binding energy (Seidel and Carl 1989, Carter 1995).

$$C_{eq} = C_S exp\left(-\frac{E-E_S}{RT}\right) = C_S exp\left(-\frac{E^*}{RT}\right) \qquad (4.5)$$

Where C_s is the maximum solubility of the solute in the solvent, E is a specific site energy, E_s is the value of the minimum adsorption energy corresponding to $C_{eq}=C_s$, R is the universal gas constant, and T is the absolute temperature.

This equation was developed for modeling adsorption from the gas phase in which the saturated vapor pressure is used as a reference state (p/p_{sat} is often used to define the solvent activity). Seidel (Seidel and Carl 1989) and Carter (Carter 1995) consider C_s to be a reasonable choice as a reference state. In our studies, C_s=7.09 mg/mL after considering ionic strength (3% NaCl) and buffer concentration (0.1 M) (Forsythe and Pusey 1996).

Substituting Equation 4.5 into the isotherms (Equation 4.2 and 4.3) gives an equation for q_e written in terms of the binding energy, E*. The approximate site energy distribution, f(E*), is obtained by differentiating the isotherm, q_e (E*).

$$f(E^*) = -\frac{dq_e(E^*)}{dE^*} \qquad (4.6)$$

The energy distribution function for the Toth expression is

$$f(E^*) = \frac{q_m C_s}{K_T RT} exp\left(\frac{tE^*}{RT}\right)\left(C_s^t + \frac{exp(tE^*/RT)}{K_T}\right)^{-(t+1)/t} \qquad (4.7)$$

where the q_m, K_T and t are the parameters from Equation 4.3 a.

The energy distribution function for the Sips expression is

$$f(E^*) = \frac{q_m K_S C_S^t t}{RT} \frac{exp(tE^*/RT)}{exp(2tE^*/RT) + 2K_S C_S^t exp(tE^*/RT) + K_S^2 C_S^{2t}} \qquad (4.8)$$

where the q_m, K_s and t are the parameters from Equation 4.3 b.

The resulting site energy distributions for different data can be normalized by setting the area under the distribution curve to be equal to the maximum adsorption capacity, q_m.

$$q_m = \int_{E^*_{max}}^{E^*_{max}} f(E^*) dE^* \qquad (4.9)$$

Using Equations 4.7-9, site distribution energies for different materials can be compared on a normalized basis.

In our studies, equations 4.3 (a) and 4.3 (b) were used for fitting the isothermal data of lysozyme on ceria nanoparticles. The parameters obtained were used for generating the approximate site energy distribution curve based on equations 4.7 and 4.8. These energy distribution curves were normalized using Equation 4.9.

4.4 Results

4.4.1 Purity and morphology of as-synthesized ceria NPs

The as-synthesized ceria NPs were crystalline, having a typical fluorite structure (card no: 034-0394, Figure 4.1 a). The average primary particle size of as-synthesized ceria NPs was determined by sizing over 80 individual particles via the TEM images (Figure 4.1 b). From the data, number frequency cumulative distributions were constructed. These cumulative distributions were best described by a lognormal distribution model, which was characterized by a sample mean and its standard deviation (Figure 4.1 c). The as-synthesized ceria nanoparticles are polyhedral with an average diameter of 12.0 ± 2.9 nm. Since the peak ratio of M5 to M4 is greater than 1 (Figure 4.1 d), the ceria NP surfaces are rich in Ce^{3+} (Wu, Wiesmann et al. 2004). Because of these oxygen vacancies, ceria nanoparticles may be ideal antioxidants for scavenging oxygen species. The citrate- and amino-silane coated ceria NPs have very thin coatings, which were not observed using TEM.

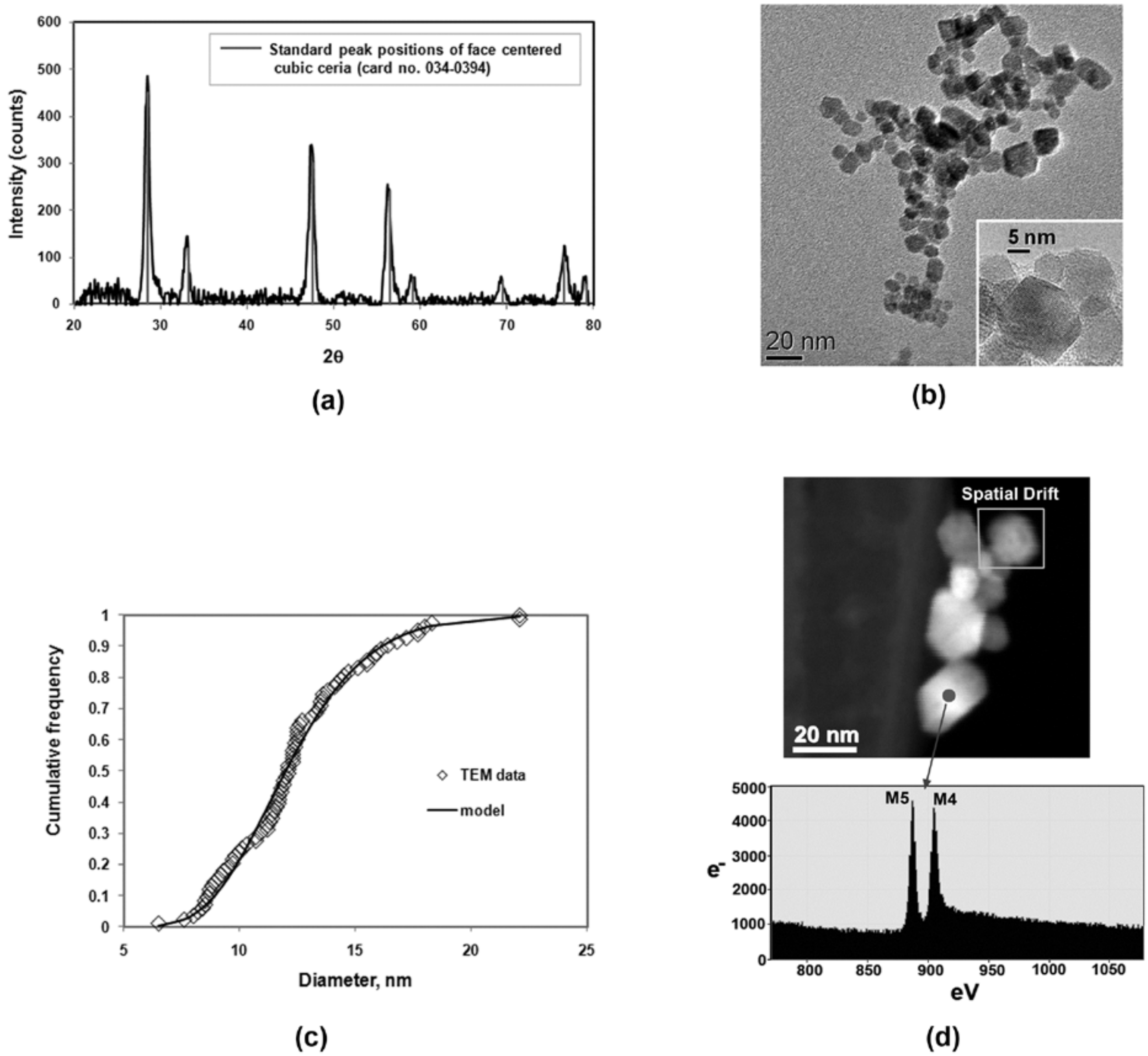

Figure 4.1 Crystal structure, primary particle size and valence state of as-synthesized ceria nanoparticles

(a) XRD pattern, the peak positions agree to cubic ceria standard (fluorite crystal structure); (b) High-resolution TEM images, the shape of ceria NPs are polyhedron; (c) Lognormal model is applied to fit the TEM image data with the determined primary particle size of 12.0 ± 2.9 nm; (d) EELS results show that the ratio of M5 over M4 is over 1, i. e. the surface of ceria NPs is Ce^{3+} rich.

4.4.2 Chemistries/morphologies of ceria NP surface coatings

Characterization of surface coating via FTIR

Figure 4.2 shows the FTIR spectra of as-synthesized, citrate and aminosilane-coated ceria NPs. The FTIR spectrum of citrate-coated ceria NPs showed three peaks at 3400, 1591 and 1370 cm $^{-1}$ (Fig. 2). The first was attributed to the stretching band of the hydroxyl group and the other two were assigned to the anti-symmetric and symmetric stretching band of the carboxyl group. The aminosilane-modified ceria NPs had two peaks associated with amines. The broad peak at 3380 cm $^{-1}$ may be attributed to the N-H vibration in primary or secondary amines. The peak at 1574 cm $^{-1}$ was specified as the carbonyl band absorption of secondary amines. A new peak at 1000 cm $^{-1}$ was detected, corresponding to the absorption band of the $Si\text{-}C_2H_5$ bond(Gokel 2006). Two weak broad peaks between 1600 to 1200 cm $^{-1}$ were detected in as-synthesized ceria NPs, which may be attributed to some CTAB groups on the surface (estimated in the next section).

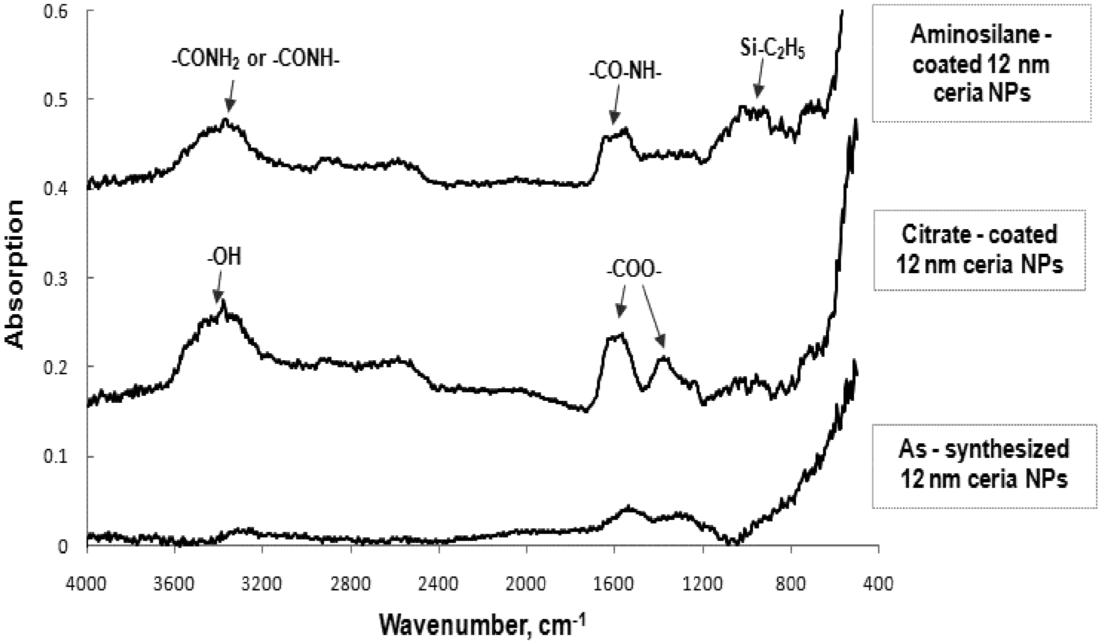

Figure 4.2 FTIR spectra of as-synthesized, citrate and aminosilane-coated ceria NPs

Surface coverage of coating via TGA

In TGA experiments, some decoupling reactions will take place on the surface of nanoparticles with the increase of temperature. Other than the removal of adsorbed water and dehydration of hydroxyls (typical of most metal oxide surfaces), the main surface decoupling reactions were the decarboxylation of citrate-coated ceria, decomposition of the amine-alkane chain of the aminosilane-coated ceria, and decomposition of CTAB. Using mass measurements from the TGA, we can estimate the functional group density and coverage on the NP surface.

The number of hydroxyls per unit mass of nanoparticles ($F_{\text{hydroxyls}}$, #[OH]/g) and created alkane or silane chains can be estimated by Equations 4.10 a-b.

$$F_{\text{hydroxyls}} = \frac{2\left(\frac{W_{water}}{Mw_{water}}\right)N_A}{W_{final}} \qquad (4.10\ \text{a})$$

$$F_{\text{other}} = \frac{\left(\frac{W_{other}}{Mw_{other}}\right) N_A}{W_{final}} \qquad (4.10\text{ b})$$

Where W_{H2O} = removed water from dehydration of hydroxyls and W_{other} = molecules from decomposition of the citrate coating or amino-alkane chain. The M_{H2O} and M_{other} are the molecular weight of water, citric acid and amino-alkane moiety in silane; N_A is Avogadro's number. W_{H2O} and W_{other} were normalized to the unit mass of the nanoparticles.

The ceria nanoparticle specific surface area (S, m^2/g) was calculated based on the primary particle size and its spherical shape.

$$S_{ceria} = \frac{surface}{mass} = \frac{4\pi r^2}{\frac{4}{3}\pi r^3 \rho} = \frac{3}{r\rho} \qquad (4.11)$$

The functional groups per area ($\#/nm^2$) were computed using the ratio between functional group per unit mass of nanoparticles and the specific surface area value.

Figure 4.3 shows TGA curves of as-synthesized, citrate and aminosilane-coated ceria nanoparticles with temperature.

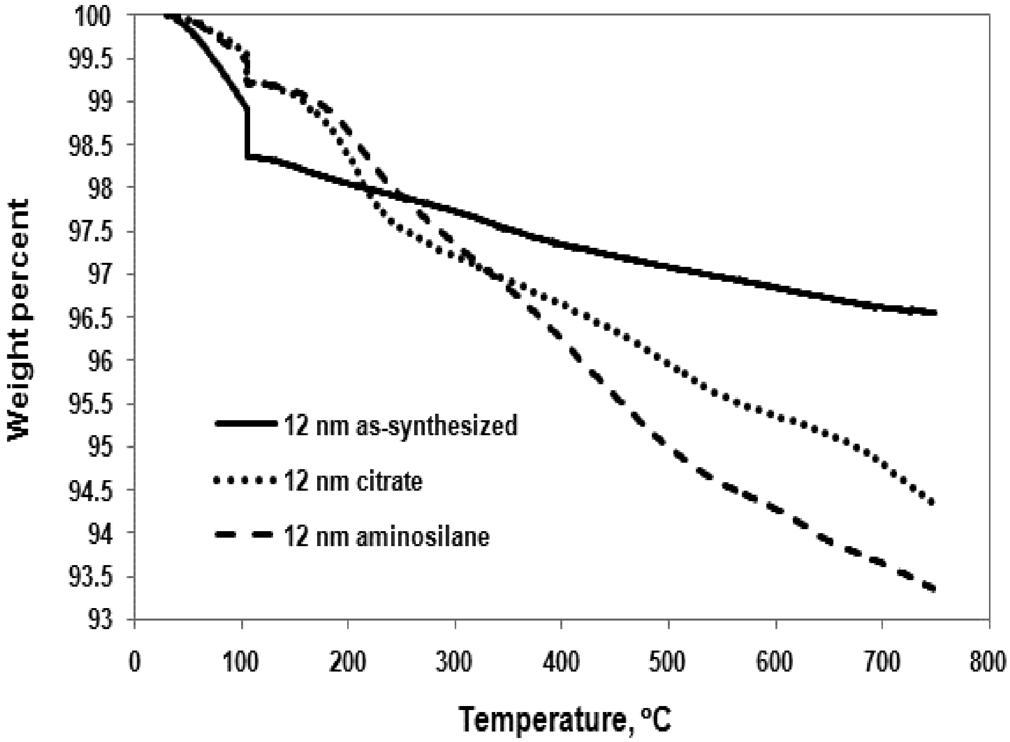

Figure 4.3 Weight loss curves with temperature of as-synthesized, citrate and aminosilane-coated ceria nanoparticles

As-synthesized ceria nanoparticles show weight loss (1.71%, normalized) below 105 °C; this is water adsorbed to the surface. Above 105 °C, both decomposition of CTAB and dehydration of hydroxyl groups occur. Pure CTAB decomposed within the range of 230 to 350°C at the same experimental conditions. The weight loss (0.51%, normalized) from 230°C to 350°C is attributed to decomposition of remaining CTAB. The surface density of CTAB was estimated to be 0.12 groups/nm^2. The average volume of CTAB molecules is 0.469 nm^3 (crystal state(Zhao, Du et al. 2006)), suggesting that the surface coverage is 9% CTAB coated.

Citrate-coated ceria nanoparticles lost 0.83% of their weight below 105 °C. Above 105 °C, the main decoupling reaction is the decomposition of the citrate coating. Pure citric acid decomposed within the range of 150 to 350°C under the same experimental conditions. The weight loss (2.39%, normalized) between 150 and 350°C is attributed to decomposition of the citrate coating. The surface density of citric acid can be estimated to be 1.1 groups/nm^2. The average diameter of citric acid molecules is in the range from 0.57 (hydrodynamic) to 0.72 nm (crystal state) (van Drunen, Finsy et al. 1993), suggesting that the surface coverage is 27% to 43%.

Aminosilane-coated ceria lost 0.86% of their weight in water during the bake-in process. Within the temperature range between 200 and 600°C, there was an apparent weight loss on the TG curves. The weight loss (4.79%, normalized) was mainly due to a decomposition reaction of the amino-alkane chain since the pure silane sample decomposed at the same temperature range at the experimental conditions. Subtracting the normalized weight loss of as-synthesized ceria (1.33 %, normalized) within this temperature range, the weight loss attributed to the silane was 3.5 %. We can assume the Si part in the ureidopropyltrimethoxysilane was left on the surface and the rest of the ligand (MW=101) decomposed from the surface. The surface density of the amino-alkane chain on the surface was 3 silanes/nm^2 (25% of the silane in the functionalization mixture reacted to form the surface coating). The average diameter of the silane is ~0.85 nm, so a spherical molecule would occupy 0.322 nm^3. The occupied volume of silanes per square nm of surface would be 0.965 nm^3 (silanes)/nm^2. Assuming that the silanes are randomly close packed (0.637 fractional occupied volume), the coating volume was 1.5 nm^3 per square nm of surface, which was equivalent to ~ 1.7 times the thickness of a silane ‘monolayer’.

4.4.3 Surface charge of three NPs via Zeta-potential measurements

The stability of ceria NPs in water and their charge properties were determined by zeta potential titrations. The curves of zeta vs. pH over the range of 3.5 to 8.2 are shown in Figure 4.4. Model curves via Equation 4.1 were used to estimate IEPs. Both as-synthesized and aminosilane-coated sample appear to follow the expected model of a constant value (plateau) at low pH, a region of change, followed by a second plateau. The citrate-coated sample doesn't have a plateau at low pH in this figure. The data are shown as points and the models are shown as continuous curves. The isoelectric point is taken to be where the model crosses zero line.

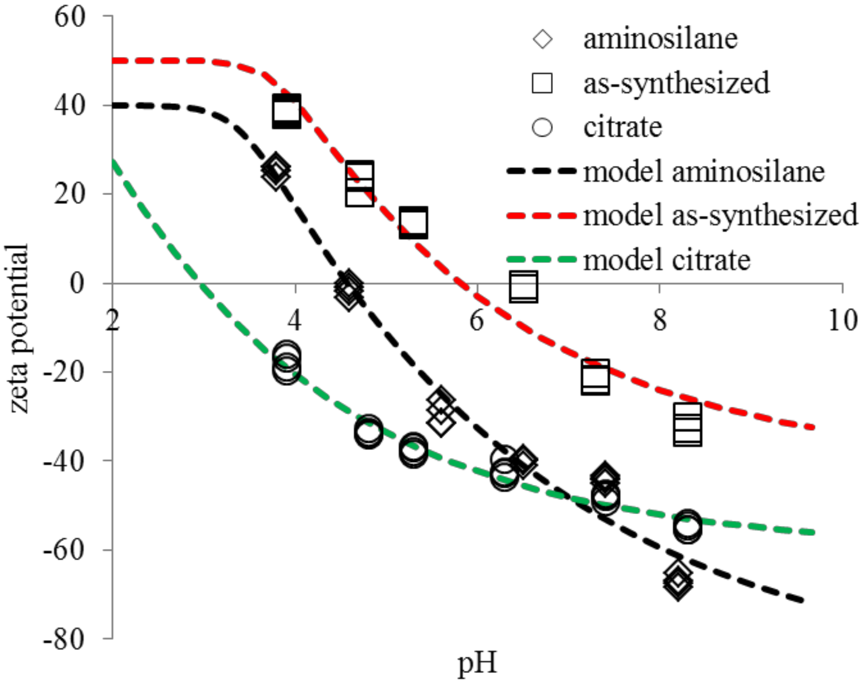

Figure 4.4 Zeta potential curves of as-synthesized, citrate- and aminosilane-coated ceria nanoparticles aqueous suspensions.

The as-synthesized ceria NPs has the highest IEP (~ 6.0) among the three ceria NPs. CTAB, which has a net positive charge, was used to control nanoparticle primary particle size and ensure dispersion stability (no agglomeration or aggregation were observed during synthesis). The washing procedure removes most absorbed CTAB, although a small fraction remains. The citrate-coated ceria NPs had a lowest IEP (~3), while aminosilane-coated ceria NPs have an IEP around 4.5. As previously reported, lysozyme adsorption experiments were done at ~pH 4.3, at which the protein is positively charged (its IEP is about 11(Rezwan, Studart et al. 2005)). At this pH, the charges on the three samples were positive (as-synthesized ceria; $\zeta = 32.3$ mV), neutral (aminosilane-coated ceria; $\zeta = +7.0$ mV) and negative (citrate-coated ceria; $\zeta = -25.5$ mV) respectively. Hence, if adsorptions of lysozyme and humic acid ion are influenced by electrostatic forces, these three ceria nanoparticles should induce different adsorption behaviors.

4.5 Adsorption isothermal for lysozyme on ceria NPs

4.5.1 Protein adsorption isotherms

The positively charged ceria had low lysozyme adsorption in the concentration range $0 < Ceq < 0.3$ mg/mL. Above 0.3 mg lysozyme/mL, the adsorption amount increases rapidly with concentration, reaching a plateau near 100 mg lysozyme/g, and then continuing to increase at concentrations higher than 0.45 mg/mL. The neutral ceria showed the lowest adsorption of lysozyme in the concentration range above 0.3 mg lysozyme/mL. Adsorbed enzyme on this nanomaterial appears to reach a plateau near 0.7 mg lysozyme/mL. Negatively charged ceria nanoparticles always showed higher lysozyme adsorption than the other nanomaterials over the entire concentration range measured. This would be expected based on the strong affinity between a positively charged protein and a negatively charged surface

4.5.2 Protein monolayer adsorption estimates

The Toth and Sips models for heterogeneous adsorption both require a parameter describing the maximum adsorption amount, q_m, (mg/g). While these parameters could have been estimated as part of the fitting exercise, we have chosen to estimate them from the general shape of the molecule, the two ‘limiting’ orientations of lysozyme on a surface (end-on or side-on)(Kubiak and Mulheran 2009) , and the alignment and packing of adsorbed lysozyme molecules in the surface layer.

The two orientations lead to different protein loadings at the same surface packing conditions. There are two ‘limiting’ cases for protein alignment and packing, the jamming limit (a maximum packing for a random sequential adsorption process for irreversible protein placement) and the higher, close-packed limit (a maximum packing for the case in which the protein adsorption is reversible so that molecules can rearrange on the adsorbent).

Lysozyme has the conformation of an ellipsoid with approximate dimensions of 3×3×4.5 nm. Its “end-on” orientation prevails when adsorption occurs from solution at high concentration, whereas a “side-on” orientation monolayer is observed at a low concentration(Andrade 1985). The concentration interval between C_{eq}= 0.1 mg/mL and C_{eq}= 1.0 mg/mL was suggested as the diffuse line between low and high concentration regions when the conformations are considered(Wei, Herron et al. 1990). The concentrations we studied were within this interval. Using the lysozyme dimensions to estimate the circumferential coverage of a 12 nm nanoparticle, we find that ~ 8 side-on oriented or ~13 end-on oriented molecules would be needed (43° or 29° of arc, respectively). It is not clear what conformational changes might be induced in this adsorbed lysozyme, but it has been shown to resist major conformation on adsorption(Robeson and Tilton 1996).

The adsorption of lysozyme (a positively charged protein) on flat silica surfaces (a negatively charged surface) has been studied previously. In the case of lysozyme on silica, it is known that adsorption is slowly reversible and the protein can spontaneously reconfigure from random surface packing toward a close-packed limit for side-on orientation(Robeson and Tilton 1996, Daly, Przybycien et al. 2003). The initial deposition of lysozyme is expected to follow a random sequential adsorption process(Vigil and Ziff 1990, Viot, Tarjus et al. 1992). At low concentrations of adsorbate, the probability of placing a new object is high. At higher coverages, the adsorption probability decreases due to exclusion effects from molecules already adsorbed. At the jamming limit, it is not possible to place an additional object without overlap of the adsorbate molecules, and the probability of adsorption is essentially zero. If the protein molecules can desorb reversibly, then it is possible to approach the maximum packing limit, which corresponds to a highly ordered arrangement of molecules on the surface with minimum void space, such as hexagonal close packing. We have used this prior work to estimate the jamming and closepacked limits for lysozyme adsorbing in either side-on or end-on orientations to 12 nm ceria nanoparticles. Comparison of the limit estimates to the adsorption isotherms provides a basis for deducing the possible lysozyme orientations on the various ceria samples.

Spherical particle estimates.

The interference points between smaller spheres (adsorbate) loading a curved surface occur at $D_{small}/2$ above the adsorbent(L.A. Rosen 1986), thereby increasing the possible packing density above that of a flat surface. In this regard, the estimates for end-on packing are probably reasonable as the ends of the lysozyme ‘ellipse’ are somewhat spheroidal. The upper half of the protein should have little steric interference due to the curvature of the nanoparticle surface. However, packing for the side-on orientation would not be accurately described for an object with an elliptical cross-section. Rather, we modeled this orientation using a spherical particle with the same cross-sectional area as that of the lysozyme ‘ellipse’.

Flat surface estimates.

Two sets of estimates were found for random sequential adsorption of unoriented anisotropic objects onto a flat plane. Both methods took into account particle anisotropy: the aspect ratio was taken as 1 for the end-on orientation and 1.5 for the side-on orientation. The random packing factors for ends-on and sides-on orientation of ellipses(Viot, Tarjus et al. 1992) are 0.548 and 0.58 while the closed-packing factors are 0.907(Pach and Agarwal 1995).

Comparison of protein surface packing limits to data.

The different estimates about monolayer amount adsorption capacity were summarized in Table 4.1. Orientation of lysozyme, different limit (random and maximum) and surface curvature were considered

Table 4.1 Theoretical estimates for q_m, the maximum adsorption capacity (assumed to be monolayer loading).

Orientation	Spherical sorbent packing Monolayer loading (mg/g)		Flat sorbent packing estimate Monolayer loading (mg/g)	
	Random	Maximum	Random	Maximum
Ends-on	195	323	133(1.9 mg/m^2)	217(3.1 mg/m^2)
Sides-en	143	235	91.1(1.3 mg/m^2)	147(2.1 mg/m^2)

Lysozyme loadings reported by Roberson and Tilton (shown in parentheses) have been converted to lysozyme (mg)/ nanoparticle (g) units for comparison with our data.

The monolayer loadings of lysozyme with “end-on” and “side-on” orientations were estimated through the packing factors reported for spherical adsorbates on (larger) spherical adsorbents (L.A. Rosen 1986), ellipses on a plane(Viot, Tarjus et al. 1992, Pach and Agarwal 1995), and rectangles on a plane applied to the data of Robeson and Tilson(Robeson and Tilton 1996). These later two methods gave similar results. As expected, the jamming and maximum packing limits for a spherical adsorbent are higher than for a flat adsorbent for both the side-on and end-on orientations. The dynamic adsorption data (adsorption on flat surfaces at low ionic strength, 0.005 M) of both Daly(Daly, Przybycien et al. 2003) and Robeson(Robeson and Tilton 1996) showed that spontaneous reconfiguration occurred near 1.6-1.7 mg lysozyme/m^2. This is in between the random packing (jamming) limits of the end-on (1.9 mg/m^2) and side-on (1.3 mg/m^2) orientations. Both research teams report similar values for the maximum levels of lysozyme loadings (2.3 mg/m^2 and 2.2 mg/m^2, respectively): these slightly exceed the maximum packing estimate for the side-on orientation (2.1 mg/m^2). The spherical packing estimates for the side-on and end-on orientations can be compared to the adsorption isotherms shown in Figures 4.5 (a) and 4.5 (b). The negatively charged ceria should be electrostatically similar to the flat silica surfaces used by Daly et al. and Robeson and Tilton, i.e., side-on adsorption might be expected. For this surface and Ce > 0.3 mg lysozyme/ml, the protein loadings lie in between the jamming (random alignment) limits for the side-on and end-on orientations. Note that these loading also exceed the maximum packing limits for side-on orientation on flat surfaces. None of the loading values for any isotherm approaches the maximum packing limits for either orientation estimated for a spherical nanoparticle.

Lysozyme adsorption to the neutral ceria has low loading levels throughout the concentration range, and appears to be well below the jamming (random alignment) limit for side-on orientation at the highest values of Ce. Lysozyme adsorption to the positively charged ceria has very low loading levels for values of Ce < 0.25 mg/ml and then increases to a final value greater than the side-on jamming limit for a spherical adsorbent.

4.5.3 Models of the adsorption isotherms

Equations 4.2 and 4.3 require a value for q_m, the maximum amount of adsorbent possible on the nanoparticles. For the negatively .and positively charged ceria nanoparticles, the lysozyme loading approaches the maximum packing end-on limit. For the neutral ceria nanoparticles, the lysozyme loading approaches the jamming side-on limit. Therefore, for modeling purposes, q_m was taken to be 215 mg/g for the negatively and positively charged ceria, and 143 mg/g for the neutral ceria (values shown in Table 4.1).

The isothermal curves and the fitting results by Toth and Sips models were shown in Figures 4.5. Symbols are experimental data and curves are fitted models: (a) Toth (Equation 4.3 a), (b) Sips (Equation 4.3 b). Side-on, random packing limit for spherical adsorbent = dash-dot line. End-on, random packing limit for spherical adsorbent = dashed line. The parameters of the Toth and Sips equations are listed in Table 4.2;

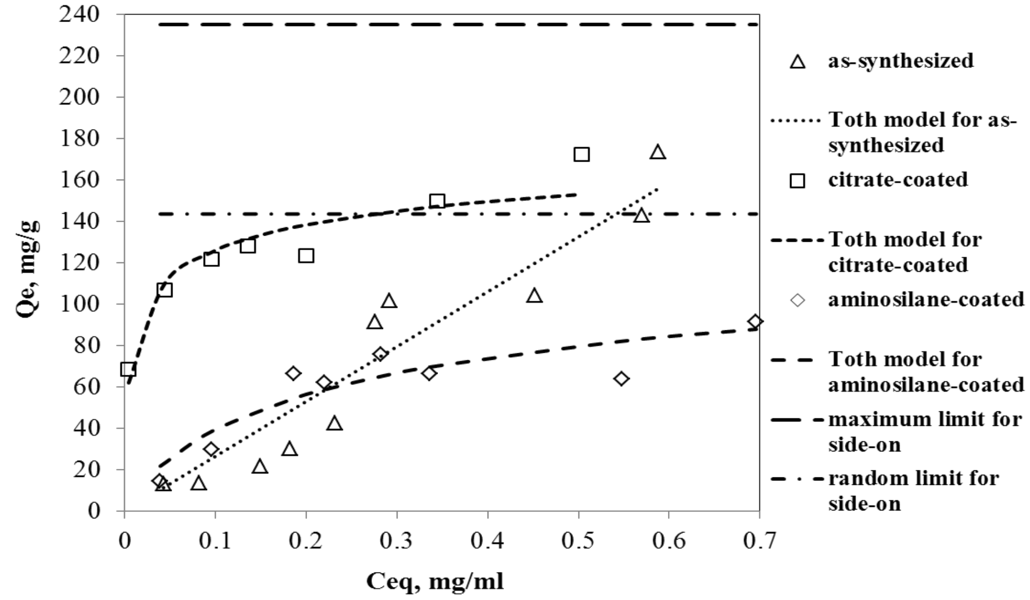

(a)

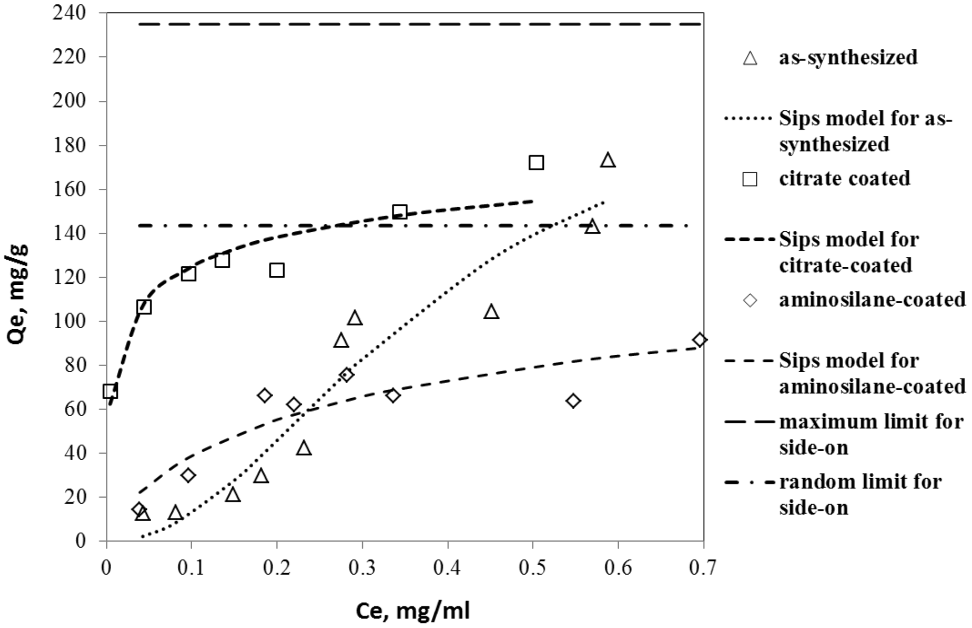

(b)

Figure 4.5 Isothermal adsorption curves of lysozyme on three ceria nanoparticles: (a) fitted by Toth model, (b) fitted by Sips model.

Table 4.2 Parameters for the Toth and Sips models obtained from the fitting process in Figure 4.5.

	Positive ceria	Neutral ceria	Negative ceria
Toth equation, K_T	3419	3.37	11.44
Toth equation, t	39.27	0.64	0.30
Sips equation, K_s	5.5	2.08	2.52
Sips equation, t	1.93	0.75	0.35

The Toth equation fits the isotherms for the negative (citrate-coated) and neutral (aminosilane-coated) ceria well (Fig. 4.5a). The heterogeneity factors, t, of these ceria samples are both less than one. When t is less than 1, the heterogeneity is thought to reflect the surface heterogeneity itself. The K_T for citrate ceria (11.44) is higher than aminosilane-coated ceria (3.37) shows the greater surface heterogeneity on the citrate-coated NP lead to more affinity to lysozyme. On the other hand, the t value for the positively charged ceria is much greater than one, which normally suggests that heterogeneity is due to the adsorbed solute, in this case, the lysozyme. The positively charged ceria data is not particularly well-described by the Toth model, which is essentially linear over this data range, due to the very high value of K_T relative to the solution concentration. The fit quality is fairly insensitive to the K_T value over a wide range, and this data set has a lower R^2 value for the Toth model than the data of the other two ceria samples.

The Sips equation can fit all three ceria very well (Fig.4.5 b); in particular, it appears to provide a better fit to the positively charged ceria. The value t values of citrate-coated

(0.35) and aminosilane-coated ceria (0.75) are still less than one and close to values for Toth equation, suggesting that the heterogeneity in energy site distributions is related to the surface charge and variation in nanoparticle surface morphology. The t value for the positively charged ceria (1.93) is greater than one, suggesting the adsorbed lysozyme influenced the adsorption of other lysozyme molecules. This value of t appears to be consistent with the presence of lowest adsorption amount and then increases rapidly. This lateral effect (positively cooperative effect) was also consistent with energy site distribution analysis that was described below.

4.5.4 Energy site distribution of lysozyme adsorption on ceria NPs

Figure 4.6 shows site energy distributions: (a) for the Toth and (b) for Sips models with C_s=7.09 mg/mL after considering ionic strength (about 3% NaCl) and buffer concentration(0.1M) (Forsythe and Pusey 1996).

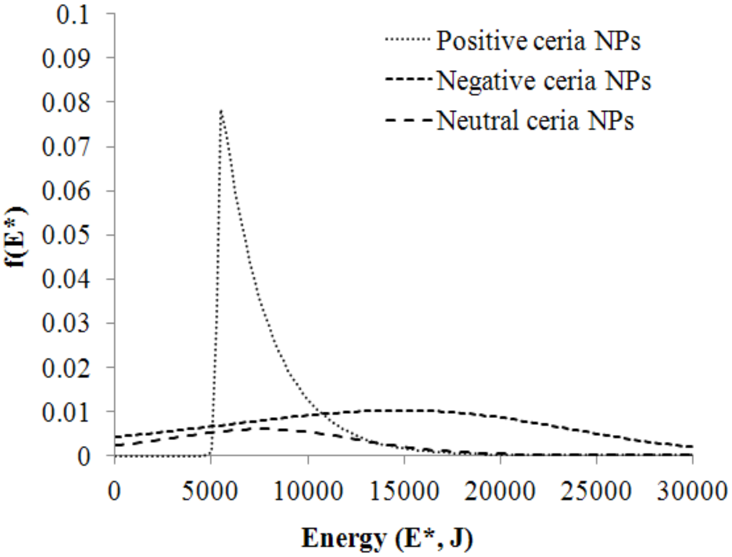

(a)

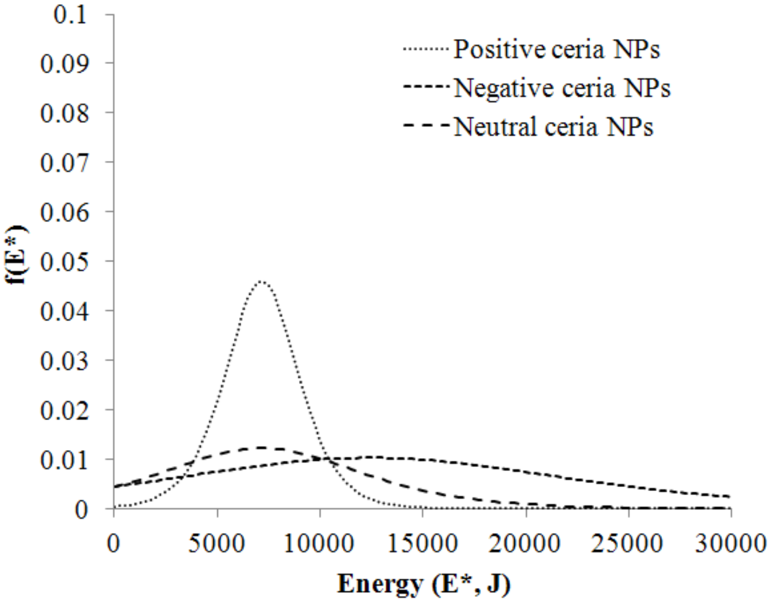

(b)

Figure 4.6 Normalized site energy distribution of lysozyme on different ceria nanoparticles: (a) on Toth parameters and (b) on Sips parameters

The most probable binding energy can be calculated from the zero-point of the derivative of the energy distribution function. The results were Equation 4.12 and 4.13. The most probable binding energy values calculated by parameters were shown in Table 4.3.

$$E^* = RTln(C_s) + \frac{RT}{t} ln(K_T t) \qquad (4.12)$$

$$E^* = RTln(C_s) + \frac{RT}{t} ln(K_s) \qquad (4.13)$$

Table 4.3 Most probable binding energies obtained from Toth and Sips models.

Equation	Positive ceria	Near neutral ceria	Negative ceria
Toth (4.2)	5.5	7.7	14.8
Sips(4.3)	7.2 kJ	7.2 kJ	12.5kJ

For the positively charged ceria, both models have binding energy distributions with a sharp peak at binding energy, 5.5 and 7.2 kJ for the Toth and Sips models, respectively. These values were lower than the peak value of negatively charged surface (14.8 and 12.5 kJ respectively). This is consistent with sorption of a protein with a net positive charge on a positively charged surface. As the lysozyme has a symmetrical distribution of positive charges but an asymmetric distribution of negative charges, there should be fewer sites with a local negative charge that interact with the positive surface(Xie, Zhou et al. 2010). The adsorption behavior, however, also depends on the width of the site energy distribution. The positively charged sample had a t value greater than 1 for both models. It suggests that the heterogeneity is induced by the adsorbate. Both very low and high energy sites were rare on the surface. As the lysozyme molecules should first occupy the binding sites with higher binding energy difference, the positively charged ceria has the initial lowest adsorption amount. Under the influence of the positive cooperative effect, the lysozyme molecules start to occupy the binding sites with average energy so the adsorption amount increases rapidly. The ceria samples with neutral and negatively charged surfaces have t values less than one and broad distributions of binding energies. The negatively charged surfaces had broad binding energy distributions with more high energy sites. The neutral surfaces had broad binding energy distributions but a lower fraction of high energy sites.

4.6 Conclusions

Three 12 nm ceria NPs having different surface charges, negative (citrate-coated), positive (as-synthesized) and neutral (aminosilane-coated) were synthesized. Lysozyme, an enzyme with net positive charge, showed different adsorption to these nanoparticles at pH 4.3. The conformation of lysozyme was stable at this pH. The negatively charged sample had the highest enzyme adsorption, the positively charged sample had a sigmoidal adsorption isotherm, and the near neutral sample had the lowest adsorption levels even at high concentrations of lysozyme in solution. These behaviors are typical of heterogeneous adsorption influenced by the surface charges of nanoparticle, the orientation of protein, and the lateral effect between adsorbed protein molecules. The Langmuir model did not fit the adsorption isotherms, while the Toth and Sips models fit the curves very well. Values of the heterogeneous parameter obtained from these models (t) suggest that surface heterogeneity dominates the adsorption on negatively charged ceria while lateral effects probably affect adsorption on neutral ceria. This effect is consistent with its sigmoidal curve. Site energy distributions were generated from the both models using the condensation approximation method. Negatively charged ceria shows the highest affinity with lysozyme initially since it has the largest binding energy change in the adsorption process. The positively charged ceria shows a narrow site energy distribution, which increased the adsorption rapidly at higher concentration. We anticipate that these methods can be used for a variety of proteins adsorbing to nanoparticle surfaces. However, there are a number of important variables that can affect adsorption; these need to be explored with care.

Chapter 5 Applying accelerator mass spectrometry for low-level detection of complex engineered nanoparticles in biological media

Much of the material in this chapter has been included in the manuscript submitted to Journal of Pharmaceutical and Biomedical Analysis (Wang 2013).

5.1 Highlights

- Citrated-coated nanoalumina was synthesized by hydrothermal reaction under pH control
- Accelerator mass spectrometry was used to analyze ^{26}Al and ^{14}C in dosing material and tissue samples
- ^{26}Al tends to accumulate and persist in liver of dosed rat than in brain and bone
- Citrate coating on nanoalumina entering liver was stable or can be incorporate into nearby tissue so didn't redistribute out of liver.
- Citrate coating on nanoalumina entering other organs dissociate from nanoparticles' surface and enter into metabolic pathway, then redistribute in organs such as the brain and bone.

5.2 Introduction

Complex engineered nanoparticles are being developed for a variety of applications. The core nanoparticles include the metal oxides, such as alumina (Al_2O_3)(Pailleux, Boudard et al. 2013), ceria (CeO_2)(Yokel, Tseng et al. 2013), titania (TiO_2)(Hund-Rinke and Klawonn 2013), zirconia (ZrO_2)(Smits, Liepins et al. 2012), and carbon-based nanomaterials, such as non-functionalized graphene (Chen, Hu et al. 2012), SWCNTs(Jin, Heller et al. 2008), MWCNTs (Chen, Hu et al. 2012). These core materials have extremely low aqueous solubility and therefore persist in biological media with potential to cause delayed toxicity (European Parliament 2006, Ai, Biazar et al. 2011, Zhan, Yanxia et al. 2011, Bimbo, Peltonen et al. 2012). In previous studies, we have found that, in the rat, a single intravenous administration of 30 nm ceria engineered nanoparticles distributed to specific organs within 24 hours; the ceria levels in these organs did not significantly decrease up to 90 days (Yokel, Au et al. 2012). The coating materials, such as organic acids, silane coupling agents, proteins, or polymers, can control the dispersion and agglomeration of nanoparticles in fluids; they can also interact with solids and solutes in organisms and in the environment (Cedervall, Lynch et al. 2007, Lynch and Dawson 2008). Citric acid, a tridentate carboxylic acid, has been widely applied on stabilizing metal oxide nanoparticles(Yokel 2013). The fate of the citrate coating on these nanoparticles was not known. Therefore, the fate and toxicology of CENPs in biological media depends not only on the physico-chemical attributes of the core nanoparticle (size, size distribution, shape), but also their surface-bound molecular coatings. Material balances need to be performed on both the core and coatings materials in order to properly interpret their transport and transformations over the product life cycles.

The common characterization methods for bio-distribution and bio-persistence of CENPs are high-resolution transmission electron microscopy (HR-TEM) (Al Faraj 2010, Dan M 2012) and Inductively coupled plasma mass spectrometry (ICP-MS) (Tsutsumi 2011, Wang 2012). The previous can give good morphology information but difficult to do quantitative analysis. The latter is difficult on tracing the organic components. Some methods based on radioactive isotope have been proposed. Perez et al. (Perez-Campana, Gomez-Vallejo et al. 2013) applied ^{13}N-labeled nanoalumina formed by proton beam activation to show bio-distribution in different organs. It verified the nanoalumina like to accumulate in liver. The method can’t supply distribution information after long time the since the half-life of ^{13}N (9.97 min) is very short. Rojas et al. (Rojas, Gispert et al. 2012) used ^{18}F isotope to label the amino coating on ceria nanoparticles and showed ceria accumulated mainly in lungs, spleen, and liver. However, labeling only the coating or core material is not enough because the coating on surface is likely to dissociate, degrade or transport in biological media. A different isotope tracer may be needed to find and quantity each component of a complex nanoparticle system. Therefore, we proposed to use one isotope tracer for the core material and another for the coating material. Accelerator mass spectrometry (AMS) was used to characterize the two tracers, which can separate rare isotopes with high selectivity and sensitivity, detecting such species at levels 10^3 to 10^9 times lower than other methods (Barker and Garner 1999, Ognibene and Vogel 2004). It seemed possible to use AMS techniques to find and quantity low levels of complex nanoparticle components in biological systems where component transformations might take place. Radioactivity in the dosing material and different tissues can give information about transporting properties of CENPs. Moreover, it should be possible to identify changes in the molar ratio (coating/core) after the CENPs entered biological media and underwent metabolism. This technology will provide an understanding of the potential effects of CNPs from where they go and if they are transformed during these processes.

In this study, the alumina nanoparticles were used as the core material. It is insoluble and common in the environment, therefore it has potential to enter biological tissue and persist there. The nanoalumina was synthesized through hydrothermal reaction and pH control. ^{26}Al isotope was introduced in the synthesis as the core material tracer. There were some hydroxyl groups on the surface of nanoalumina. It can react with citric acid with ^{14}C isotope, used as coating material. The citric acid was bound to the nanoparticle or self-crosslinked on the surface. The CENPs, ^{26}Al-labeled nanoalumina core with ^{14}C-labeled coating, was infused into rats. The dosing material and selected tissues were analyzed by AMS in Purdue Rare Isotope Measurement Laboratory (PRIME lab) to quantify ^{26}Al and ^{14}C.

5.3 Experiments

5.3.1 Synthesis of neat nanoalumina

The synthesis route was modified from Chuah's work(Chuah, Jaenicke et al. 2000). 0.001 mol of anhydrous aluminum chloride ($AlCl_3$, Acros) was dissolved in 10 mL 1M HCl solution to form 0.1 mol/L $AlCl_3$ solution. The anhydrous $AlCl_3$ has a very high tendency to hydrolyze so it was dissolved into acidic solution at a pH of about 2.5 to avoid precipitation. 1mL ^{26}Al-HCl solution (16.5 nCi/mL, provided by the PRIME Lab) was diluted 10-fold. 600μL of the diluted solution with (1 nCi ^{26}Al) was added to the $AlCl_3$ solution. With stirring 0.5 M NaOH solution was added dropwise into the aluminum chloride solution until the pH was 9.5. AlO(OH) and $Al(OH)_3$ are formed in the process (scheme 5.1).

$$AlCl_3 + 3NaOH \rightarrow AlO(OH) + 3NaCl + H_2O$$

$$AlCl_3 + 3NaOH \rightarrow Al(OH)_3 + 3NaCl \qquad \text{Scheme 5.1}$$

The obtained white opaque mixtures were transferred to PTFE containers. The containers were inserted into a metal container (Parr Instrument Company, Models 4746). They were put in a furnace at 190 °C for 24 h, and then cooled to room temperature. The products were washed with distilled water three times and ultracentrifuged to remove the remaining Al^{3+} ion. The solid samples were dried at 90°C for 2 h to remove the adsorbed water and then heated to 600°C for ½ h. The AlO(OH) and $Al(OH)_3$ nanoparticles decomposed to form γ-alumina nanoparticles via calcination (scheme 5.2)(Farag and Endres 2008).

$$2AlO(OH) \rightarrow Al_2O_3 + H_2O$$

$$2Al(OH)_3 \rightarrow Al_2O_3 + 3H_2O \qquad \text{Scheme 5.2}$$

The final samples were named "neat nanoalumina" The weight was 40 mg, 80% of the expected product mass. The expected radioactivity was ^{26}Al 0.02 nCi/mg.

5.3.2 Formation of citrate-coated nanoalumina

For coating nanoalumina with citric acid, 400 mg citric acid (MW=192, citric acid: alumina=10:1 w/w) was dissolved in 4 mL water. 50 μL citric acid with ^{14}C (0.05 mCi/mL, Amersham Bioscience UK limited, CFA263) was diluted into 5 mL with 0.5 μCi/mL. 500 μL of this diluted solution (250 nCi ^{14}C) was added into the citric acid solution. Thermo-gravimetrical analysis showed that the adsorbed citric acid was 0.32% of that added. The adsorbed ^{14}C citric acid should have 0.8 n Ci if the adsorbed/total ratio didn't change. 40 mg of neat nanoalumina was added to the citric acid solution then the mixture was stirred for 24 h. The sample was washed by distilled water, ultracentrifuged and recovered three times to remove the free citric acid, and then was dried at 90°C for 2 h. The dried sample was named "citrate-coated nanoalumina" with an expected radioactivity of 0.02 nCi/mg.

5.3.3 Characterization of nanoaluimina

The shape and morphology of neat nanoalumina were observed by scanning electron microscopy (SEM, Hitachi 4300, University of Kentucky). Quantitation of hydroxyl and citrate groups on the surfaces of neat and citrated-coated nanoalumina was done via thermo gravimetric analysis (TGA) (Perkin Elmer, TGA-7 Thermo gravimetric Analyzer). In a nitrogen environment, the neat and citrate-coated nanoalumina were heated from room temperature to 110°C, kept at 110°C for ½ h to remove physically-adsorbed water then heated to 750 °C at rate of 10°C/min. At higher temperature, the hydroxyl groups will dehydrate to form water and citrate coating will decompose to form carbon dioxide and ethylene(Barbooti and Al-Sammerrai 1986). Some dried alumina-citrate nanoparticles were dispersed in water with ultrasonication, the particle distribution was measured by dynamic light scattering (90 Plus, particle size analyzer, Brookhaven Instrument

Corporation).

5.3.4 Animal infusions

20 mg of the citrate-coated nanoalumina was put into 1 ml water then ultrasonicated; the dispersion was expected to have 0.4 nCi ^{26}Al and 0.4 nCi ^{14}C/ml. One rat was intravenously infused, via a cannula inserted into a femoral vein that terminated in the vena cava, with 0.4 ml of this dispersion (anticipated dose 0.16 nCi ^{26}Al and 0.16 nCi ^{14}C). The dosed animal was terminated 30 days later and tissues, including liver, brain, and bone, were collected. The similar tissues from one undosed animal were collected as the control samples.

5.3.5 Sample preparation for AMS quantification of ^{26}Al

The pathways to analyze ^{26}Al is described in the following paragraphs and summarized in Scheme 5.3.

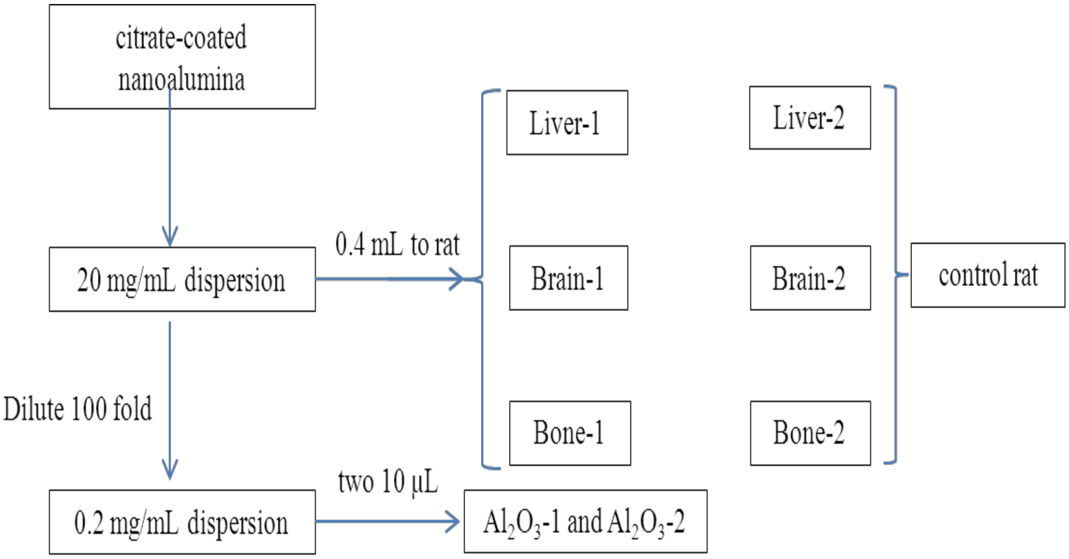

Scheme 5.3 the pathway to analyze ^{26}Al

To quantify ^{26}Al in the dosing material, it was diluted 100-fold to form 0.2 mg/mL dispersion. 400 µL of the commercial analytical standard Al in HCl solution (Aluminum Standard for ICP, 10,000 mg/L in 5% nitric acid, 41377 Fluka) was added to two 10 µL aliquots of the diluted dosing material (Al_2O_3-1 and Al_2O_3-2). This enabled determination of the ^{26}Al/^{27}Al ratio by introducing a known amount of ^{27}Al (4 mg) that greatly exceeded the ^{27}Al in the sample. They were dried and ashed at 1000 °C.

To quantify ^{26}Al in tissue samples, the samples from the dosed and control animals were transferred to a scrupulously cleaned, pre-weighed, 7-ml Teflon screw-cap container and re-weighed to obtain sample weight. Four mg of ^{27}Al from the standard HCl solution was added to each sample. The mixture was dried at 110 °C. 3 ml 2:1 v/v mixture of HNO and H_2O_2 was added to digest the samples. After evaporating the liquid using a heatable, semi-closed system(Yokel and Melograna 1983), the samples (except brain samples) were ashed at 1000 °C. For brain samples, direct ashing will result in some glasslike material believed to be aluminum oxyphosphate. So a procedure that separates Al from phosphate was used (Brauer, Robertson et al. 1999). A diluted mixture of HNO_3 and H_2O_2 was used to solubilize the residue after evaporating the liquid. Two g cation exchange resin containing sulfonic acid functional group (AG 50-X8, 100-200 mesh; Bio-Rad) was used to complex the Al^{3+}. After washing three times with 5 mL 0.2% HNO_3, 5 mL of 1M HF was used to elute Al from the resin. The solution was dried by evaporation then ashed at 1000 °C. The dosing material and tissure samples were sent to the PRIME lab for ^{26}Al quantification by AMS.

5.3.6 Sample preparation for AMS quantification of ^{14}C

The pathways to analyze ^{14}C is described in the following paragraphs and summarized in Scheme 5.4.

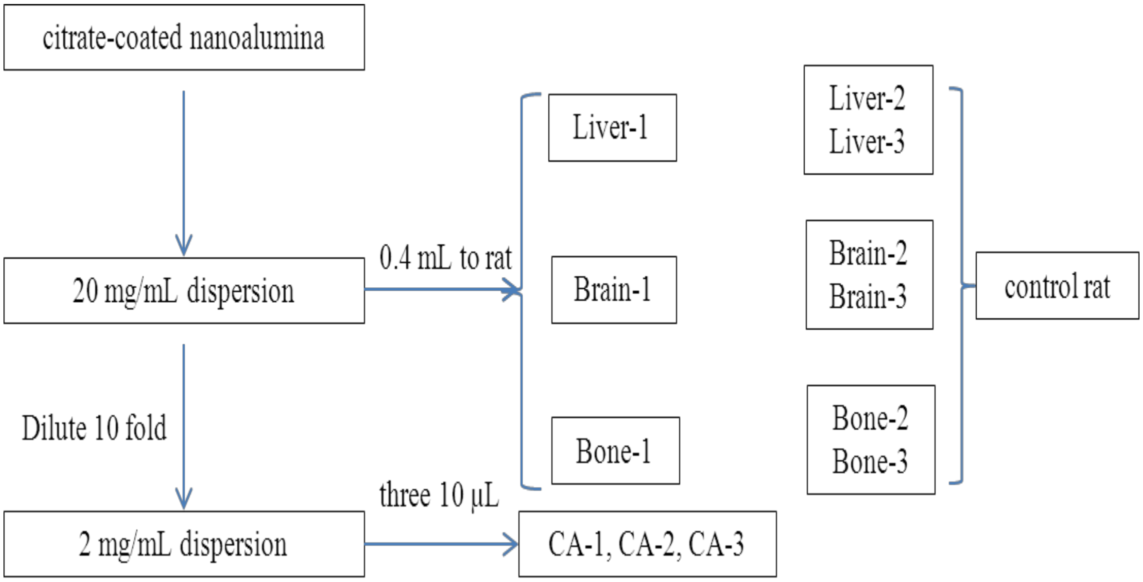

Scheme 5.4 the pathway to analyze ^{26}Al

<u>^{14}C in dosing material samples</u>. To quantify ^{14}C in the dosing material, it was diluted 10-fold to form a 2 mg/mL dispersion. Three 10 µL aliquots of the diluted dispersion were collected (CA-1, CA-2 and CA-3). The CA 1-3 samples were sent to PRIME lab. For the dose material dilutions, tributyrin were added directly to the sample. Tributyrin has no vapor pressure to speak of and is carbon rich. The ^{14}C:^{12}C ratio of the tributyrin is almost exactly 5 x 10^{-14}. The mixture was placed in a small quartz tube that was nestled in a pyrex tube with a glass microfiber filter in the top. The pyrex tube was then placed in a centrifuge tube with another glass microfiber filter in the top. The lid of the centrifuge tube had a few small holes drilled for water vapor removal. This apparatus was then placed in a centrifuge and spun under vacuum for 24 h to remove the water. The sample was then placed in a combustion tube with appropriate reactants, pumped to less than 15 microns as recorded by a gauge on the vacuum line. The tube was sealed with a torch, and placed in an oven to be combusted. The CO_2 was then transferred to another tube and graphitized using the method developed by Ognibene et.al(T.J. Ognibene 2003).

<u>^{14}C in tissue samples</u>. The tributyrin method was good for dosing material, since it had a

very low content of carbon material. There was not enough material for an accurate AMS measurement without addition of a carrier. However, the tissue samples to sufficient carbon content to permit direct measurements of the $^{14}C/^{12}C$ ratio without addition of a carrier. The tissue sample was located in a combustion tube with appropriate reactants, the tube sealed with a torch, and the contents combusted, as above. The CO_2 was then transferred to another tube and graphitized.

5.4 Results and Discussions

5.4.1 Particle size analysis

Figure 5.1 shows the morphology of neat nanoalumina. The top surfaces of most alumina nanoparticles were square. It is not very easy to determine if they were cubic shape or square disks. The typical particle size was 50 nm-80 nm. However, some smaller particles (30 nm) and larger particles (100 nm) existed which may come from sintering and Ostwald ripening in the hydrothermal and calcination processes.

Figure 5.2 shows the volume-averaged particle size distribution of neat and citrate-coated nanoalumina in their dispersion. The dispersion of neat nanoalumina showed three peaks: one centered at 95 nm (65 nm < D < 180 nm); one over the range, 230 nm to 500 nm; and one over the range, 1 μm to 2 μm. The peak centered at 95 nm was consistent with the size observed in SEM. The larger peaks likely represent agglomerates. The dispersion of citrate-coated nanoalumina showed only two peaks: one over the range of 65 nm to 105 nm with a peak at 83 nm and a second over the range, 230 nm to 360 nm. No larger agglomerates were observed. The results shows the citrate coating helped stabilize the nanoparticle dispersion.

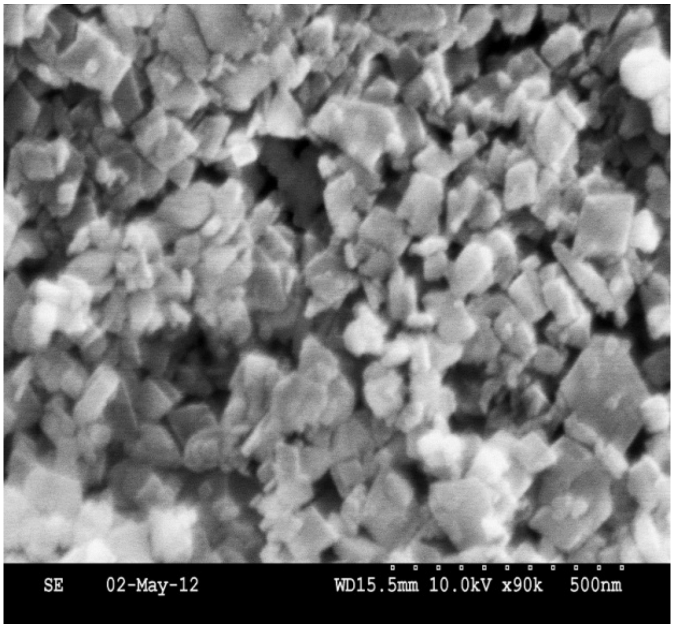

Figure 5.1 Morphology of neat nanoalumina

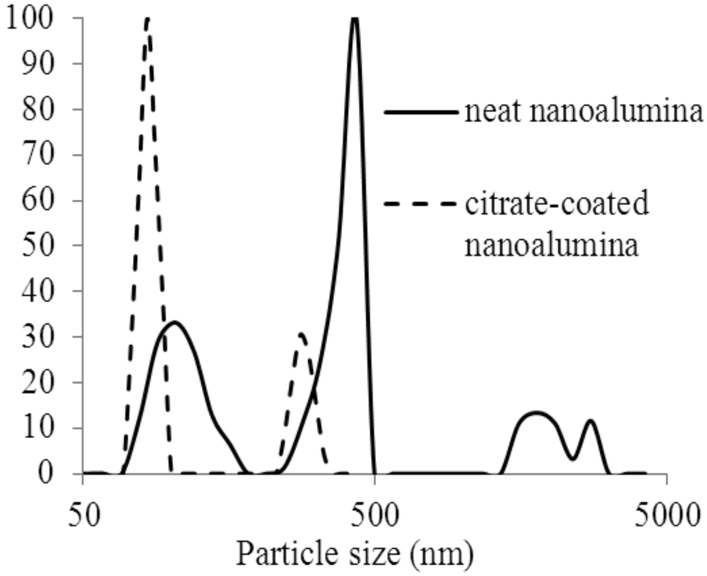

Figure 5.2 Volume-averaged particle size distribution of neat and citrate-coated nanoalumina in their aqueous dispersions.

5.4.2 Thermogravimetric analysis of nanoalumina

Fig 5.3 shows the TGA curves of neat alumina and citrate-coated nanoalumina.

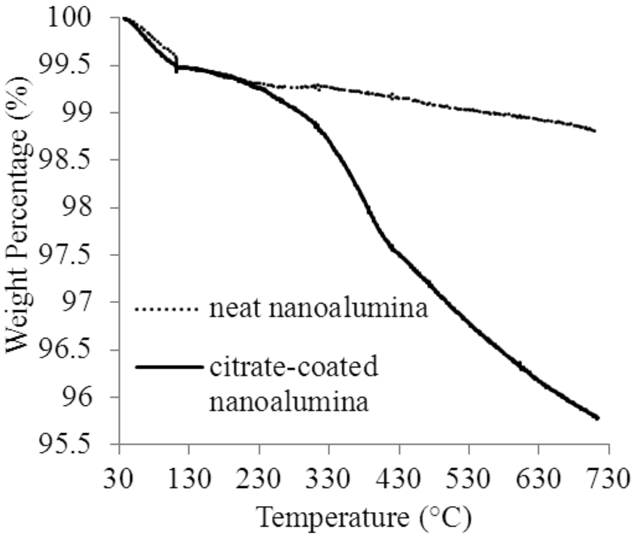

Figure 5.3 Weight loss curves with temperature of neat and citrate-coated nanoalumina

The weight loss of the alumina nanoparticles decreased 0.68% due to the loss of surface hydroxyls. One method has been developed by use to estimate surface density of functional groups. The surface density of hydroxyl groups is 17 /nm^2 based on side length of 60 nm and assuming the shape is cubic. After the alumina was coated with the citrate coating, the weight loss was 3.85%. The 3.2% difference was attributed to decomposition of the citrate coating. The estimated surface density of citric acid is 3.3/nm^2. The hydrodynamic diameter of citric acid is 0.57 nm (van Drunen, Finsy et al. 1993) so the coverage of citrate-coating was estimated to be 77% based on the calculation that we have applied on surface of ceria nanoparticles(Wang 2012).

5.4.3 ^{26}Al in dosing material

Table 5.1 shows the ratio of ^{26}Al/^{27}Al in dosing materials obtained by AMS. The ^{26}Al/^{27}Al ratio in Al_2O_3-1 was 1.41×10^{-9}. The number of ^{26}Al in Al_2O_3-1 was 1.26×10^{11} atoms. The ^{26}Al/^{27}Al ratio in Al_2O_3-2 was 1.20×10^{-9}. It contained 1.07×10^{11} ^{26}Al atoms.

The average number of ^{26}Al atoms in Al_2O_3-1 and Al_2O_3-2 was 1.16×10^{11}. Both of them were 10 µL aliquots of 100-fold diluted dosing material. So the dosing material had average number concentration of 1.16×10^{15} ^{26}Al /ml. The treated rat received 0.4 ml of the dosing material, corresponding to 4.64×10^{14} ^{26}Al atoms or 0.383 nCi. It was 2.4 times the planned dose.

5.4.4 ^{26}Al in tissue samples

Table 5.2 shows the ratio of 26Al/27Al obtained by AMS in tissues from different organs

Liver. The ^{26}Al/ ^{27}Al ratio in liver-1 sample (38.7 mg) was 2.41×10^{-9}. The liver-1 sample contained 2.15×10^{11} ^{26}Al atoms. The liver weight from dosed and control rats was around 16.3 grams so the total liver would contain 9.06×10^{13} ^{26}Al atoms or 7.47×10^{-2} nCi, corresponding to 19.5% of the dose. The ^{26}Al/^{27}Al ratio in liver-2 (35.9 mg) was 7.61×10^{-13}. The liver-2 sample contained 6.78×10^{7} ^{26}Al atoms so the total liver of control rat would contain 3.08×10^{10} ^{26}Al atoms or 2.54×10^{-5} nCi, 3 orders of magnitude less than the liver from the dosed rat. The weight of liver was about 3.2% of the rat's weight and contained 19.5% of dose, showing accumulation of the nanoalumina in the liver.

Brain. The ^{26}Al/^{27}Al ratio in the brain-1 was 5.99×10^{-11}. Brain-1 sample (757.1 mg) contained 5.35×10^{9} ^{26}Al atoms. The average weight of rat's brain is 1.86 gram so the total brain would contain 1.31 ×10^{10} nCi ^{26}Al atoms or 1.08×10^{-5} nCi, about 0.003% of the dosing material. The ^{26}Al/^{27}Al ratio in brain-2 was 5.01×10^{-11}. Brain-2 sample (738 mg) contained 4.47×10^{9} ^{26}Al atoms so the total brain from control rat contained 1.13 ×10^{10} nCi ^{26}Al atoms or 9.27 ×10^{-6} nCi.

The ^{26}Al/^{27}Al background for sample without ^{26}Al was around 10^{-14} in AMS measurements. So the high ^{26}Al/^{27}Al ratio in control rat suggests that some low-level contamination happens in infuse or surgery process. We can't compare the actual difference between the ^{26}Al in livers from dosed and control rats. However, the 0.003%

of dosing material can be considered as the upper limit of ^{26}Al in liver from dosed rats. It indicates only very small amount (if any) of the ^{26}Al got incorporated into the brain since the nanoalumina did not cross the blood-brain barrier to enter brain parenchyma.

Bone. The ^{26}Al/^{27}Al ratio in bone-1 was 4.62×10^{-12}. The bone-1 tissue (52 mg) contained 4.12×10^{8} ^{26}Al atoms. The total rat skeletal weight is about of 5% of body weight (25 gram). So the total skeletal system would contain 1.98×10^{11} ^{26}Al atoms or 1.63×10^{-4} nCi, 0.043% of the dose. The bone-2 (50.8 mg) contained 7.52×10^{8} ^{26}Al atoms, translating to a total rat skeletal content of 3.05×10^{-4} nCi. The control rat bone had higher radioactivity in the bone than the dosed animal. The unexpected result may be from low level contamination on brain as well. The 0.043% of dosing material was used as the upper limit and indicate only small amount (if any) of the ^{26}Al got incorporated into the brain. In the typical mammal, 60% of the body burden of Al is in the skeletal system and only 3% in the liver (Krewski, Yokel et al. 2007). The high concentration of ^{26}Al in liver and low concentration in bone suggests that the ^{26}Al from the nanoalumina is difficult to dissolve and redistributed into bone.

Table 5.1 Ratio of ^{26}Al/^{27}Al obtained by AMS in dosing materials

Dosing material	^{26}Al/^{27}Al	σ on ^{26}Al/^{27}Al	number of ^{27}Al in aliquot	number of ^{26}Al in aliquot	average number in aliquot	number in dosing material	radioactivity in dosing material (nCi)
Al_2O_3-1	1.41E-09	4.20E-11	8.92E+19	1.26E+11	1.16E+11	4.65E+14	3.83E-01
Al_2O_3-2	1.20E-09	3.15E-11	8.92E+19	1.07E+11			

Exact 4 mg of ^{27}Al (8.92E+19 ^{27}Al atoms) was added. The number of ^{26}Al with 1 nCi is 1.21E+15 based on its half-life.

Table 5.2 Ratio of $^{26}Al/^{27}Al$ obtained by AMS in tissues

Tissue samples	sample weight (mg)	$^{26}Al/^{27}Al$	σ on $^{26}Al/^{27}Al$	number of ^{27}Al in sample	number of ^{26}Al in sample	number of ^{26}Al in total organ	radioactivity in total organ (nCi)	fraction in organ
Liver-1	38.7	2.41E-09	5.91E-11	8.92E+19	2.15E+11	9.06E+13	7.47E-02	19.5%
Liver-2	35.9	7.61E-13	4.77E-13	8.92E+19	6.78E+07	3.08E+10	2.54E-05	
Brain-1	757.1	5.99E-11	1.55E-12	8.92E+19	5.35E+09	1.31E+10	1.08E-05	<0.003%
Brain-2	738	5.01E-11	4.65E-12	8.92E+19	4.47E+09	1.13E+10	9.27E-06	
Bone-1	52	4.62E-12	1.66E-13	8.92E+19	4.12E+08	1.98E+11	1.63E-04	<0.043%
Bone-2	50.8	8.44E-12	7.59E-13	8.92E+19	7.52E+08	3.70E+11	3.05E-04	

Two samples of dosed material were tested. For tissue samples, 1=dosed rat, 2= undosed rat. Exact 4 mg of ^{27}Al (8.92E+19 ^{27}Al atoms) was added. The number of ^{26}Al with 1 nCi is 1.21E+15 based on its half-life.

5.4.5 ^{14}C in dosing material

Table 5.3 shows the ratio of $^{14}C/^{12}C$ obtained by AMS and the calculated radioactivity of sample. The $^{14}C/^{12}C$ in CA-1, CA-2, and CA-3 samples was 10353, 9342, 8359, giving an average number of 1.1×10^{9} ^{14}C atoms in the three aliquots. They were 10 μL aliquots of 10-fold diluted dosing material so the dosing material had number concentration of 1.1×10^{12} ^{14}C atoms/mL. The rat got 0.4mL of the dosing material, corresponding to 4.40×10^{11} ^{14}C atoms or 4.56×10^{-2} nCi. It was 28.5% of the planned dose.

5.4.6 ^{14}C in tissue samples

Because ^{14}C is ubiquitous in air, water and food, it inevitably enters the animal to become stored and form the ^{14}C background. The typical ratio $^{14}C/^{12}C$ of mammal's tissue sample via previous AMS measurements is around 1250. It is very closed to value reported in literature(Sabol and Weng 1995). However, the precise ratio in each organ does vary, so we used the ratios in the control rat as our background.

Liver. After subtracting the average $^{14}C/^{12}C$ ratio background (1437.5) from Liver-2 and Liver-3 samples, the actual $^{14}C/^{12}C$ ratio in liver-1 sample was 607.5. The typical carbon percent in liver is 15 wt%. There are 1.23×10^{23} ^{12}C atoms in total liver (16.3 grams). The calculated ^{14}C in total liver of dosed rat is 7.45×10^{10} or 7.72×10^{-3} nCi, 16.9% of the dosage. The ^{14}C of the coating material concentrated in the liver of the dosed rat, but the differences between the dosed rat and the controls was not large as those for the core material, ^{26}Al.

Brain. The $^{14}C/^{12}C$ ratio (1261) from Brain-2 of control rat was used as the background. After subtracting background, the $^{14}C/^{12}C$ in brain-1 sample is 22. The difference is larger than one standard deviation of the measured value so there was some higher amount of ^{14}C in brain of dosed rat than control rat in a statistically significant sense. The typical carbon percent in brain is 15 wt%. There are 1.40×10^{22} ^{12}C atoms in the total brain (1.86 grams). The total brain would contain 3.08×10^{8} ^{14}C atoms or 3.19×10^{-5} nCi, 0.07% of the dosage. For the Brain-3 sample, the $^{14}C/^{12}C$ ratio is much higher than brain-2 sample, even brain-1. The contamination may have come from a previous sample with high ratio of $^{14}C/^{12}C$ that was dried in the vacuum centrifuge.

Bone. After subtracting the average $^{14}C/^{12}C$ ratio background (1412.5) from Bone-2 and Bone-3 samples, the actual ratio of $^{14}C/^{12}C$ in bone-1 sample was 76.5. The typical carbon percent in bone was around 12% (Mehta 2009). There are 1.51×10^{23} ^{12}C atoms in total bone (25 grams). The total bone would contain 1.16×10^{10} ^{14}C atoms or 1.20×10^{-3} nCi, 2.63% of the dosage. The bone from the dosed rat has higher ^{14}C than that from control rats

Table 5.3 Ratio of $^{14}C/^{12}C$ obtained by AMS in dosing materials

number of 14C for 1 nCi	9.65E+12						
14C in 4 mg tributyrin	6.0E+06						
Dosing material	14C/12C (10^{-15})	tributyrin (mg)	12C in tributyrin	14C in aliquot	average 14C in aliquot	14C in dosing material	Radioactivity in dosing material (nCi)
CA-1	10353	3.8	1.14E+20	1.17E+09	1.10E+09	4.40E+11	4.56E-02
CA-2	9342	4	1.20E+20	1.11E+09			
CA-3	8359	4.1	1.23E+20	1.02E+09			

Three samples of dosing material were tested. About 4 mg of tributyrin containing 6.0E+06 14C atoms was added to each sample. The number of ^{14}C atoms with 1 nCi is 9.65E+12 based on its half-life.

Table 5.4 Ratio of $^{14}C/^{12}C$ obtained by AMS in tissues

Tissue samples	$^{14}C/^{12}C$ (10^{-15})	σ on $^{14}C/^{12}C$ (10^{-15})	Actual $^{14}C/^{12}C$ (10^{-15})	organ weight(g)	^{12}C weight in organ(g)	^{12}C Number in total organ	^{14}C number in total organ	radioactivity in total organ (nCi)	fraction in organ
Liver-1	2045	14	607.5	16.3	2.45	1.23E+23	7.45E+10	7.72E-03	16.9%
Liver-2	1454	13							
Liver-3	1419	60							
Brain-1	1283	9	22	1.86	0.28	1.40E+22	3.08E+08	3.19E-05	0.07%
Brain-2	1261	16							
Brain-3	1928	24							

Continue in following page

(Table 5.4, Continued)

Bone-1	1489	14	76.5	25	3.0	1.51E+23	1.16E+10	1.20E-03	2.63%
Bone-2	1411	12							
Bone-3	1414	18							

1=dosed rat, 2 and 3 = undosed rat. The number of 14C atoms with 1 nCi is 9.65E+12 based on its half-life

5.4.7 The ratio of coating:core and material balance

The ratio between ^{14}C/^{26}Al in different organs and the mass distribution are shown in Table 5.5.

Table 5.5 Rare isotopes recovered from tissues

Tissue	^{26}Al	% of ^{26}Al dose	^{14}C	% of ^{14}C dose	^{14}C/^{26}Al, atomic ratio
Dosing material	4.65×10^{14}	100%	4.4×10^{11}	100%	9.46×10^{-4}
Liver	9.06×10^{13}	19.5%	7.45×10^{10}	16.9%	8.22×10^{-4}
Brain	1.31×10^{10}	<0.003%	3.08×10^{8}	0.07%	$>2.35\times10^{-2}$
Bone	1.98×10^{11}	<0.043%	1.16×10^{10}	2.63%	$>5.86\times10^{-2}$
Total		19.5%		19.6%	

The ratio between ^{14}C/^{26}Al in different organs and the mass distribution are shown in Tables 3. In the dosing material, the average numbers of ^{26}Al and ^{14}C atoms were 4.65×10^{14} and 4.40×10^{11} respectively. The ^{14}C/^{26}Al was 9.46×10^{-4}. The total recovered ^{26}Al and ^{14}C from liver, brain and bone are 19.5% and 19.6% of the dosing material respectively.

The numbers of isotope atoms in the dosed liver were: ^{26}Al = 9.06×10^{13} and ^{14}C = 7.45×10^{10}. The ^{14}C/^{26}Al in liver of dosed rat was 8.22×10^{-4}, around 87% of the ratio in dosing material. The citrated coating entering liver (19.5% of dosage) partially dissociated from the nanoalumina, and would have been available to redistribute into organs such as the brain and bone.

The average numbers of isotope atoms in brain were: ^{26}Al $<1.31\times10^{10}$ and ^{14}C = 3.08×10^{8}, for a ^{14}C/^{26}Al ratio $> 2.35\times10^{-2}$. The average numbers of isotope atoms in bone were: ^{26}Al $<1.98\times10^{11}$ and ^{14}C = 1.16×10^{10}, for a ^{14}C/^{26}Al calculated ratio $> 5.81\times10^{-2}$. Both of these ratios are much higher than that of the dosing material. The reason is that ^{14}C preferentially accumulated in brain (0.07%) and bone (2.63%) compared to the levels of ^{26}Al in these two organs (0.003% and 0.043%, respectively). This finding suggests that some of the citrate coating dissociated from the nanoalumina's surface and then redistributed to organs such as the brain and bone.

5.5 Conclusions

The core and surface coatings of a complex engineered nanoparticle have been tracked during biological exposure to the rat using rare isotope labels detected by AMS. The alumina core was tracked using ^{26}Al and the citrate coating was tracked using ^{14}C. Comparison of the rare isotope levels and their ratios, $^{14}C/^{26}Al$, in different organs demonstrated the relative stability of the two CENP components. The amount of ^{26}Al in the liver of the dosed rat was higher than that of control rats. The amounts of ^{26}Al in brain and bone of the dosed rat were similar to those of the control rat. It suggests the nanoalumina accumulated, and persisted in the liver 30 days after infusion. The amounts of ^{14}C in the liver, bone, and brain of the dosed rat were also higher than those of the control rats. However, the $^{14}C/^{26}Al$ ratios differed between liver, brain, and bone. Slightly less coating material went to the liver compared to the core material and its levels were significantly higher in brain and bone compared to the core material. Some of the citrate coating dissociated from the nanoparticle surfaces and redistributed to organs such as the brain and bone. AMS methodology provides a new opportunity to characterize the biodistributions of complex engineered nanoparticles.

Chapter 6 Summary and future research

6.1 Surface modification of graphite and silicon carbide nanoparticles and it effect on properties of their dispersions

The project supported by Valvoline, ASHLAND InC., (along with U.S. Army TARDEC division) was for developing heat transfer fluid used under specific environment. Chemical surface modification was proposed to give the improved and balanced properties of graphite and SiC dispersions. One new and environmentally-friendly method was developed to convert the surface of graphite and SiC to hydrophobic surface. The thermogravimetric analysis (TGA) method was extended to estimate the original surface density of hydroxyl groups. SiC was found to have enough hydroxyl groups therefore direct silanization was used to create alkane chain. The graphite was verified to be short of reactive groups on surface so citric acid was used to generate hydroxyl surface groups firstly.

The surface modification was verified to offset the formation of agglomerates in their dispersion. It leads the non-linear enhancement on thermal conductivity. One combined model, consider the shape factor of agglomerates, was built to fit and interpret the interesting results. The results suggest the enhancement on thermal conductivity related to shape of agglomerates more closely than primary shape. The dispersion of surface-modified graphite has lower thermal enhancement than those of neat graphite, while the dispersion of complex SiC has higher thermal conductivity than those of neat SiC dispersion. The competitive effect between Brownian motion and nanocluster mechanisms was also discussed. The less agglomerates brought by surface modification also influence the rheological behavior. The dispersions with surface-modified nanoparticles became more Newtonian, lower viscosity at higher volume fraction, more practical for practical application. It has good potential application for nanofluids used under conditions with intense change of shear force.

The result supplied more understanding to influence of surface modification on the thermal and rheological properties of dispersions with nanoparticles. However, more experiment data need to fit the model better and give more exact value for shape factor, maximum volume fraction and intrinsic viscosity. The physical meanings of these fitting parameters need to be given detailed study.

6.2 Nanoparticle segregation in ultrathin films: surface chemistry effects

The project supported by Optical Dynamics, division of Vision Dynamics was for developing bi-layer optical thin film by self-assembly separation of nanoparticles. There are always some hydroxyl groups on the surfaces of silica and titania nanoparticles. Silanization reaction was used to transform relatively hydrophilic surfaces of silica and titania nanoparticles to hydrophobic surface via attaching alkane chains. Thermo gravimetric analysis (TGA) was developed to analyze the original surface density of hydroxyl groups and their conversion percentage to alkane chains. The neat nanoparticles has tendency to remain in monomer while alkane-grafted nanoparticles settle down easily. They are capable to segregate assembly to form bi-layer structure self-assembly in single deposition process. The Energy-dispersive X-ray spectroscopy (EDS) verifies that the bi-layer structure has been successfully obtained. It has good potential application for create multi-layered antireflectane or high reflectance optical thin film.

To verify and quantification of reasons behind self-assembly separation is on future work. The difference on agglomerates size, which has been discussed, is one reason for the self-assembly separation in one deposition. The other reason may be the interfacial tension between nanoparticles, monomer and solvents. The hydrophilic monomer should have better wettability on neat nanoparticle (hydrophilic) than surface-modified nanoparticles (hydrophobic). It offset the settling tendency of agglomerates. However, there was still no ideal measurement on interfacial tension between nanoparticles and continuous phase.

6.3 Influence of surface charge on lysozyme adsorption to ceria nanoparticles

This project supported by United States Environmental Protection Agency was for investigated the interaction between nanoparticles and biomacromolecules. Three 12 nm ceria NPs having different surface charges, negative (citrate-coated), positive (as-synthesized) and near-neutral (aminosilane-coated) were synthesized. Lysozyme, an enzyme with net positive charge, showed different adsorption behaviors to these three nanoparticles. The highest enzyme adsorption was observed on the negatively charged surface, the positively charged sample had a sigmoidal adsorption isotherm, and the near neutral sample had the lowest adsorption levels even at high concentrations of lysozyme in solution.

These behaviors are typical of heterogeneous adsorption influenced by the surface charges of nanoparticle, the orientation of protein, and the lateral effect between adsorbed protein molecules. The Langmuir model did not fit the adsorption isotherms, while the Toth and Sips models fit the curves very well. Values of the heterogeneous parameter obtained from these models (t) suggest that surface heterogeneity dominates the adsorption on negatively charged ceria while lateral effects probably affect adsorption on positively charged ceria. This effect is consistent with its sigmoidal curve.

Site energy distributions were generated from the both models using the condensation approximation methods. Negatively charged ceria shows the highest affinity with lysozyme initially since it has the largest binding energy change in the adsorption process. The positively charged ceria shows a narrow site energy distribution, which increased the adsorption rapidly at higher concentration. We anticipate that these methods can be used for a variety of proteins adsorbing to nanoparticle surfaces.

In the study, the monolayer estimation on jamming and maximum limit was crucial on both fitting process for adsorption isothermal curves and calculation of local site energy distributions. The value depends on orientation of protein and surface curvature of nanoparticles. Only theoretical estimation is not enough for future study. An exact measurement to orientation of adsorbed proteins and monolayer coverage amount need development.

6.4 Applying accelerator mass spectrometry for low-level detection of complex engineered nanoparticles in biological media

This project was supported by National Science Foundation to low-level detection of complex nanomaterials in biological media. The core and surface coatings of a complex engineered nanoparticle have been tracked during biological exposure to the rat using rare isotope labels detected by AMS. The alumina core was tracked using ^{26}Al and the citrate coating was tracked using ^{14}C. Comparison of the rare isotope levels and their ratios, ^{14}C/^{26}Al, in different organs demonstrated the relative stability of the two CENP components. The amount of ^{26}Al in the liver of the dosed rat was higher than that of control rats. The amounts of ^{26}Al in brain and bone of the dosed rat were similar to those of the control rat. It suggests the nanoalumina accumulated, and persisted in the liver 30 days after infusion.

The amounts of ^{14}C in the liver, bone, and brain of the dosed rat were also higher than those of the control rats. However, the ^{14}C/^{26}Al ratios differed between liver, brain, and bone. Slightly less coating material went to the liver compared to the core material and its levels were significantly higher in brain and bone compared to the core material. Some of

the citrate coating dissociated from the nanoparticle surfaces and redistributed to organs such as the brain and bone. AMS methodology provides a new opportunity to characterize the biodistribution of complex engineered nanoparticles.

Bibliography

A.J.Moses (1978). The practicing scientist's handbook: a guid for physical and terrestrial scientists and engineers, Van Nostrand Reinhold Co.

Ai, J., E. Biazar, M. Jafarpour, M. Montazeri, A. Majdi, S. Aminifard, M. Zafari, H. R. Akbari and H. G. Rad (2011). "Nanotoxicology and nanoparticle safety in biomedical designs." Int. J. Nanomed. **6**: 1117-1127.

Al-Muhtaseb, S. A. and J. A. RItter (1999). "Roles of Surface Heterogeneity and Lateral Interactions on the Isosteric Heat of Adsorption and Adsorbed Phase Heat Capacity." Journal of Physical Chemistry B **103**(13): 2467-2479.

Al Faraj, A. B., Amine; Cieslar, Katarzyna; Lacroix, Ghislaine; Canet-Soulas, Emmanuelle; Cremillieux, Yannick (2010). "Long-term follow-up of lung biodistribution and effect of instilled SWCNTs using multiscale imaging techniques." nanotechnology **21**(17): 175103/175101-175103/175109.

Alekseev, S. A., V. N. Zaitsev, J. Botsoa and D. Barbier (2007). "Fourier Transform Infrared Spectroscopy and Temperature-Programmed Desorption Mass Spectrometry Study of Surface Chemistry of Porous 6H-SiC." Chemistry of Materials **19**(9): 2189-2194.

Allen CG, B. D., Albin JM, Oertli HE, Gillaspie DT, Olson DC, Furtak TE, Collins RT (2008). "Surface modification of ZnO using triethoxysilane-based molecules." Langmuir **24**(23): 13393-13398.

An, X. and H. Zeng (2003). "Functionalization of carbon nanobeads and their use as metal ion adsorbents." Carbon **41**(15): 2889-2896.

Andrade, J. D. (1985). New York, Plenum Press.

Anoop, K. B., S. Kabelac, T. Sundararajan and S. K. Das (2009). "rheological and flow characteristics of nanofluids: Influence of electroviscous effect and particle agglomeration." Journal of applied physics **106**: 034909/034901-034909/034907.

Assael, M. J., C. F. Chen, I. Metaxa and W. A. Wakeham (2004). "Thermal Conductivity of Suspensions of Carbon Nanotubes in Water." International Journal of Thermophysics **25**(4): 971-985.

Asthagiri, D. and A. M. Lenhoff (1997). "Influence of Structural Details in Modeling Electrostatically Driven Protein Adsorption." Langmuir **13**(25): 6761-6768.

Barbooti, M. M. and D. A. Al-Sammerrai (1986). "Thermal decomposition of citric acid."

Thermochimica Acta **98**: 119-126.

Barker, J. and R. C. Garner (1999). "Biomedical applications of accelerator mass spectrometry-isotope measurements at the level of the atom." Rapid Commun Mass Spectrom **13**(4): 285-293.

Barton, S. S. and B. H. Harrison (1975). "Acidic surface oxide structures on carbon and graphite. I." Carbon **13**(4): 283-288.

Beck, C., W. Hartl and R. Hempelmann (1999). "Covalent surface functionalization and self-organization of silica nanoparticles." Angewandte Chemie, International Edition **38**(9): 1297-1300.

Berber, S., Y.-K. Kwon and D. Tomanek (2000). "Unusually High Thermal Conductivity of Carbon Nanotubes." Physical Review Letters **84**(20): 4613-4616.

Bimbo, L. M., L. Peltonen, J. Hirvonen and H. A. Santos (2012). "Toxicological profile of therapeutic nanodelivery systems." Curr. Drug Metab. **13**(8): 1068-1086.

Bonincontro, A., A. De Francesco, M. Matzeu, G. Onori and A. Santucci (1997). "Conformational changes of lysozyme in water-ethanol mixtures." Colloids Surf., B **10**(2): 105-111.

Bradford, M. M. (1976). "A rapid and sensitive method for the quantitation of microgram quantities of protein utilizing the principle of protein-dye binding." Anal Biochem **72**: 248-254.

Brauer, R. D., J. D. Robertson, P. Sharma and R. A. Yokel (1999). "Aluminum and phosphorus separation: application to preparation of target from brain tissue for 26Al determination by accelerator mass spectrometry." Nucl. Instrum. Methods Phys. Res., Sect. B **152**(1): 129-134.

Brinley, E., S. Seal, R. Folks, E. Braunstein and L. Kramer (2006). "High efficiency SiO2–TiO2 hybrid sol-gel antireflective coating for infrared applications " Journal of Vacuum Science & Technology A: Vacuum, Surfaces, and Films **24**(4): 1141-1146.

Burton, W. G., K. D. Nugent, T. K. Slattery, B. R. Summers and L. R. Snyder (1988). "Separation of proteins by reversed-phase high-performance liquid chromatography. I. Optimizing the column." J. Chromatogr. **443**: 363-379.

Calleja, W., C. Falcony, A. Torres, M. Aceves and R. Osorio (1995). "Optical properties of non-stoichiometric SiO2 as a function of excess silicon content and thermal treatments." Thin Solid Films **270**(1-2): 114-117.

Cao, G. (2004). Nanostructures & Nanomaterials: Synthesis, Properties & Applications.

London, Imperial College Press.

Caracciolo, G. (2011). "Factors Determining the Superior Performance of Lipid/DNA/Protammine Nanoparticles over Lipoplexes." Journal of medical chemistry **54**(12): 4160-4171.

Carmo, N. L. D. F. a. D. R. d. (2001). Adsorption at Silica, Alumina, and Related surface. Encyclopedia of surface and colloid science. P. Somasundaran, Taylor & Francis Group. **1:** 214.

Carter, M. C. (1995). "Site Energy Distribution Analysis of Preloaded Adsorbents." Environmental Science Technology **29**: 1773-1780.

Cedervall, T., I. Lynch, S. Lindman, T. Berggard, E. Thulin, H. Nilsson, K. A. Dawson and S. Linse (2007). "Understanding the nanoparticle-protein corona using methods to quantify exchange rates and affinities of proteins for nanoparticles." Proc. Natl. Acad. Sci. U. S. A. **104**(7): 2050-2055.

Cerofolini, G. F. (1974). " Localized Adsorption on Heterogeneous Surfaces." Thin Solid Films **23**: 129-152.

Chang, H. and C. S. Jwo (2005). "Rheology of CuO nanoparticle suspension." Reviews on Advanced Material Science **10**: 128-132.

Che, J., X. Wang, Y. Xiao, X. Wu, L. Zhou and W. Yuan (2007). "Effect of inorganic-organic composite coating on the dispersion of silicon carbide nanoparticles in non-aqueous medium." Nanotechnology **18**(13): 135706/135701-135706/135706.

Chee Kok Poh, S. H. L., Hui Pan, Jianyi Lin, Jim Yang Lee (2008). "Citric acid functionalized carbon materials for fuel cell applications." Journal of power sources **176**(1): 70-75.

Chen, H., Y. Ding and C. Tan (2007). "Rheological behaviour of nanofluids." New J. Phys **9**.

Chen, L. Q., P. P. Hu, L. Zhang, S. Z. Huang, L. F. Luo and C. Z. Huang (2012). "Toxicity of graphene oxide and multi-walled carbon nanotubes against human cells and zebrafish." Sci. China Chem. **55**(10): 2209-2216.

Chercoles, A. R., A. M. M. San, l. R. J. M. de and M. Gomez (2009). "Analytical characterization of polymers used in conservation and restoration by ATR-FTIR spectroscopy." Anal Bioanal Chem **395**(7): 2081-2096.

Chevalier, Y. D.-C., M. -C.; Durand, J. -P.; Delfort, B.; Gateau, P.; Barré, L.; Frot, D.; Briolant, Y.; Blanchard, I.; Gallo, R. (2001). Adsorption of poly(isobutenylsuccinimide) dispersants at a solid-hydrocarbon interface. Trends in Colloid and Interface Science XV. P. P. G. Koutsoukos.

Choi, S. U. S., Z. G. Zhang, W. Yu, F. E. Lockwood and E. A. Grulke (2001). "Anomalous thermal conductivity enhancement in nanotube suspensions." Applied Physics Letters **79**(14): 2252-2254.

Chon, C. H., K. D. Kihm, S. P. Lee and S. U. S. Choi (2005). "Empirical correlation finding the role of temperature and particle size for nanofluid (AlO3) thermal conductivity enhancement." Appl. Phys. Lett. **87**: 153107/153101-153107/153103.

Chuah, G. K., S. Jaenicke and T. H. Xu (2000). "The effect of digestion on the surface area and porosity of alumina." Microporous Mesoporous Mater. **37**(3): 345-353.

Daly, S. M., T. M. Przybycien and R. D. Tilton (2003). "Coverage-Dependent Orientation of Lysozyme Adsorbed on Silica." Langmuir **19**(Copyright (C) 2011 American Chemical Society (ACS). All Rights Reserved.): 3848-3857.

Dan M, T. M., Wu P, Unrine JM, Grulke EA, Yokel RA. (2012). "Brain microvascular endothelial cell association and distribution of a 5 nm ceria engineered nanomaterial." Int J Nanomedicine **7**: 4023-4036.

Daniel Bonduel, M. M., Michaël Alexandre, Fabien Monteverde and Philippe Dubois. (2005). "Supported coordination polymerization: a unique way to potent polyolefin carbon nanotube nanocomposites." Chem. Commun.: 781-783.

Das, S. K., N. Putra and W. Roetzel (2003). "Pool boiling characteristics of nano-fluids." International Journal of Heat and Mass Transfer **46**(5): 851-862.

Davis, M. E., Z. Chen and D. M. Shin (2008). "Nanoparticle therapeutics: an emerging treatment modality for cancer." Nat. Rev. Drug Discovery **7**: 771-782.

De, M., S. Rana, H. Akpinar, O. R. Miranda, R. R. Arvizo, U. H. F. Bunz and V. M. Rotello (2009). "Sensing of proteins in human serum using conjugates of nanoparticles and green fluorescent protein." Nat. Chem **1**: 461-465.

Deiss, J. L., P. Anizan, S. El Hadigui and C. Wecker (1996). "Steric stability of TiO2 nanoparticles in aqueous dispersions." Colloids and Surfaces, A Physicochemical and Engineering Aspects **106**(1): 59-62.

Delhaes, P. (2000). Graphite and Precursors, CRC Press.

Ding, Y., H. Alias, D. Wen and R. A. Williams (2006). "Heat transfer of aqueous suspensions of carbon nanotubes (CNT nanofluids)." International Journal of Heat and Mass Transfer **49**(1-2): 240-250.

Druffel, T., K. Geng and E. Grulke (2006). "Mechanical comparison of a polymer nanocomposite to a ceramic thin film anti-reflective filter." Nanotechnology **17**.

Eastman, J. A., S. R. Phillpot, S. U. S. Choi and P. Keblinski (2004). "Thermal transport in nanofluids." Annual Review of Materials Research **34**: 219-246.

Ermakova, E. (2005). "Lysozyme dimerization: Brownian dynamics simulation." J. Mol. Model. **12**(Copyright (C) 2011 American Chemical Society (ACS). All Rights Reserved.): 34-41.

European Parliament, P. D. E. a. S. P. (2006). Nanomaterials in consumer products, Availability on the European market and adequacy of the regulatory framework.

Eva M. Wong, P. G. H., Cindy J. Liang, Bai-Ming Shi, Gerald J. Meyer, and Peter C. Searson (2001). "Influence of Organic Capping Ligands on the Growth Kinetics of ZnO Nanoparticles." Langmuir **17**(26): 8362-8367.

Farag, H. K. and F. Endres (2008). "Studies on the synthesis of nano-alumina in air and water stable ionic liquids." J. Mater. Chem. **18**(4): 442-449.

Fischer, N. O., C. M. McIntosh, J. M. Simard and V. M. Rotello (2002). Proc. Natl. Acad. Sci. **99**.

Forsythe, E. L. and M. L. Pusey (1996). "The effects of acetate buffer concentration on lysozyme solubility." Journal of Crystal Growth **168**: 112-117.

Fumihide Shiraishi1, M. U., Rumi Chand1, Yuichiro Shibata, Hom Nath Luitel (2013). "Effect of silanization of titanium dioxide on photocatalytic decomposition of 2,4-dinitropheonol under irradiation with artificial UV light and sunlight." J. Chem. Technol. Biotechnol.

G.I. Titelman, V. Gelman, S. Bron, R.L. Khalfin, Y. Cohen and H. Bianco-Peled (2005). "Characteristics and microstructure of aqueous colloidal dispersions of graphite oxide." Carbon **43**(3): 641-649.

Galoppini, E. (2004). "Linkers For Anchoring Sensitizers To Semiconductor Nanoparticles." Coord. Chem. Rev **248**: 1283-1297.

Garboczi, E. J., K. A. Snyder, J. F. Douglas and M. F. Thorpe (1995). "Geometrical percolation threshold of overlapping ellipsoids." Physical Review E Statistical Physics, Plasmas, Fluids, and Related Interdisciplinary Topics **52**(1-B): 819-828.

Garcia-Gonzalez, C. A., J. Fraile, A. Lopez-Periago and C. Domingo (2009). "Preparation of silane-coated TiO2 nanoparticles in supercritical CO2." Journal of Colloid and Interface Science **338**(2): 491-499.

George, O. S. a. S. M. (1995). "Thermal Stability of Hydroxyl Groups on a Well-Defined Silica Surface " Journal of Physical Chemistry **99**: 9.

Gillich, T., C. Acikgöz, I. L, S. AD, S. ND and T. M (2013). "PEG-stabilized core-shell nanoparticles: impact of linear versus dendritic polymer shell architecture on colloidal properties and the reversibility of temperature-induced aggregation." ACS Nano **7**(1): 316-329.

Glocker, D. A. (1995). Handbook of Thin Film Process Technology. Bristol, IOP.

Gokel, G. W. (2006). Dean's Handbook of Organic Chemistry, Mcgraw-Hill.

Gu, J., Q. Zhang, J. Dang, J. Zhang and S. Chen (2009). "Preparation and mechanical properties researches of silane coupling reagent modified beta -silicon carbide filled epoxy composites." Polymer Bulletin (Heidelberg, Germany) **62**(5): 689-697.

H.A.Macleod (2001). Thin-Film Optical Filters. Philadelphia, PA, Institute of Physics Publishing.

H.Masuda and A. Ebata (1993). "Alteration of thermal condutivities and viscosities of liquids by dispersing ultra-fine particles." Netsu Bussei **7**: 227-233.

Hardas, S. S., D. A. Butterfield, R. Sultana, M. T. Tseng, M. Dan, R. L. Florence, J. M. Unrine, U. M. Graham, P. Wu, E. A. Grulke and R. A. Yokel (2010). "Brain distribution and toxicological evaluation of a systemically delivered engineered nanoscale ceria." Toxicol. Sci. **116**(2): 562-576.

Harris, G. L. (1995). Properties of silicon carbide. London, IEE INSPEC.

Heine, D. R., M. K. Petersen and G. S. Grest (2010). "Effect of particle shape and charge on bulk rheology of nanoparticle suspensions." Journal of Chemical Physics **132**: 184509/184501-184509/184506.

Hilding, J., E. A. Grulke, Z. G. Zhang and F. Lockwood (2003). "Dispersion of carbon nanotubes in liquids." Journal of Dispersion Science and Technology **24**(1): 1-41.

Hoecke, K. V. (2009). "Fate and Effects of CeO2 Nanoparticles in Aquatic Ecotoxicity Tests." Environ. Sci. Technol **43**: 4537-4546.

Horacio E. Bergna, W. O. R., Ed. (2006). Colloidal silica: fundamentals and applications. Surfactant Science Series, CRC Press, Taylor & Francis Group.

Huesing, N., U. Schubert, B. Riegel and W. Kiefer (1996). "Chemical functionalization of silica aerogels." Materials Research Society Symposium Proceedings **435**(Better Ceramics through Chemistry VII: Organic/Inorganic Hybrid Materials): 339-344.

Hund-Rinke, K. and T. Klawonn (2013). Investigation of widely used nanomaterials (TiO2, Ag) and gold nanoparticles in standardised ecotoxicological tests, Fraunhofer Institute for Molecular Biology and Applied Ecology IME, Schmallenberg, Germany.**:** F/1-F/3, i-xxv, 1-431.

Iwasawa, Y., Ed. (1986). Tailored metal catalysts, D. Reidel Publishing Company.

Jang, S. P. and S. U. S. Choi (2004). "Role of Brownian motion in the enhanced thermal conductivity of nanofluids." Applied Physics Letters **84**: 4316-4318.

Jin, H., D. A. Heller and M. S. Strano (2008). "Single-Particle Tracking of Endocytosis and Exocytosis of Single-Walled Carbon Nanotubes in NIH-3T3 Cells." Nano Lett. **8**(6): 1577-1585.

Jwo, C. S., T. P. Teng, C. J. Hung and Y. T. Guo (2005). "Research and development of measurement device for thermal conductivity of nanofluids." Journal of Physics Conference Series **13**: 55-58.

K. Sefiane, J. S., and J. MacGillivray (2008). "Contact line motion and dynamic wetting of nanofluid solutions." Advances in Colloid and Interface Science **138**(2): 101-120.

K.Gupta, R. (2000). Polymer and Composite Rheology. New York, Marcel Dekker Inc.

Kats, M. A., R. Blanchard, P. Genevet and F. Capasso (2013). "Nanometre optical coatings based on strong interference effects in highly absorbing media." Nat. Mater. **12**(1): 20-24.

Keblinski, P. and S. R. Phillpot (2001). "Mechanisms of heat flow in suspensions of nano-sized particles." International Journal of Heat and Mass Transfer **45**: 855-863.

Keblinski, P., S. R. Phillpot, S. U. S. Choi and J. A. Eastman (2002). "Mechanisms of heat flow in suspensions of nano-sized particles (nanofluids)." International Journal of Heat and Mass Transfer **45**: 855-863.

Kim, P., L. Shi, A. Majumdar and P. L. McEuen (2001). "Thermal Transport Measurements of Individual Multiwalled Nanotubes." Physical Review Letters **87**(21): 215502/215501-215502/215504.

Kim, S. H., S. R. Choi and D. Kim (2007). "Thermal Conductivity of Metal-Oxide Nanofluids: Particle Size Dependence and Effect of Laser Irradiation." ASME J. Heat Transfer **129**(3): 298-307.

Kirk (2001). Kirk-Othmer Encylclopedia of Chemical Technology, John Wiley & Sons, Inc. **22:** 69-81.

Korsvik, C., S. Patil, S. Seal and W. T. Self (2007). "Superoxide dismutase mimetic properties exhibited by vacancy engineered ceria nanoparticles." Chem. Commun. (Cambridge, U. K.)(10): 1056-1058.

Kowalczyk, T. A. P. C. J. G. P. A. R. G. (2003). "Developing the solution analogue of the Toth adsorption isotherm equation." Journal of Colloid and Interface Science **266**: 473-476.

Krewski, D., R. A. Yokel, E. Nieboer, D. Borchelt, J. Cohen, J. Harry, S. Kacew, J. Lindsay, A. M. Mahfouz and V. Rondeau (2007). "Human health risk assessment for aluminium, aluminium oxide, and aluminium hydroxide." Journal of Toxicology and Environmental Health, Part B: Critical Reviews **10, Suppl 1**: 1-269.

Kubiak, K. and P. A. Mulheran (2009). "Molecular Dynamics Simulations of Hen Egg White Lysozyme Adsorption at a Charged Solid Surface." J. Phys. Chem. B **113**(36): 12189-12200.

Kumar, D. H. and H. E. Patel (2004). "Model for Heat Conduction in Nanofluids." Physical Review Letters **93**: 144301/144301-144301/144304.

Kumar, K. V., d. C. M. Monteiro, M. Martinez-Escandell, M. Molina-Sabio and F. Rodriguez-Reinoso (2011). "A site energy distribution function from Toth isotherm for adsorption of gases on heterogeneous surfaces." Phys. Chem. Chem. Phys **13**: 5753-5759.

L.A. Rosen, N. A. S., E.D. Glandt (1986). "Random sequential adsorption onto the surface of small spheres." J. Chem. Phys. **85**: 7359-7363.

Land, P. L. (1973). "Defect equilibriums for extended point defects, with application to nonstoichiometric ceria." J. Phys. Chem. Solids **34**(11): 1839-1844.

Lee M. Bishop, J. C. Y., Xin Chen, Jamie N. Wheeler, Marco D. Torelli, Michelle C. Benson, Steven D. Burke, Joel A. Pedersen, and Robert J. Hamers (2011). "A Citric Acid-Derived Ligand for Modular Functionalization of Metal Oxide Surfaces via "Click" Chemistry." Langmuir **28**(2): 1322-1329.

Lee, S., S. U. S. Choi, S. Li and J. A. Eastman (1999). "Measuring thermal conductivity of fluids containing oxide nanoparticles." Journal of Heat Transfer **121**(2): 280-289.

Li, K., Y. Chen, W. Zhang, Z. Pu, L. Jiang and Y. Chen (2012). "Surface Interactions Affect the Toxicity of Engineered Metal Oxide Nanoparticles toward Paramecium." Chem. Res. Toxicol. **25**: 1675-1681.

Li Wang, S. F., Jianghong Zhao, Jianfeng Zheng, Zhijian Wang, Li Li, Zhenping Zhu (2010). "A facile method to modify carbon nanotubes with nitro/amino groups." Journal of applied surface science **256**(20): 6060-6064.

Lindegren M, L. J., Persson P. (2009). "Molecular structures of citrate and tricarballylate adsorbed on alpha-FeOOH particles in aqueous suspensions." Langmuir **25**: 10639-10647.

Liu, J., A. G. Rinzler, H. Dai, J. H. Hafner, R. K. Bradley, P. J. Boul, A. Lu, T. Iverson, K. Shelimov, C. B. Huffman, F. Rodriguez-Macias, Y.-S. Shon, T. R. Lee, D. T. Colbert and R. E. Smalley (1998). "Fullerene pipes." Science (Washington, D. C.) **280**(5367): 1253-1256.

Liu, M.-S., M. C.-C. Lin, I. T. Huang and C.-C. Wang (2005). "Enhancement of thermal conductivity with carbon nanotube for nanofluids." International Communications in Heat and Mass Transfer **32**(9): 1202-1210.

Liu, M.-S., M. C.-C. Lin, I. T. Huang and C.-C. Wang (2006). "Enhancement of thermal conductivity with CuO for nanofluids." Chemical Engineering & Technology **29**(1): 72-77.

Liu, M., M. C. Lin and C. Wang (2011). "Enhancements of thermal conductivities with Cu, CuO, and carbon nanotube nanofluids and application of MWNT/water nanofluid on a water chiller system." Nano Scale Research Letters **6**.

Lu, C.-W., H.-Q. Xie and H.-M. Yu (2003). "Studies on the thermal stability of nano-SiC powder with excessive free carbon by thermal analysis-mass spectrometry coupling technique." Proceedings of the NATAS Annual Conference on Thermal Analysis and Applications **31st**: 162/161-162/164.

Lynch, I. and K. A. Dawson (2008). "Protein-nanoparticle interactions." Nano Today **3**(1-2): 40-47.

Ma, P. C., J.-K. Kim and B. Z. Tang (2006). "Functionalization of carbon nanotubes using a silane coupling agent." Carbon **44**(15): 3232-3238.

Maira, A. J., J. M. Coronado, V. Augugliaro, K. L. Yeung, J. C. Conesa and J. Soria (2001). "Fourier Transform Infrared Study of the Performance of Nanostructured TiO2 Particles for the Photocatalytic Oxidation of Gaseous Toluene." Journal of Catalysis **202**(2): 413-420.

Mandzy, N., E. Grulke and T. Druffel (2005). "Breakage of TiO2 agglomerates in electrostatically stabilized aqueous dispersions." Powder Technology **160**(2): 121-126.

María Jose Pastoriza-Gallego, L. L., José Luis Legido, Manuel M Piñeiro (2011). "heological non-Newtonian behaviour of ethylene glycol-based Fe2O3 nanofluids." Nanoscale Research Letters **6**.

Marie, H. S., K. Ajay, S. Sanjay, S. William, T. Ron, S. Sudipta and R. C. M (2011).

"Bio-distribution and in vivo antioxidant effects of cerium oxide nanoparticles in mice." Environmental toxicology **28**(2): 107-118.

Martinu, L. and D. Poitras (2000). "Plasma deposition of optical films and coatings: A review." Journal of Vacuum Science & Technology A: Vacuum, Surfaces, and Films **18**(6): 2619-2645.

Masui, T. H., H.; Imanaka, N.; Adachi, G.; Sakata, T.; Mori, H. (2002). "Synthesis of cerium oxide nanoparticles by hydrothermal crystallization with citric acid." Journal of Materials Science Letters **21**(6): 489-491.

Mehta, R. L., Ryan A.; Fitch, Hannah M.; Ali, Nawab; Soulsby, Michael; Chowdhury, Parimal (2009). "Studies of Hard and Soft Tissue Elemental Compositions in Mice and Rats Subjected to Simulated Microgravity." AIP Conference Proceedings **1099**: 259-264.

Mosher, B. P., C. Wu, T. Sun and T. Zeng (2006). "Particle-reinforced water based organic-inorganic nanocomposite coatings for tailored applications." Journal of Non-crystalline Solids **352**(30-31): 3295-3301.

Mudunkotuwa IA, G. V. (2010). "Citric acid adsorption on TiO2 nanoparticles in aqueous suspensions at acidic and circumneutral pH: surface coverage, surface speciation, and its impact on nanoparticle-nanoparticle interactions." J. Am. Chem. Soc **132**: 14986-14994.

Murshed, S. M. S., K. C. Leong and C. Yang (2005). "Enhanced thermal conductivity of TiO2-water based nanofluids." International Journal of Thermal Sciences **44**(4): 367-373.

Nan, C.-W., R. Birringer, D. R. Clarke and H. Gleiter (1997). "effective thermal conductivity of particulate composites with interfacial thermal resistance." J. Appl. Phys **81**.

Nikolov, D. T. W. a. A. D. (2003). "Spreading of nanofluids on solids." Nature **423**: 156–159.

Ognibene, T. J. and J. S. Vogel (2004). "Highly sensitive 14C and 3H quantification of biochemical samples using accelerator mass spectrometry." Synth. Appl. Isot. Labelled Compd., Proc. Int. Symp., 8th: 293-295.

Oh, T., K.-M. Lee, K. S. Kim, S. B. Oh, W. H. Kim and C. K. Choi (2005). "HOMO-LUMO interaction between diene and dienophile with an electron-withdrawing group." Key Engineering Materials **277-279**(Pt. 2, On the Convergence of Bio-, Information-, Environmental-, Energy-, Space- and Nano-Technologies): 983-989.

Ould-Moussa, N., M. Safi, M.-A. Guedeau-Boudeville, D. Montero, H. Conjeaud and J.-F. Berret (2013). "In vitro toxicity of nanoceria: effect of coating and stability in biofluids." nanotoxicology.

Pach, J. and P. K. Agarwal (1995). Combinatorial geometry, Wiley-Interscience.

Pailleux, M., D. Boudard, J. Pourchez, V. Forest, P. Grosseau and M. Cottier (2013). "New insight into artifactual phenomena during in vitro toxicity assessment of engineered nanoparticles: Study of TNF-α adsorption on alumina oxide nanoparticle." Toxicol. In Vitro **27**(3): 1049-1056.

Pan, C., D. Zhang and L. Shi (2008). "CTAB assisted hydrothermal synthesis, controlled conversion and CO oxidation properties of CeO2 nanoplates, nanotubes, and nanorods." Journal of Solid State Chemistry **181**(6): 1298-1306.

Pellenbarg, T., N. Dementev, R. Jean-Gilles, C. Bessel, E. Borguet, N. Dollahon and R. Giuliano (2010). "Detecting and quantifying oxygen functional groups on graphite nanofibers by fluorescence labeling of surface species." Carbon **48**(15): 4256-4267.

Perez-Campana, C., V. Gomez-Vallejo, M. Puigivila, A. Martin, T. Calvo-Fernandez, S. E. Moya, R. Ziolo, T. F.Reese and J. Llop (2013). "Biodistribution of Different Sized Nanoparticles Assessed by Positron Emission Tomography: A General Strategy for Direct Activation of Metal Oxide Particles." ACS NANO **7**(4): 3498-3505.

Podkoscielny, P. (2008). "The cooperative effect of the surface heterogeneity and of the lateral interactions between adsorbed molecules on adsorption of simple aromatic compounds from dilute aqueous solutions on activated carbons " Colloids and Surfaces A: Physicochemical and Engineering Aspects **318**(1-3): 227-237.

Poh, C. K., S. H. Lim, H. Pan, J. Lin and J. Y. Lee (2008). "Citric acid functionalized carbon materials for fuel cell applications." Journal of power sources **176**(1): 70-75.

Prasher, R., P. Bhattacharya and P. E. Phelan (2005). "Thermal Conductivity of Nanoscale Colloidal Solutions (Nanofluids) " Physical Review Letters **94**: 025901/025901-025901/025904.

Pugh, R. J., & Fowkes F. M. (1984). "The dispersability and stability of coal particles in hydrocarbon media with a polyisobutene succinamide dispersing agent." Colloids and Surfaces, A Physicochemical and Engineering Aspects **11**: 423-427.

R.K.Ilner (1979). The Chemistry of Silica. New York, Wiley.

Raghuraman, G. K. and R. Dhamodharan (2004). "Polymer grafted titania nanoparticles and magnetite nanoparticles prepared from surface-confined azo initiators and atom transfer radical polymerization (ATRP) initiators." MACRO 2004, International Conference on Polymers for Advanced Technologies, Thiruvananthapuram, India, Dec. 15-17, 2004: PF 3/1-PF 3/7.

Raghuraman, G. K. R., Juergen; Dhamodharan, Raghavachari. (2008). "Grafting of

PMMA brushes on titania nanoparticulate surface via surface-initiated conventional radical and "controlled" radical polymerization (ATRP)." Journal of Nanoparticle Research **13**: 415-427.

Rajendran, S. G. a. V. (2013). "Influence of Various Surfactants on Size, Morphology, and Optical Properties of CeO2 Nanostructures via Facile Hydrothermal Route." Journal of Nanoparticles: 1-6.

Ravichandran, S., J. D. Madura and J. Talbot (2001). "A Brownian Dynamics Study of the Initial Stages of Hen Egg-White Lysozyme Adsorption at a Solid Interface." J. Phys. Chem. B **105**(Copyright (C) 2011 American Chemical Society (ACS). All Rights Reserved.): 3610-3613.

Rezwan, K., A. R. Studart, J. Voeroes and L. J. Gauckler (2005). "Change of z Potential of Biocompatible Colloidal Oxide Particles upon Adsorption of Bovine Serum Albumin and Lysozyme." J. Phys. Chem. B **109**(30): 14469-14474.

Robeson, J. L. and R. D. Tilton (1996). "Spontaneous Reconfiguration of Adsorbed Lysozyme Layers Observed by Total Internal Reflection Fluorescence with a pH-Sensitive Fluorophore." Langmuir **12**(Copyright (C) 2011 American Chemical Society (ACS). All Rights Reserved.): 6104-6113.

Rojas, S., J. D. Gispert, S. Abad, M. Buaki-Sogo, V. M. Victor, H. Garcia and J. R. Herance (2012). "In Vivo Biodistribution of Amino-Functionalized Ceria Nanoparticles in Rats Using Positron Emission Tomography." Mol. Pharmaceutics, **9**(12): 3543-3550.

Rzigalinski, B. A. (2005). "Nanoparticles and cell longevity." Technol. Cancer Res. Treat. **4**(6): 651-659.

S.-C. Tzeng, C.-W. L., and K. D. Huang (2005). "Heat transfer enhancement of nanofluids in rotary blade coupling of four-wheel-drive vehicles." Acta Mechanica **179**: 11-23.

Sabol, J. and P.-s. Weng (1995). Introduction to Radiation Protection Dosimetry, World Scientific.

Sahoo, B., M. Goswami, S. Nag and S. Maiti (2007). "Spontaneous formation of a protein corona prevents the loss of quantum dot fluorescence in physiological buffers." Chem. Phys. Lett. **445**(4-6): 217-220.

Sandhu, K. K., C. M. McIntosh, J. M. Simard, S. W. Smith and V. M. Rotello (2002). Bioconjugate Chemistry **13**.

Sasha Stankovich, R. D. P., Xinqi Chen, Nianqiang Wu, SonBinh T. Nguyen and Rodney S. Ruoff, (2006). "Stable aqueous dispersions of graphitic nanoplatelets via the reduction of exfoliated graphite oxide in the presence of poly(sodium 4-styrenesulfonate)." J. Mater. Chem **16**(2): 155-158.

Schaefer, J., C. Schulze, E. E. J. Marxer, U. F. Schaefer, U. B. Wendel Wohlleben and C.-M. Lehr (2012). "Atomic Force Microscopy and Analytical Ultracentrifugation for Probing Nanomaterial Protein Interactions." ACS Nano **6**(6): 4603-4614.

Schoell, S. J., M. Hoeb, I. D. Sharp, W. Steins, M. Eickhoff, M. Stutzmann and M. S. Brandt (2008). "Functionalization of 6H-SiC surfaces with organosilanes." Applied Physics Letters **92**(15): 153301/153301-153301/153303.

Seidel, A. and P. S. Carl (1989). "The concentration dependence of surface diffusion for adsorption on energetically heterogeneous adsorbents." Chem. Eng. Sci. **44**(Copyright (C) 2011 American Chemical Society (ACS). All Rights Reserved.): 189-194.

Seok, S. H., W.-S. Cho, J. S. Park, Y. Na, A. Jang, H. Kim, Y. Cho, T. Kim, J.-R. You, S. Ko, B.-C. Kang, J. K. Lee, J. Jeong and J.-H. Che (2013). " Rat pancreatitis produced by 13-week administration of zinc oxide nanoparticles: biopersistence of nanoparticles and possible solutions." Journal of applied nanotoxicity **33**(10): 1089-1096.

Shaffer, M. S. P., X. Fan and A. H. Windle (1998). "Dispersion and packing of carbon nanotubes." Carbon **36**(11): 1603-1612.

Shen, Z. G. and J. F. Chen (2004). "Dispersion of nanosized aqueous suspensions of barium titanate with ammonium polyacrylate." Journal of Colloid and interface Science **275**: 158-164.

Shenogin, S. and L. Xue (2004). "Role of thermal boundary resistance on the heat flow in carbon-nanotube composites." Journal of applied physics **95**: 8136-8144.

Shenoy, A. V. (1998). Filled Polymer Systems: Rheological Principles, Chapman & Hall.

Shi, Y. C. and Y. S. Wu (2003). "Surface and Rheology Characaterization of NH4PAA-Stabilized Nanosized TiO2 suspensions." Journal of Dispersion Science and Technology **24**: 739-743.

Shimada, T., K. Aoki, Y. Shinoda, T. Nakamura, N. Tokunaga, S. Inagaki and T. Hayashi (2003). "Functionalization on Silica Gel with Allylsilanes. A New Method of Covalent Attachment of Organic Functional Groups on Silica Gel." Journal of the American Chemical Society **125**(16): 4688-4689.

Shvedova, A. A. K., V. E. (2010). "The role of nanotoxicology in realizing the 'helping without harm' paradigm of nanomedicine: lessons from studies of pulmonary effects of single-walled carbon nanotubes." Journal of Internal Medicine **267**(1): 106-118.

Smith, A. M., H. W. Duan, A. M. Mohs and S. M. Nie (2008). "Bioconjugated quantum dots for in vivo molecular and cellular imaging." Adv. Drug Delivery Rev **60**: 1226-1240.

Smits, K., J. Liepins, M. Gavare, A. Patmalnieks, A. Gruduls and D. Jankovica (2012). "Zirconia nanocrystals as submicron level biological label." IOP Conf. Ser. Mater. Sci. Eng. **38**: 012050/012051-012050/012054.

Sneh, O. and S. M. George (1995). "Thermal Stability of Hydroxyl Groups on a Well-Defined Silica Surface." Journal of Physical Chemistry **99**(13): 4639-4647.

Sund, u., H. Alenius, M. Vippola, K. Savolainen and A. Puustinen (2011). "Proteomic Characterization of Engineered Nanomaterial: ProteinInteractions in Relation to Surface Reactivity." ACS Nano **5**(6): 4300-4309.

Suslick, K. S. and G. J. Price (1999). "Applications of ultrasound to materials chemistry." Annual Review of Materials Science **29**: 295-326.

Suzuki, T., I. Kosacki, H. U. Anderson and P. Colomban (2001). "Electrical conductivity and lattice defects in nanocrystalline cerium oxide thin films." J. Am. Ceram. Soc. **84**(9): 2007-2014.

T.J. Ognibene, G. B., J.S. Vogel, G.F. Peaslee, S. Murov (2003). "A High-Throughput Method for the Conversion of CO2 Obtained from Biochemical Samples to Graphite in Septa-Sealed Vials for Quantification of 14C via Accelerator Mass Spectrometry." Anal. Chem. **75**: 2192-2196.

Tamura, H. (2002). Ion complexation at oxide-solution interfaces. Encyclopedia of Surface and Colloid Science. A. T. Hubbard. **3:** 2860.

Taratula, O. G. E. W., D.; Chu, D.; Zhang, Z.; Chen, H.; Saraf, G. and Lu, Y. (2006). "Binding Studies of Molecular Linkers to ZnO Nanotips." J. Phys. Chem. B **110**: 6506-6515.

Tarnuzzer, R. W., J. Colon, S. Patil and S. Seal (2005). "Vacancy Engineered Ceria Nanostructures for Protection from Radiation-Induced Cellular Damage." Nano Lett. **5**(12): 2573-2577.

Tiemeyer, S., M. Paulus and M. Tolan (2010). "Effect of Surface Charge Distribution on the Adsorption Orientation of Proteins to Lipid Monolayers." Langmuir **26**(Copyright (C) 2011 American Chemical Society (ACS). All Rights Reserved.): 14064-14067.

Tok, A. I. Y., F. Y. C. Boey, Z. Dong and X. L. Sun (2007). "Hydrothermal synthesis of CeO2 nano-particles." J. Mater. Process. Technol **190**(Copyright (C) 2011 American Chemical Society (ACS). All Rights Reserved.): 217-222.

Toth, J. (2002). Adsorption: Theory, Modeling, and Analysis. [In: Surfactant Sci. Ser., 2002; 107], Marcel Dekker, Inc.

Tseng, W. and K. C. Lin (2003). "Rheology and colloidal structure of aqueous TiO2 nanoparticle suspensions." Material Science & Engineering, A: Structural Materials: Properties, Microstructure and Processing **A355**: 186-192.

Tsutsumi, Y. Y., Yasuo (2011). "Quantifying the biodistribution of nanoparticles." Nature Nanotechnology **6**(12).

V. Kanniah, B. W., Y. Yang, E. A. Grulke (2012). "Graphite functionalization for dispersion in a two-phase lubricant oligomer mixture." Journal of Applied Polymer Science **125**(1): 165-174.

van Drunen, M. A., R. Finsy, H. G. Merkus, B. Scarlett and G. M. van Rosmalen (1993). "Measurement of cluster formation in aqueous citric acid solutions by photon correlation spectroscopy." Journal of Crystal Growth **134**(3-4): 196-202.

Verma, A. and V. M. Rotello (2005). "Surface recognition of biomacromolecules using nanoparticle receptors." Chem. Commun.: 303-312.

Vigil, R. D. and R. M. Ziff (1990). "Kinetics of random sequential adsorption of rectangles and line segments." J. Chem. Phys. **93**(Copyright (C) 2011 American Chemical Society (ACS). All Rights Reserved.): 8270-8272.

Viot, P., G. Tarjus, S. M. Ricci and J. Talbot (1992). "Random sequential adsorption of anisotropic particles. I. Jamming limit and asymptotic behavior." J. Chem. Phys. **97**(Copyright (C) 2011 American Chemical Society (ACS). All Rights Reserved.): 5212-5218.

Wang, B., Jackson, G., Yokel, R. A., Grulke, E.A. (2013). "Applying accelerator mass spectrometry for low-level detection of complex engineered nanoparticles in biological media." Journal of Pharmaceutical and Biomedical Analysis. Submitted

Wang, B., Wu, P., Yokel, R.A., Grulke, E.A. (2012). "Influence of surface charge on lysozyme adsorption to ceria nanoparticles." Applied Surface Science **258**(14): 5232-5241.

Wang, Q., J. M. Perez and T. J. Webster (2013). "Inhibited growth of Pseudomonas aeruginosa by dextran- and polyacrylic acid-coated ceria nanoparticles." International Journal of Nanomedicine **8**: 3395-3399.

Wang, T. H. H., Hui An; Hsieh, Yi Kong; Chiang, Chi Shiun; Sun, Yuh Chang; Wang, Chu Fang (2012). "The in vivo biodistribution and fate of CdSe quantum dots in the murine model: a laser ablation inductively coupled plasma mass spectrometry study."

Analytical and Bioanalytical Chemistry **404**(10): 3025-3036.

Wanga, B., X. Wanga, W. Loua and J. Hao (2012). "Thermal conductivity and rheological properties of graphite/oil nanofluids." Colloids and Surfaces A: Physicochemical and Engineering Aspects **414**: 125-131.

Wei, A. P., J. N. Herron and J. D. Andrade (1990). From Clone to Clinic, Kluwer Academic.

Wen, D. and Y. Ding (2004). "Effective thermal conductivity of aqueous suspensions of carbon nanotubes (carbon nanotube nanofluids)." Journal of Thermophysics and Heat Transfer **18**(4): 481-485.

Wensel, J., B. Wright, D. Thomas, W. Douglas, B. Mannhalter, W. Cross, H. Hong, J. Kellar, P. Smith and W. Roy (2008). "Enhanced thermal conductivity by aggregation in heat transfer nanofluids containing metal oxide nanoparticles and carbon nanotubes." Applied Physics Letters **92**(2): 023110/023111-023110/023113.

Wierenga, A. M. and A. P. Philipse (1998). "Low-shear viscosity of isotropic dispersions of (Brownian) rods and fibers; a review of theory and experiments." Colloids and Surfaces, A Physicochemical and Engineering Aspects **137**(1-3): 355-372.

Won, Y. Y., S. P. Meeker, V.Trappe, D.A.Weitz, N.Z.Diggs and J.I.Emert (2005). "Effect of temperature on carbon-black agglomeration in hydrocarbon liquid with adsorbed dispersant." langmuir **21**(3): 924-932.

Wu, L., H. J. Wiesmann, A. R. Moodenbaugh, R. F. Klie, Y. Zhu, D. O. Welch and M. Suenaga (2004). "Oxidation state and lattice expansion of CeO2-x nanoparticles as a function of particle size." Phys. Rev. B: Condens. Matter Mater. Phys. **69**(12): 125415/125411-125415/125419.

Xie, H., H. Lee, W. Youn and M. Choi (2003). "Nanofluids containing multiwalled carbon nanotubes and their enhanced thermal conductivities." Journal of Applied Physics **94**(8): 4967-4971.

Xie, H., J. Wang, T. Xi and Y. Liu (2001). "Study on the thermal conductivity of SiC nanofluids." Journal of the Chinese Ceramic Society **29**(4): 361-364.

Xie, H., J. Wang, T. Xi, Y. Liu, F. Ai and Q. Wu (2002). "Thermal conductivity enhancement of suspensions containing nanosized alumina particles." Journal of applied physics **91**: 4568-4572.

Xie, Y., J. Zhou and S. Jiang (2010). "Parallel tempering Monte Carlo simulations of lysozyme orientation on charged surfaces." J. Chem. Phys. **132**(Copyright (C) 2011 American Chemical Society (ACS). All Rights Reserved.):

065101/065101-065101/065108.

Xu, X. and A. M. Lenhoff (2008). "A Predictive Approach to Correlating Protein Adsorption Isotherms on Ion-Exchange Media." J. Phys. Chem. B **112**(3): 1028-1040.

Xue, L. and P. Keblinski (2003). "Two regimes of thermal resistance at a liquid-solid interface." Journal of Chemical Physics **118**: 337-339.

Yamamoto, S. and T. Matsuoka (1999). "Dynamic simulation of rod-like and plate-like particle dispersed systems." Computational Materials Science **14**(1-4): 169-176.

Yang, Y., E. A. Grulke, Z. G. Zhang and G. Wu (2005). "Rheological behavior of carbon nanotube and graphite nanoparticle dispersions." Journal of Nanoscience and Nanotechnology **5**(4): 571-579.

Yang, Y., E. A. Grulke, Z. G. Zhang and G. Wu (2006). "Thermal and rheological properties of carbon nanotube-in-oil dispersions." Journal of Applied Physics **99**(11): 114307/114301-114307/114308.

Yao, Y. and A. M. Lenhoff (2005). "Electrostatic Contributions to Protein Retention in Ion-Exchange Chromatography. 2. Proteins with Various Degrees of Structural Differences." Anal. Chem. **77**(7): 2157-2165.

Ying Yang, Z. G. Z., Eric A. Grulke, William B. Anderson, Gefei Wu (2005). "Heat transfer properties of nanoparticle-in-fluid dispersions (nanofluids) in laminar flow " International Journal of Heat and Mass Transfer **48**(6): 1107-1116.

Yokel, R., Grulke, E., MacPhail, R. Metal-based nanoparticle interactions with the nervous system: the challenge of brain entry and the risk of retention in the organism (2013). "Metal-based nanoparticle interactions with the nervous system: the challenge of brain entry and the risk of retention in the organism." WIREs Nanomed Nanobiotechnol **5**: 346-373.

Yokel, R. A., T. C. Au, R. MacPhail, S. S. Hardas, D. A. Butterfield, R. Sultana, M. T. Tseng, M. Dan, R. L. Florence, J. M. Unrine, U. M. Graham, P. Wu and E. A. Grulke (2012). "Distribution, elimination and biopersistence to 90 days of a systemically-introduced 30 nm ceria engineered nanomaterial in rats." Toxicological Sciences **127**(1): 256-268.

Yokel, R. A. and J. M. Melograna (1983). "A safe method to acid digest small samples of biological tissues for graphite furnace atomic absorption analysis of aluminum." Biol. Trace Elem. Res. **5**(3): 225-237.

Yokel, R. A., M. T. Tseng, M. Dan, J. M. Unrine, U. M. Graham, P. Wu and E. A. Grulke (2013). "Biodistribution and biopersistence of ceria engineered nanomaterials: size dependence." Nanomedicine (N. Y., NY, U. S.) **9**(3): 398-407.

Yoo, D.-H., K. S. Hong and H.-S. Yang (2007). "Study of thermal conductivity of nanofluids for the application of heat transfer fluids." Thermochimica Acta **455**: 66-69.

Yu, C.-J., A. G. Richter, A. Datta, M. K. Durbin and P. Dutta (1999). "Observation of Molecular Layering in Thin Liquid Films Using X-Ray Reflectivity." Physical Review Letters **82**: 2326-2329.

Z. R. Tian, J. A. V., J. Liu, B. Mckenzie, M. J. Mcdermott, M. A. Rodriguez,H. Konishi, H. Xu (2003). "Complex and oriented ZnO nanostructures." Nature Materials **2**: 821-826.

Zaman, A. A. and P. Singh (2002). "Impact of Self-assembled Surfactant structures on Rheology of Concentrated Nanoparticle Dispersions." Journal of Colloid and interface Science **251**: 381-387.

Zhan, L., G. Yanxia, Z. Xiaoyong, Q. Wei, F. Qiaohui, L. Yan, J. Zongxian, W. Jianjun, T. Yuqin, D. Xiaojiang and W. Wu (2011). "Biodistribution of co-exposure to multi-walled carbon nanotubes and graphene oxide nanoplatelets radiotracers." Journal of Nanoparticle Research **13**(7): 2939-2947.

Zhang, N., J. Xie and V. K. Varadan (2002). "Functionalization of carbon nanotubes by potassium permanganate assisted with phase transfer catalyst." Smart Materials and Structures **11**(6): 962-965.

Zhang, W., D. Li and J. Wang (2009). "Cu-induced poly-Si/SiO2/伪-Si multilayer film with high reflectivity across the whole visible band." Phys. Status Solidi RRL **3**(2-3): 82-84.

Zhang, X., H. Gu and M. Fujii (2007). "Effective thermal conductivity and thermal diffusivity of nanofluids containing spherical and cylindrical nanoparticles." Exp.Therm. Fluid. Sci **31**(6): 593-599.

Zhao, F., Y.-K. Du, J.-K. Xu and S.-F. Liu (2006). "Determination of surfactant molecular volume by atomic force microscopy." Colloid J. **68**(Copyright (C) 2011 American Chemical Society (ACS). All Rights Reserved.): 784-787.

Zhou, J., S. Chen and S. Jiang (2003). "Orientation of Adsorbed Antibodies on Charged Surfaces by Computer Simulation Based on a United-Residue Model." Langmuir **19**(8): 3472-3478.

Zhou, J., H.-K. Tsao, Y.-J. Sheng and S. Jiang (2004). "Monte Carlo simulations of antibody adsorption and orientation on charged surfaces." J. Chem. Phys. **121**(2): 1050-1057.

Zhou, J., J. Zheng and S. Jiang (2004). "Molecular Simulation Studies of the Orientation and Conformation of Cytochrome c Adsorbed on Self-Assembled Monolayers." J. Phys. Chem. B **108**(45): 17418-17424.

Zhu, H., C. Zhang, S. Liu, Y. Tang and Y. Yin (2006). "Effects of nanoparticle clustering and alignment on thermal conductivities of Fe3O4 aqueous nanofluids." Appl. Phys. Lett. **89**: 023123.

Vita

Binghui Wang was born in Beijing, P.R.C. He attended Beijing University of Chemical Technology, where he received his Bachelor of Engineering in Polymer Science and Engineering in July 2003. He attended Katholieke Universiteit Leuven in Belgium, where he received Master of Engineering in Materials Engineering. He began his Ph.D. study at University of Kentucky in August 2005.

Publications:

V. Kanniah, B. Wang, Y. Yang, Eric A.Grulke. "Graphite functionalization for dispersion in a two-phase lubricant oligomer mixture." Journal of Applied Polymer Science 125(1): 165-174.(2012)

Wang, B., Wu, P., Yokel, R.A., Grulke, E.A. (2012). "Influence of surface charge on lysozyme adsorption to ceria nanoparticles." Applied Surface Science **258**(14): 5232-5241.

Wang, B., Jackson, G., Yokel, R. A., Grulke, E.A. (2013). "Applying accelerator mass spectrometry for low-level detection of complex engineered nanoparticles in biological media." Journal of Pharmaceutical and Biomedical Analysis. Submitted

Binghui Wang
Student Signature

12/19/13
Date